Perhaps the most valuable result of all education is the ability to make yourself do the thing you have to do, when it ought to be done whether you like it or not, it is the first lesson that ought to be learned; and however early a man's training begins, it is probably the last lesson that he learns thoroughly – Thomas H. Huxley

University of Alberta

Specific Phage Based Bacteria Detection Using Microcantilever Sensors

by

Nicholas Ryan Glass

A thesis submitted to the Faculty of Graduate Studies and Research
in partial fulfillment of the requirements for the degree of

Master of Science

in

Micro-Electro-Mechanical Systems and Nanosystems

Electrical and Computer Engineering

Fall 2009

Edmonton, Alberta

Examining Committee

Dr. Stephane Evoy, Electrical and Computer Engineering, University of Alberta

Dr. Michael Brett, Electrical and Computer Engineering, University of Alberta

Dr. Christine Szymanski, Biological Sciences, University of Alberta

I dedicate this thesis to my parents, Al and Sherry, for their unconditional support and encouragement throughout my education.

Abstract

Resonant microcantilevers are promising transducers for bacteria detection because of their high sensitivities. Surface stress and mass from adsorbates affect the resonant frequency. We developed a novel method for decoupling the frequency contributions of a change in mass and surface stress on a cantilever sensor validated in theoretical, finite element and experimental framework.

Bacteria capture was achieved by several different chemical immobilization of T4 phages. The most successful bacteria capturing surface produced bacterial densities of about 11 bacteria/100μm^2. The developed theory is then applied to determine captured bacterial mass on the cantilevers. This provides an estimate of the bacteria mass on the cantilever. Two different functionalizations resulted in predicted bacterial densities of 5 bacteria/100μm^2 and 3 bacteria/100μm^2. Poor densities relative to surface capture experiments is caused by the boundary effects of the cantilever in solution.

Acknowledgements

First and foremost, I would like to thank Dr. Stéphane Evoy, my supervisor. His guidance and insight has truly been instrumental in my development as a researcher. His patience, support and troubleshooting skills have been vital in keeping me on track throughout my degree. Furthermore, it was Stéphane who introduced me to the field of MEMS and nanotechnology, which has become a great interest of mine over the past few years. He has also given invaluable advice on academia and life as a researcher that have helped me greatly through the last few years.

Dr. Amit Singh has had a profound influence on my degree. He has truly been a great source of knowledge, ideas and was also willing to discuss new thoughts. He also has assisted with countless experiments, always in good spirits. Working with him as been a pleasure. Luc Gervais, also deserves a huge thanks. He took the time to train me in all the skills I needed to hit the ground running on my research project. Furthermore, Luc was always willing to take the time to help even now. A huge thanks also go out to Dr. Christine Szymanski for many fruitful phage discussions as well as many useful suggestions. Thanks are also due to Jamshid Tanha for phage discussions.

Many thanks also go out to Lee Fischer, Andrew Murray and Nathan Nelson-Fitzpatrick. Lee was always excited to talk about mechanics and providing fresh prospectives on new thoughts. Andrew was more than willing to lend an ear troubleshoot problems and microfabrication ideas. Andrew was also always in good spirits during many late night thesis workings. A special thanks goes to Nathan, who was always up for discussing different aspects of cantilever and surface science. Furthermore, Nathan has been there countless times for experimental help, weekend work and last minute favors. I truly would not have finished if it wasn't for him. In addition, Lee, Andrew and Nathan all made my

transition into graduate school and a new department one of the best experiences of my life.

Also, thanks to Sarang Dutt, for assistance with surface characterization and help with experiments in the final months of my research. In addition, thanks to Ravendra Naidoo for all sorts of interesting phage immobilization conversations. Thanks to Daniel Salomon, for amazing SEM support and Les Schowalter for top-notch sputtering support. Thanks to Mansel Griffiths for supplying T4 bacteriophages. Thanks to Shannon Lubitz and Megan Brebber for essential biological lab support and helping me with some unconventional biological lab problems. Also, a special thanks goes to Eric Finley for all sorts of various experimental support, often with very little notice. Dr. Wayne Materi has also been a big source of guidance in many biological aspects of my research.

Finally, to family and friends who have supported through both good times and tough times. I truly could not have done any of this without your support.

Table of Contents

List of Tables

List of Figures

List of Abbreviations

AFM	Atomic force microscope
BSA	Bovine serum album
cfu	Colony forming units
DNA	Deoxyribonucleic acid
EDC	1-Ethyl-3-[3-dimethylaminopropyl]carbodiimide hydrochloride
ELISA	Enzyme linked immunosorbant assay
Fab	Antigen binding fragment
Fc	Crystallizable fragment
FEA	Finite element analysis
LB	Luria Bertani
MEMS	Microelectromechanical systems
PBS	Phosphate buffered saline
PCR	Polymerase chain reaction
QCM	Quartz crystal microbalance
RNA	Ribonucleic acid
SAM	Self assembled monolayer
SAW	Surface acoustic wave

SEM	Scanning electron microscope
SPR	Surface plasmon resonance
ssDNA	Single stranded DNA
Sulfo-NHS	N-hydroxysulfosuccinimide
TSB	Tryptic soy broth
TSBT	Tryptic soy broth with 0.05% Tween20

1 Bacteria Detection

1.1 Introduction

The discovery of germs was one of the greatest advances in medicine. The concept that many diseases and illnesses were caused by microorganisms changed society forever. Knowledge of microbiology has increased dramatically since then. It is now common knowledge that bacteria can be found almost everywhere.

There are many different types of bacteria with huge variations in their properties. The level of pathogenesis is typically determined by species or strain of a bacteria. A bacterial strain is a subset of a bacterial species, which often only differs by a few genes. Most bacteria strains are not harmful to the public health. Some of these bacteria are even symbiotic with larger animals. For example several different types of *Escherichia coli* assist in the human digestive process by breaking down food and producing the vitamin K_2. However, species like *E. coli* O157:H7 can cause food poisoning. While most people with healthy immune systems can fight off the bacteria, outbreaks can be fatal in children, the elderly, and other groups with compromised immunity [1].

Pathogenic bacteria can cause a variety of diseases and can be exposed to people through various sources. *Salmonella*, for example, has many different subsets that are pathogenic. *Salmonella* Typhimurium is a common species often found in poultry, which causes many food poisoning incidents in North America. *Salmonella* Typhi causes typhoid fever and spreads by contaminated fecal matter in water systems. Contraction of typhoid fever is

known to cause death in 10-30 percent of untreated cases [1]. *Campylobacter jejuni* is responsible for most foodborne illnesses in the world. It can be found in undercooked pork and poultry, untreated water, and unpasteurized milk. *E. coli* O157:H7 is found in the intestine of cattle and can contaminate meat in the slaughtering process or feces can contaminate local water supplies [2]. Since the bacteria remains on the surface of the meat, they are easily killed by cooking the food. However, ground beef that is not fully cooked can still have some bacteria present [1].

Most deaths caused by bacterial infections occur in people with weakened immune systems. As such, hospitals require microbe free environments to prevent infections in recovering patients. The contagious nature of bacteria also brings sanitation to a very high priority. Furthermore, antibiotic-resistant strains of bacteria are becoming more common, making treatment significantly more difficult [1]. These issues highlight the importance of early prevention and detection [3].

As a result, realtime, point of care detection of pathogens is of great interest to public health, agricultural and water treatment industries alike. Such detection methods would not only represent significant laboratory cost saving, but also help ensure the public health.

1.2 Conventional Bacteria Detection

1.2.1 Culture and Plating Methods

One of the oldest form of bacteria detection is the culturing and plating method. Because of its reliability and ease of use, it is also the standard method of bacteria detection. The bacteria is first grown to a detectable concentration by enrichment [1, 3, 4]. The concentration of the enriched bacteria can then be determined by seeding drops of various dilutions of bacteria. The plate can then be incubated so that the bacteria reproduce until single colonies are visible [3]. Since one colony represents one single viable bacteria at the time of the drop seeding, the original concentration can be precisely determined. This method is very sensitive and is considered the gold standard for quantifying bacteria. The units of bacterial concentration are colony forming units (cfu) per unit volume. Due to the many growing steps involved in this technique, detection can take weeks for reliable results [5]. If the presence of bacteria is only important and not the quantity, inspection of the growth media can be used instead. Media that appears cloudy or opaque after enrichment contains bacteria.

The species and strain of bacteria is also important to determine the associated hazards and concerns. Selective medias and inhibitors have been developed to support the growth

of specific bacteria. Strain identification can take on the order of days or weeks because of the slow growth rate of some bacteria. By using several selective medias in parallel the type of bacteria can be identified [6]. For example, identification of *Salmonella*, a common food borne pathogen, takes more than a week using conventional methods [3].

In order for other bacteria detection methods to become mainstream, they must offer comparable sensitivities to that of the colony counting method. This means bacteria concentrations as low as 10 to 100 cfu/mL should within the detectable limits.

1.2.2 Immunological Methods

Immunological bacteria detection methods rely on exploiting the antibody-antigen affinity. The concept is based on the fact that bacteria will have many different antigens on their cell wall [7]. Some antigens are specific to only certain species or strains of bacteria. The antibody to that antigen can then be used to target or capture that specific type of bacteria.

One common immunological technique involves the functionalization of beads or particles with antibodies specific to a bacteria strain [5, 8, 9]. These particles are then mixed with the sample to be analyzed. If the bacteria of interest is present, the particles will attach to them. Both separation and/or detection can be carried out though design of the particle's properties. For example, magnetic particles maybe used to separate the bacteria from the rest of the sample [9]. Bacteria separated out can then be enumerated using another method [5]. Alternatively, particles that are fluorescent could be used with flow cytometry for enumeration [10].

Another immunological technique used for the detection of bacteria is Enzyme Linked Immunosorbant Assays (ELISA). ELISA is a biochemical assay used to determine the concentration of a biological analyte. The technique can be summarized as follows [5]:

1. Antibodies are immobilized on a multi-well plate followed by rinsing. This antibody is called the recognition antibody.

2. The sample is introduced to a well. If the antigen specific to the recognition antibody is present (on the cell wall of a bacteria) they will bind. This well is then rinsed again with a mild surfactant to prevent unspecific binding.

3. Another antibody, also specific to the target, is then added to the well. This antibody is called the detection antibody. The detection antibody is modified so that there is an enzyme attached at the conservative end. Once added, the detection antibody will tag the antigen. The well is once again rinsed with a mild surfactant.

4. The enzyme's substrate is then added to the well. The enzyme is chosen so that the break down of its substrate will cause a measurable color change.

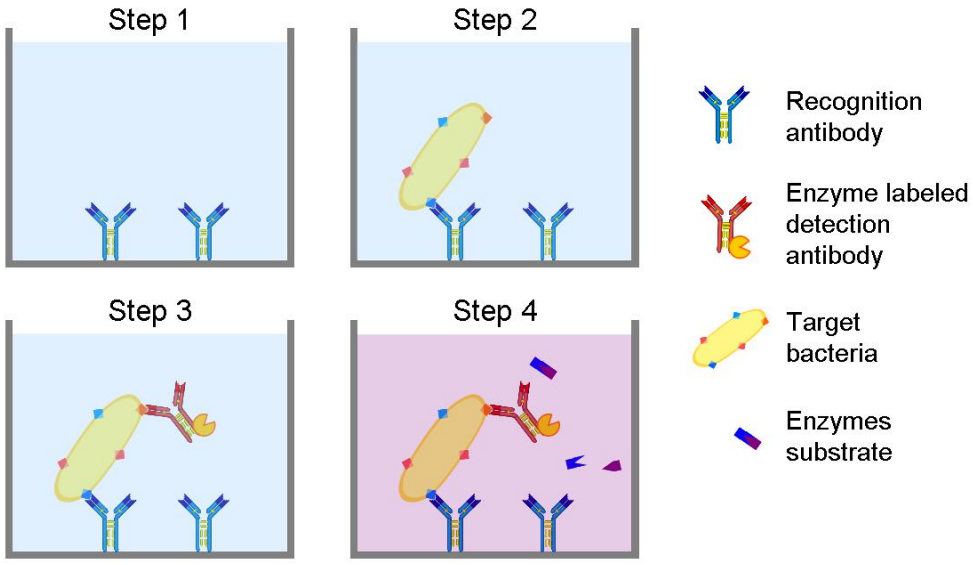

Figure 1.1: The process of ELISA. Step 1: Recognition antibody immobilization. Step 2: The target is captured. Step 3: The target is labeled with an enzyme linked detection antibody. Step 4: The enzyme's substrate is added to the well and a color change results. Rinsing is required after each step, often with a mild surfactant.

Naturally, only if the target is present will a color change occur. The concentration of the target can also be determined if the enzymes reaction rate is known. ELISA is a fairly standard method involved in the detection of bacteria [3, 7]. For example, Ferguson et al. used an ELISA to detect *Bacillus subtilis* in strawberry plants [11].

The technique requires that the use of two different antibodies specific to the target bacteria and extensive purification of the sample [5]. Another major drawback of such a method is that it requires labeling the bacteria. This means that in order to detect a bacteria, it has to be tagged to produce a detectable signal.

1.2.3 Genetic Methods

Because the genome of a given bacteria species or strain is very specific, genetic diagnostics have been of interest for bacteria detection [5]. These methods require that the bacteria be enriched and lysed so their deoxyribonucleic acid (DNA) can be isolated. The DNA is then often amplified using Polymerase Chain Reaction (PCR). Briefly, PCR uses thermal cycling

with heat resistant DNA polymerase, free nucleotides and small strands of DNA called primers to amplify DNA. DNA is heated up so that it is broken into two complementary strands. The primers are designed to bind to one end of the DNA strands. DNA polymerase then uses the primer as a start site so that a complementary strand can be produced using the free nucleotides. This is one PCR cycle and can be repeated many times. Once the DNA is increased to detectable levels, several different methods can be used to be determine the strain [3].

The simplest assay involves the cutting of the genetic material with several restriction enzymes. The DNA can then be separated by length by agarose gel electrophoresis. Accordingly, the segment length can be compared to known species or strain of bacteria exposed to the same restriction enzymes [12]. Some commercial PCR detection systems can determine the genetic sequence, by attaching fluorescent molecules to the DNA during amplification [6, 13].

There has been significant commercialization in microarrays for genetic testing [14, 15]. Microarrays are planar arrays that are functionalized with a certain type with single strand DNA (ssDNA) in each region. These devices are able to read out successful hybridization of complementary ssDNA on each region of the array either through optical or electrical means. Massively parallel genetic testing is possible because each region is sized on the order of microns. Microarrays can be used for pathogen identification by searching for sequences specific to that strain of bacteria. However, amplification by PCR is often necessary because relatively large amounts of genetic material are required [14].

1.3 Biosensors Defined

The Biosensors and Bioelectronics journal defines a biosensor as:

"Biosensors are defined as analytical devices incorporating a biological material (eg. tissue, microorganisms, organelles, cell receptors, enzymes, antibodies, nucleic acids etc), a biologically derived material or biomimic intimately associated with or integrated within a physiochemical transducer or transducing microsystem, which may be optical, electrochemical, thermometric, piezoelectric, magnetic or micromechanical." [16]

To that end, bacterial biosensors combine a transducer (mechanical, electrical, chemical, or optical) with a specific bacterial recognition probe (antibodies or ligands). By doing so, a biosensor can specifically detect bacteria often at the strain level. Furthermore, because the transduction method is a physical response to the presence of the of the bacteria, they are often label free. That is, the device can detect the bacteria without tagging it.

1.4 Surface Modification for Specific Bacteria Detection

1.4.1 Antibodies

Antibodies are the most common form of biosensor functionalization. As outlined in Section 1.2.2, antibodies can be used to capture specific antigens. Antibodies can be used to detect individual proteins, viruses and bacteria that have their binding site present. Typically, biosensor transducers rely on capturing the target on a surface [7].

There are several different types of antibodies. They exist in monomer, dimer and pentamer forms [9]. In biosensing, monomer antibodies are often used. The basic structure of a monomer antibody is shown in Figure 1.2. Antibodies can be broken down into two different domains: the crystallisable fragment (Fc) and the antigen binding fragment (Fab). The Fc domain is conservative between antibodies. It is desired to immobilize an antibody by anchoring the Fc domain so that the active end is sterically accessible. The carboxyl end groups of the Fc domain are often used to achieve directional immobilization. The antigen binding site is located at the end of the Fab domain [17]. This site is responsible for the specific binding of the antigen and varies between antibodies.

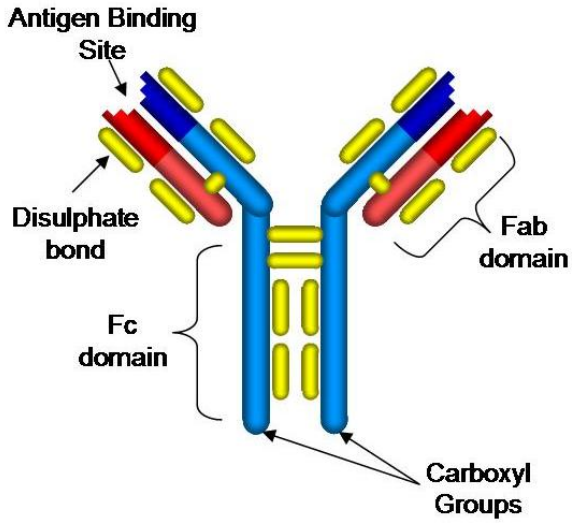

Figure 1.2: The structure of a typical monomer antibody.

Several methods have been developed to enhance antibody immobilization. Both improvements in attachment density and orientation will appreciably increase the antigen capturing. The physical adsorption of antibodies onto sensor surfaces is also commonly employed [7]. Sensors that rely on adsorption typically have surfaces that support strong physical adsorption or chemisorption. Furthermore, adsorption can be enhanced by the use

of an adsorbed capture molecule, such as Protein A [17]. Protein A is known to capture the conservative end of an antibody.

Several other methods have been developed in order to chemically anchor antibodies onto surfaces. A chemical group can be introduced to a surface through use of a plasma [18] or a Self Assembled Monolayer (SAM) [5, 17, 19–21]. SAMs are molecules that will form a single ordered layer of molecules on a surface. Subsequently, various crosslinkers, such as 1-Ethyl-3-[3-dimethylaminopropyl]carbodiimide hydrochloride (EDC) and N-hydroxysulfosuccinimide (Sulfo-NHS), can be used [5]. EDC and Sulfo-NHS are used to couple a carboxyl group to an amine group by forming an amide bond [22]. Since carboxyl and amine groups are common in proteins, these chemistries can be very useful in immobilizing antibodies or other proteins [17]. While these methods are limited in terms of providing directionality, they can often increase the number of antibodies immobilized and ensure a strong anchoring to the device [17].

Some designer SAM's have been developed to directionally capture the Fc fragment of an antibody. One example is the calix-crown SAM [23]. While these molecules are fairly expensive, they allow for directional immobilization of antibodies. In addition, an antibody can also be tagged with a linker molecule on its conservative end. Tags such as biotin (biotin-avidin affinity), avidin (biotin-avidin affinity) [5,24], histidine (His-Ni-NTI affinity) and thiol (disulphide bond formation or sulphur-gold affinity) [17] are all common tags for antibodies. By immobilizing the tag's complementary component, a tagged antibody can subsequently immobilized.

It is not necessary to immobilize an entire antibody to capture its complementary antigen. Parts of antibodies, or fragments, are sufficient for molecular recognition. Several sites exist where the proteins can be cleaved while maintaining functionality. Maintaining functionality of the Fab fragment is required however. Fragments can be immobilized onto surfaces in similar ways as whole antibodies (with the the exception of any immobilization procedure that targets the Fc domain) [17]. The largest drawback with the use of fragments is that they are relatively expensive in comparison to whole antibodies. However, they offer improvements in terms of surface densities, while reducing the amount of unnecessary protein on the sensor's surface.

Another advantage of antibodies is that they often can be reused. The antibody will release the antigen by modifying the environmental pH appropriately [7]. The sensor can then be used to detect the presence of the analyte again. However, in general, antibodies are expensive to produce and are prone to environmental damage. In addition, in order to ensure selectivity, monoconal antibodies should be used as opposed to polyconal ones [7].

Monoconal antibodies will only attach a single antigen, while polyconal ones will attach several similar antigens. As such, the use of polyconal antibodies can result in false positives.

1.4.2 Single Strand DNA

Surfaces can also be functionalized with ssDNA in order to create genetic sensors [5]. The sensors exploit the high specificity that a ssDNA will have for its complementary strand. If a certain strand of ssDNA is immobilized on a surface it should only bind with its complementary strand. This makes it simple in terms of capturing specific coding sequences. For the detection of bacteria, typically only certain sequences that are characteristic of the bacteria are targeted for detection [14].

There are several different methods for immobilizing ssDNA to a surface. A simple approach is to attach a thiol group on a desired ssDNA to attach it onto a gold surface [25]. Advances in microarray fabrication have enabled several commercial fabrication methods. These include variations on photolithography and ink-jet printing. Each method is typically proprietary of a specific microarray system fabricator [14, 15]. Due to surface interactions, it is important to design the ssDNA to have an extended region of nucleotides close to the surface. This ensures proper hybridization between the immobilized strand and the strand to be detected. Without the extended region the surface can interfere with the DNA hybridization process [25].

One advantage of using ssDNA is that the sensor is easily regenerated simply heating the device to the DNA's melting point. By doing so, the bonds between the complementary strands break, and the strand that is not immobilized can be washed away. Furthermore, it is possible to multiplex sensing in large arrays because of the specificity of ssDNA [14].

However, using ssDNA still requires a lengthy, laboratory intensive process in terms of bacterial detection. This process involves lysing the bacteria, isolating the DNA and mechanically shearing it in order to produce small linear strands. Also depending on the quantity of bacteria, prior bacterial enrichment or PCR might be necessary. Furthermore, unlike the colony counting method, unviable (dead) cells can still provide sufficient DNA to cause a false positive [3].

1.4.3 Surface Blocking

While much of the focus in surface functionalization has been on capturing a specific biological entity, it is also important to prevent the adsorption of other, undesired entities

[24]. Not only is it important to capture one type of bacteria, it is also important to prevent the adsorption of other types. This ensures the specificity of the sensor.

There are several different ways to block a surface. Bovine serum albumin (BSA) and casein (as pure casein or skim milk powder) have been successfully used in ELISA's for blocking [26]. Several different efficiencies have been reported in terms of their successful blocking ability. Most biosensors reported in literature use BSA or Casein as a blocking agent [26]. Other blocking buffers are also available for purchase [27]. The blocking agent is typically adsorbed to the surface after the immobilization of the probe. However, some blocking agents can be modified so they can be incorporated into the surface immobilization procedure [24]. In this case, the use of a SAM or tag can help enhance the the adsorption of the blocking agent and/or probe.

Small molecules can also be used for blocking. For example, ethanolamine is often used to inactivate unbounded amine binding regions. The hydroxyl group are known to reduce subsequent adsorption [28]. Furthermore, several different polymeric molecules have been used for blocking: poly(ethylene glycol) (PEG) is the most commonly used [26, 29]. A thiol or silane group is typically coupled with a PEG to help anchor it on a gold or silicon surface, respectively. Furthermore, mixed SAM's can be form with PEG molecules and probe capturing molecules, which makes for specific biofunctional surface [29]. The main drawback in using PEG designer molecules is their high cost compared to BSA or casein blocking. Furthermore, obtaining an optimal blocking procedure is difficult using covalently attached polymers mixed with bio-recognition probes.

1.5 Types of Biosensors

1.5.1 Overview

There are many different types of transducers that can be used as biosensors. Several different transduction methods have been developed levying either optical, inertial, electrical and/or chemical effects. Outlined below are several transducers often used as biosensors. These include quartz crystal microbalance (QCM), surface acoustic wave (SAW) sensors and surface plasmon resonance (SPR). In addition, microcantilever based sensors will be discussed in detail in Chapter 3. Table 1.1 shows an overview of the advantages and disadvantages of these sensors.

Table 1.1: Overview of Several Biosensor Transducers

Sensor	Advantages	Disadvantages
QCM	Inexpensive	Large
	Easy fluidic integration	Large viscous damping
	Well established	Low sensitivity
SAW	Medium sensitivity	Piezoelectric substrate
	Easy microfluidic integration	Sensitivity reduced by guiding layer
	Little viscous damping	
SPR	Sensitive	Detection 300 nm from surface
	Real time detection	Bulky optical systems
	Easy fluidic integration	
Cantilever:		
Resonant	Very high sensitivity	High viscous damping
		3-D structure
		Fragile
Deflection	High sensitivity	3-D structure
	Easy fluidic operation	Fragile
		Requires blocking 1 side

1.5.2 Quartz Crystal Microbalance

QCM is a type of sensor that detects an additional mass. These devices are commonly used as thin film thickness monitors during deposition [30, 31]. QCM devices are simply piezoelectric discs with electrodes on opposite sides. For biosensing purposes, QCM devices are often coated with gold in order to simplify biofunctionalization [25]. The piezoelectric disc can be mechanically resonated by applying an alternating electric potential. This resonance has a strong dependence on the mass of the device. If a mass is added, the frequency of oscillation will decrease. The amount of added mass onto the device can then be correlated to frequency shift [30, 32]. A schematic of a QCM device is shown in Figure 1.3.

Several different bacterial sensors have been developed around QCM technology. Wu *et al.* functionalized QCM device with ssDNA. This was fully integrated with fluidic systems to detect *E.coli* O157:H7. The system was coupled with PCR in order to bring genetic material to detectable quantities [25]. Shen *et al.* were able to detect 750 cfu/mL of *E. coli* W1485 [33]. This was accomplished by modifying the QCM device with both lectin and carbohydrate receptors specific to the strain of interest. Su *et al.* reported the detection of *Salmonella* Typhimurium using a Protein A and antibody functionalized QCM device. Furthermore, by concentrating the bacteria using magnetic beads and

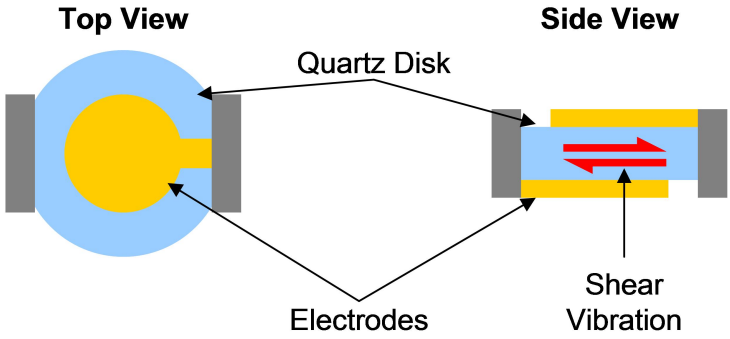

Figure 1.3: A typical QCM Sensor. When a mass attaches to the devices a reduction in the frequency of oscillation can be measured.

subsequently monitoring the frequency and motion resistance their device was able to detect bacteria concentrations of approximately 100 cfu/mL [34]. Poitras and Tufenkji studied the frequency shift and the dissipation effects of adsorption during the detection of *E. coli* O157:H7. However, they did not achieve competitive minimum detectable concentrations [2].

QCM devices have the advantage of being simple to fabricate and relatively easy to integrate with fluidic systems. Furthermore, both the input and output signals are electrical, which makes integration with electronic interfaces simple. However, QCM devices are not very sensitive in terms of minimum detectable masses compared to other mechanical sensors [32]. Also, the sensitivity of the device is reduced when operated in liquids due to damping effects [2].

1.5.3 Surface Acoustic Wave Sensors

SAW's are acoustic waves that are constrained to the surface of a device. These devices are typically created by fabricating four electrodes on the surface of a piezoelectric substrate. Two of these electrodes generate a propagating wave by creating a waveform by applying voltages appropriately. The other two electrodes are on the other side of the chip and are used to readout the transmitted wave. The frequency of this wave can be shifted by the adsorption of a mass on the surface. Figure 1.4 shows a schematic of a SAW sensor. Depending on the orientation of the piezoelectric substrate an in-plane shear or an out-of-plane Rayleigh waveform can be constructed [35]. Shear waves are of the most interest for biosensing applications because of their minimal interaction with surrounding liquid [27, 36]. The sensor is typically coated with a guiding layer. The wave will actually

propagate in the guiding layer and the resulting acoustic wave is called a Love wave. This also provides isolation of the electrical components to the fluidic environment. This guiding layer, which can be a polymer or a thin film, can then be functionalized with a probe. Both the mass and stiffness of the guiding layer effect the device sensitivity [37]. Any captured mass will cause a downwards frequency shift. Furthermore, SAW sensors are predicted to have a better mass sensitivity than QCM [32].

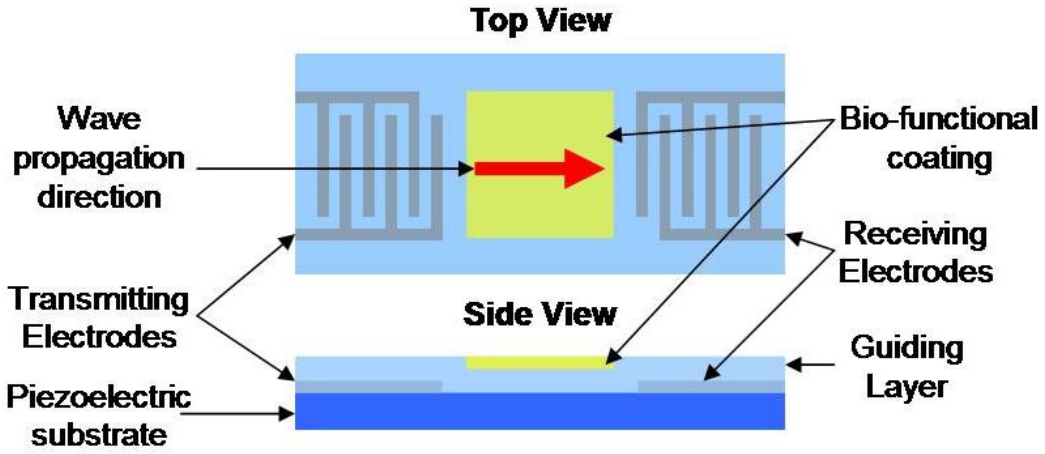

Figure 1.4: A typical SAW wave sensor. For biosensors, Love wave sensors are often used. A Love wave is a shear wave that is propagated in the guiding layer.

While SAW sensors are relatively well established, little work has been performed in terms of bacteria detection. Moll *et al.* detected *E. coli* bacteria with an antibody functionalized Love wave sensor. A minimum concentration of 1000 cfu/mL was realized [27]. However, further device optimization is expected to yield better results.

There are several advantages to SAW biosensors. These devices can be integrated into microfludics, which can lead to full lab-on-a-chip systems. Furthermore, fluids do not significantly reduce their sensitivity unlike most mechanical sensors [27]. The properties of the guiding layer however can have a huge effect on the device's sensitivity [37].

1.5.4 Surface Plasmon Resonance

SPR levies the interaction of light with a metal thin film deposited on a glass substrate. When light strikes the metal film at various angles, there exists an angle at which the maximum amount of light is absorbed by the metallic film. This is called the surface plasmon resonance angle and physically corresponds to the interaction of light and the electrons of the metal surface. This excites electromagnetic waves that propagate near

the surface which are called surface plasmons. This effect is dependant on the index of refraction in close proximity to the metal: only a change in the index of refraction within the evanescent field will effect the SPR angle [38, 39]. When a molecule is adsorbed or attaches to the surface, it changes the local index of refraction [40]. This will cause a shift in the SPR angle.

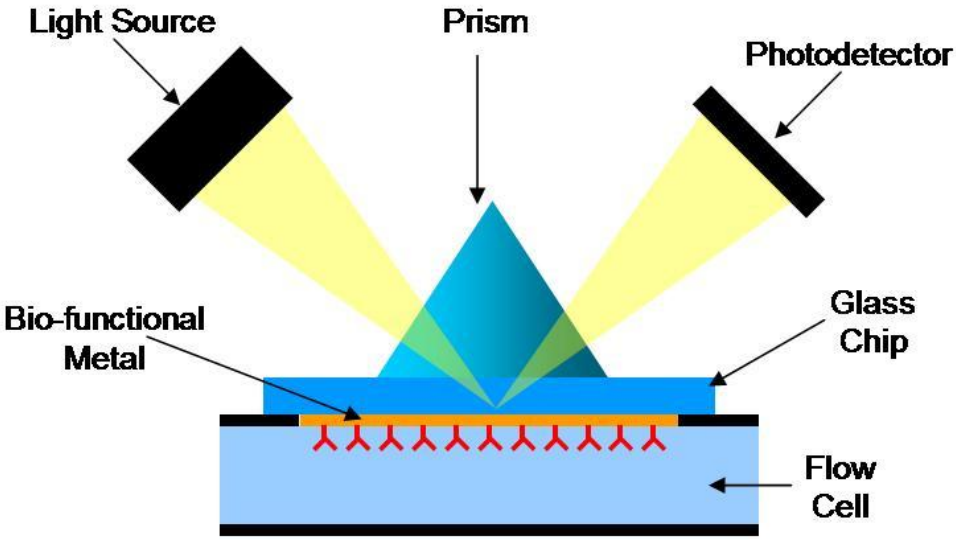

Figure 1.5: A typical SPR setup. When the functionalized metal surface captures analytes from the flow cell, a change in the local index of refraction occurs. This causes a detectable shift in the SPR angle.

Several detection groups have used SPR to detect bacteria. Taylor *et al.* detected four types of bacteria concurrently using a multichannel SPR device. The minimum detected concentration was 3400cfu/mL, however this varied from bacteria to bacteria [41]. Most bacteria capture experiments using SPR required high bacterial concentrations (10^7 cfu/mL) to produce any signal [7]. Poor detection limitations are attributed to low antigen surface concentration and relatively slow bacterial diffusion. However, Waswa *et al.* predicted the detection limits based on their data to be approximately 25 cfu/mL for *Salmonella* and *E. coli* using a Biacore SPR system [4].

Only changes of the index of refraction within the evanescent field can be detected by SPR. This field only exist close (300nm) to the surface [38]. Due to the large size of a bacteria, only part of the bacteria is in the evanescent field, which ultimately limits SPR's sensitivity to bacteria [7, 38]. Several methods are being developed to improve the sensitivity of SPR [39]. Also, SPR systems generally rely on bulky optical systems, which limit their amenability to full microfluidic integration.

1.6 Summary

This chapter has outlined several different conventional and new approaches for bacteria detection. Culture, immunological and genetic methods of bacteria detection have all been discussed. These methods are sensitive but take significant time and resources to carry out. Biosensor based methods have also been explored in terms of surface modification and common transducers used for the detection of bacteria. Several different studies were also reviewed that involved the detection of bacteria.

2

Introduction to Bacteriophage Biotechnology

2.1 Introduction to Bacteriophages

Bacteriophages (also know as phages) are classes of viruses that specifically infect bacteria. They are considered one of the most abundant naturally occurring biological entities and are massively diverse. Phages can be found everywhere including water, food and soil. However, because they only infect bacteria, they pose little direct threat to other species. Everywhere that bacteria are found in significant numbers, often there are phages. Phages have evolved along with their bacteria counterparts and thus many different types of phages exist. Some phages have evolved to be specific to bacteria at the strain level, while others can infect a much larger range of bacteria [42, 43].

The phage was discovered independently by Frederick Twort and Felix d'Herelle in 1915 and 1917, respectively [42, 44]. Their existence and nature was debated for sometime until the advent of the electron microscope. This proof explained why some natural water supplies had antibacterial properties and several other microbiology mysteries. Phages are robust viruses and stable enough to infect bacteria, often a decade after their assembly [42].

Phages are complex macromolecules comprised mostly of proteins and genetic material. Some phages also have bilipid membranes, however this is not common. Both DNA and ribonucleic acid (RNA) based phages exist, however DNA based phages are more common.

Phage are inactive unless a host bacteria is present. The phage can then infect a bacterium by incorporating its genomic information into the host cell. This typically causes the host bacteria to begin to produce more of the phage virion. This results in the propagation of the phage [42].

There are two major structural classifications of phages: tailed phages and filamentous phages [42,43]. Most phages are tail based phages. Phages are very diverse, ranging in size from twenty nanometers to hundreds of nanometers and can carry anywhere from twenty to hundreds of genes [42]. Figure 2.1 shows a scanning electron microscope (SEM) image of a common tailed phage, the T4 phage.

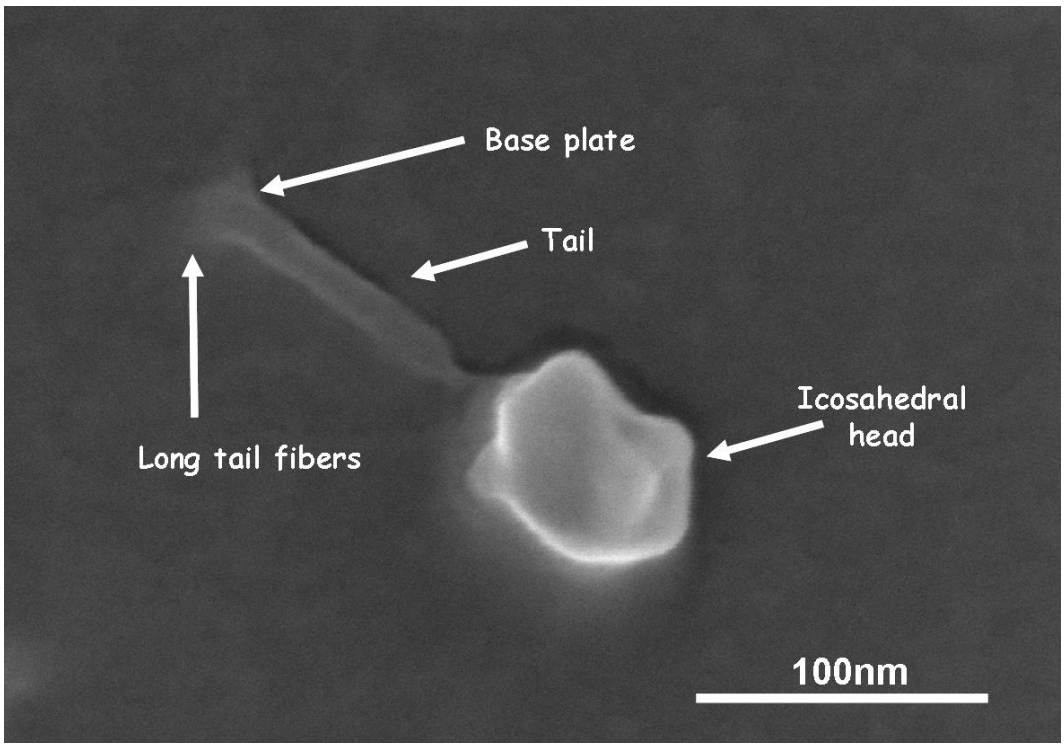

Figure 2.1: A SEM image of a T4 phage on a silicon surface. The phage was fixed, dehydrated and sputter coated with 3nm of chrome.

Recent applications of phages in biotechnology include alternatives for antibiotics [42], massively parallel protein binding assays [42, 45], molecular transport for gene and drug delivery [42,46], and molecular recognition [42,47,48]. These applications will be explored in detail after reviewing the basic biology of phages.

2.2 Phage Structure and Function

2.2.1 Tailed Phage

Tailed phages are the largest group of phages, representing up to 95% of phages. Tailed phages can be broken down into several structural components. These can include the phage head, tail, base plate and tail fibers. In a tailed phage, the head is where the genetic material, typically DNA, is stored. The head of the phage is comprised of several repeating structural proteins. The head acts as a protective shell for the genetic material [42].

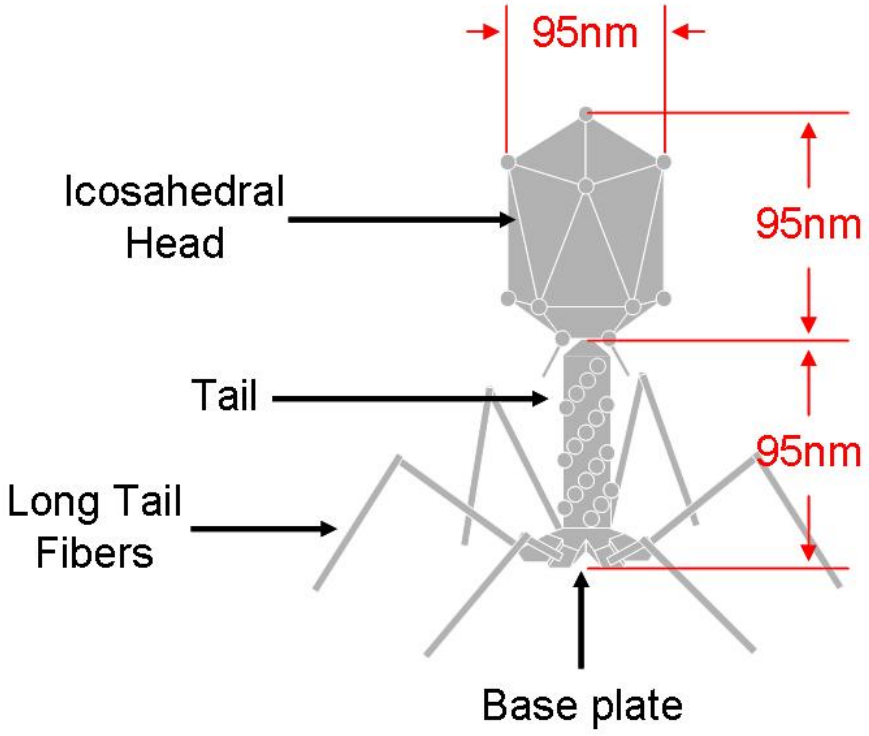

Figure 2.2: The structural components of a T4 Phage. Many dimensions vary between phage types and many have less components.

Tailed phages have significant variations in the structure, length, and function of the tail. The tail supports the bacterial binding site [42]. Some tails actually contract, which facilitates transportation of the genetic material into the host. For example, the T4 phage tail will contract after successfully attaching to its host. The mechanism has even been proposed as a possible organic actuator in microfabricated devices [49]. Tails that contract are typically longer and ridged. Other phages have long tails that do not contract and are

flexible. In addition, some phages have relatively short tails that are neither flexible nor contractible [42].

At the end of the tail, there are proteins that enable the infection of the host cell. More complicated phages (like the T4 phage) have several structures including a base plate, short tail fibers and long tail fibers [50, 51]. The structure of a T4 phage is shown in Figure 2.2. All of these structures play a role in the infection process. Phages like P22 in contrast rely on short tail fibers (often called tail spike proteins) [52]. These proteins recognize and bind to the host bacteria. Furthermore, the phage tail often exhibits enzymatic activity to locally break down cell wall. This helps facilitate the transport of the phage's genetic material into the host bacteria [42].

2.2.2 Filamentous Phage

Filamentous phages differ significantly from tailed phages, however several similarities in function can be seen [42, 45]. The filamentous phage consists of a long tubular structure with two ends, one of which can infect bacteria. The long structure consists of many repeating pVIII proteins, which represents most of the phage's mass. The protein creates a long tubular structure that is about 2nm thick. The inside of the tubular structure houses the phage's DNA. The length of the phage is typically proportional to the number of nucleotides in its genome; there are 0.435 pVIII proteins per nucleotide. This corresponds to about 0.1435nm per nucleotide [45]. The M13 phage is a common filamentous phage and a schematic of it is shown in Figure 2.3.

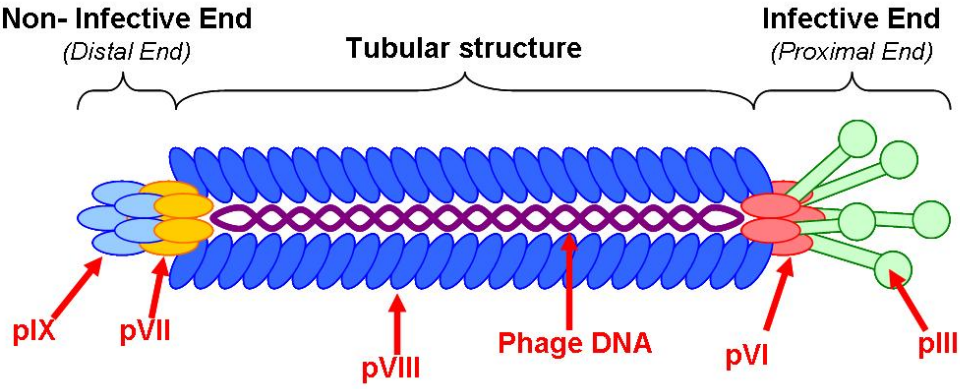

Figure 2.3: The structural components of an M13 phage.

The non-infectious end of filamentous phages is comprised of five pVII and five PIX proteins. This end is the is the origin of DNA packing and is assembled first. The infectious

end, much like the end of a tailed phage, has proteins that recognize and bind to the host. This consists of five pIII and pVI proteins. Often, these phages use pili to recognize a host bacteria for binding. This is followed by the integration of the phage into the cell wall of the host bacteria [45].

2.2.3 Other Phages

Several other classifications of phages exist, however they are less common and not as prevalent in the biotechnology industry. For instance, there are several different smaller RNA based phages including R17, MS2 and F2. These phages often infect cells at the base of the pilus. Several small DNA based phages will also attach to the pilus of a bacteria. Some smaller phages, like PRD1, also incorporate lipid membranes into there structure. Normally, these lipids are taken from the host bacteria's cell membrane during the phage's assembly. Mycoplasma bacteria (small bacteria that lack a cell wall) can be attacked by different phages that resemble that of animal viruses. The phages will bind directly to receptors on the cell membrane. These bacteria are typically not susceptible to most antibiotics, but can be infected by their phages with great efficiency [42].

2.3 Infection

2.3.1 Initial Recognition and Infection

The first step in phage infection is the attachment of the phage to the host cell surface. This is typically accomplished by the recognition of a receptor on the outside of the bacterial cell wall such as an antigen, pilus or other structure. There is much variability from phage to phage in terms of which receptor they bind to. For example, the P22 phage binds to a polysaccharide receptor know as the O-antigen common to *Salmonella* [3,42,52,53], while χ-phage infects *Campylobacter jejuni* by means of the base of the flagellum [54].

Initial recognition is often achieved by specific protein(s) at either the tail or the infectious end. These protein(s) are generally responsible for recognition, binding, and digesting part of the bacteria's cell wall. This mechanism varies from phage to phage [42]. For example, the infection process of the T4 phage is relatively complicated. The long tail fibers initially recognize the receptors on the host bacterium's cell wall. This is a reversible reaction that is used to orient the phage. For infection to occur, at least three of the six long tail fibers must be bound to the cell wall. Once this occurs a change in the phage's base plate is observed, which allows the short tail fibers to bind the cell wall. The tail

subsequently contracts in response. This exposes the tail's lysozyme to the cell wall, which locally digests it to facilitate the phage DNA transport into the host [50, 51].

2.3.2 The Lytic Cycle

After the successful transport of the phage's DNA into the cytoplasm of the bacteria, it is often incorporated into the bacteria's chromosome. The bacteria then enter one of two phage induced cycles: the lytic cycle or the lysogenic cycle. The lytic cycle involves the over expression of the phage proteins [42]. This happens sequentially, which allows the phage assembly to take place.

In tailed phages, this often begins with the head and the tail proteins independently. Once the head is assembled, the phage DNA is packed in. The tail subsequently attaches to the head. Once this is complete smaller extremities are added to the tail, for example, in the case of the T4 phage, its tail fibers. Phages remain in the bacteria as other phages are produced concurrently. Digestive enzymes encoded in the phages genome are eventually activated and transcribed, which causes the lysis of the host bacteria. This releases the newly assembled phages into the environment, each of which can infect a new host bacteria cell [42, 50]. T2 and T4 phages are common lytic phages.

2.3.3 The Lysogenic Cycle

Many phages have evolved the ability to coexist with their host in a non virulent way. This allows the phages to enter the lysogenic cycle. The phage virulent genes are essentially repressed by other proteins encoded in it. When this occurs the phage's added DNA segment is called prophage. While the new DNA generally does not transcribe any proteins involved in phage assembly it can contain several other genes that are still active. These genes typically are repressor proteins for other genes in the prophage, but may also change the phenotype of the the bacteria. These could give the bacteria an new antibiotic resistance or turn a harmless bacteria into pathogenic one [3, 42].

Phages that enter the lysogenic cycle are called temperate phages. However, when stress is induced on the phage, such as UV light exposure or starvation, they may enter the lytic cycle. This will often cause massive assembly of phage particles followed by the lysis of the cell. In addition, many filamentous phages can be created during the bacteria's life cycle. These phages typically are assembled on the cell membrane and eventually excreted out without destroying the bacteria. Furthermore, these phages allow the bacteria to divide, which also replicates the prophage in the bacterial chromosome. This can result

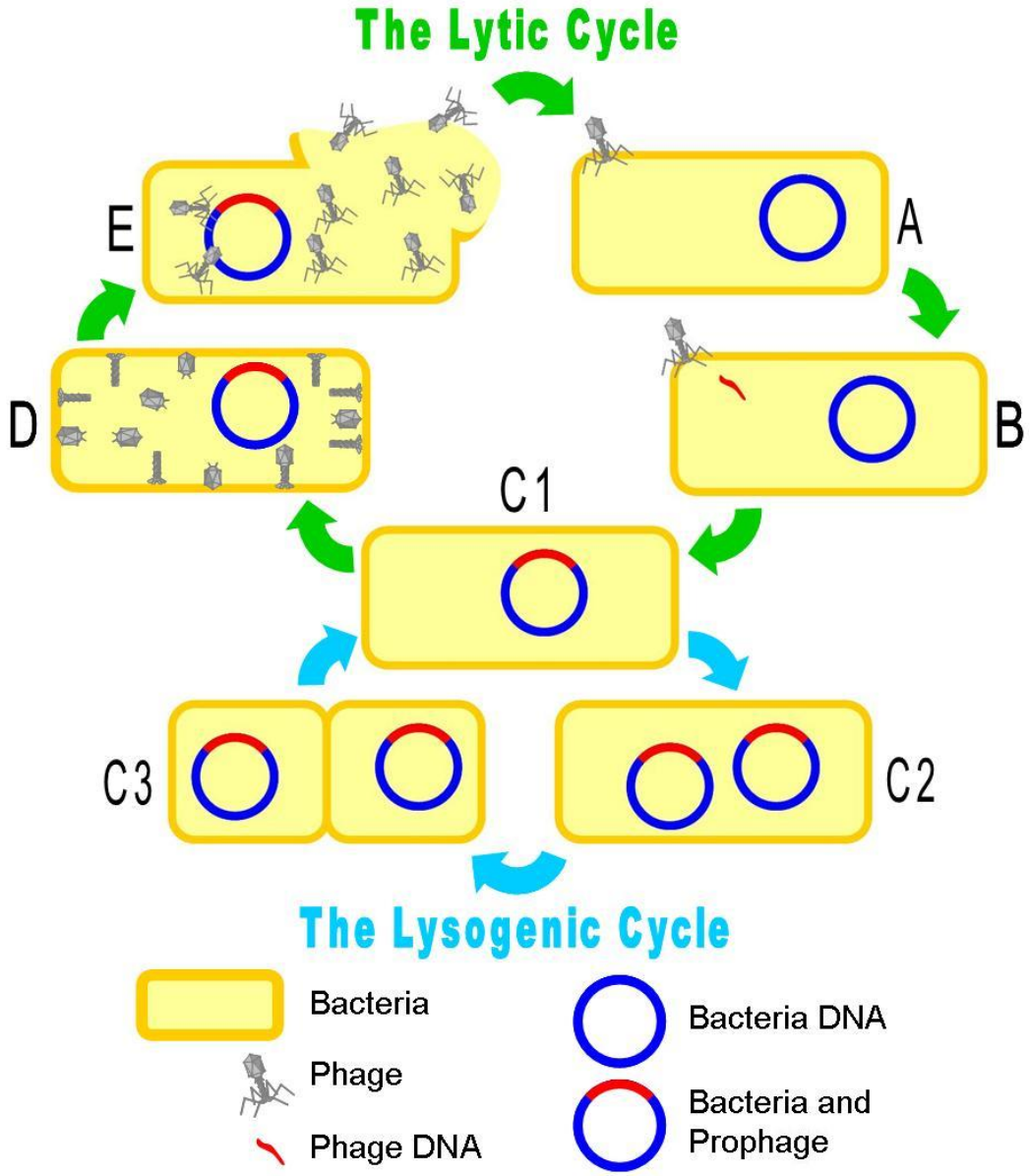

Figure 2.4: The phage life cycle may consist of both the lytic and lysogenic cycles. A: A phage recognizes its host bacteria. B: The phage infects the host bacteria. C1: The phage's DNA integrates with the bacteria's chromosome. The bacteria can then either enter the lysogenic cycle (C2) or the lytic cycle (D). C2: Bacteria undergoes normal growth, with many of the phage's genes repressed. Copies of the prophage are replicated when preparing for cell division. C3: The bacteria divides into two infected cells. D: The beginning of the lytic cycle. A bacteria will enter the lytic cycle if it is a lytic phage or some external stress was applied to a bacteria infected by a temperate phage. As such, the phage proteins begin to assemble on the cell membrane. As this progresses, the parts assemble into full phages. E: Late in the lytic cycle, enzymes are produced to break down the cell, which eventually causes lysis. This releases free phages that are able to infect other host cells.

in thousands of phages being produced from a single host [42, 55]. Figure 2.4 shows both the lysogenic and the lytic cycles.

2.4 Phage Nanobiotechnology

2.4.1 Phage Display

Phage display is a biological combinatory method to assess binding interactions between proteins [42,45]. This process is widely used in drug development in order to quickly assess binding properties of many proteins to a certain test protein [42,45,56]. Filamentous phages are most often used in phage display. Large tailed phages have been used to investigate the interactions of larger proteins [42].

This relies on the highly repetitive structure of the tubular or head portion of the phages. Because these proteins are mostly protective in nature, changing the externally expressed portion of the protein does not adversely affect the phage. Phage libraries can then be created of phage mutants that are genetically modified to express different proteins. These phage libraries can have thousands of different proteins expressed on the phages [42, 45].

While there are several variants of phage display, it is often implemented by coating a substrate with the protein of interest (this is called substrate phage display). The substrate is then exposed to a phage library and binding is allowed to occur. The substrate is then washed so that only surface bound phages remain. These phages are then eluted from the surface by change in pH. The DNA of the phages that attached to the surface are then isolated and analyzed to determine their expressed protein. The type of protein expressed on the phages that bound to the surface can then give insight into the interactions between substrate protein and the phage mutant capsid protein [42, 45]. This process is illustrated in Figure 2.5.

2.4.2 Phage Therapy

One of the first pieces evidence of for the presence of phages before their discovery was an observation that several natural water sources had anti-bacterial properties [42]. It is now known that phages were responsible for this property. Phages were of interest for their ability to kill pathogenic bacteria shortly after their discovery. The concept involved mixing many different types of lytic phages into a phage cocktail. The mixture could then be used to ward off subsequent infections. However, with the discovery of antibiotics, most

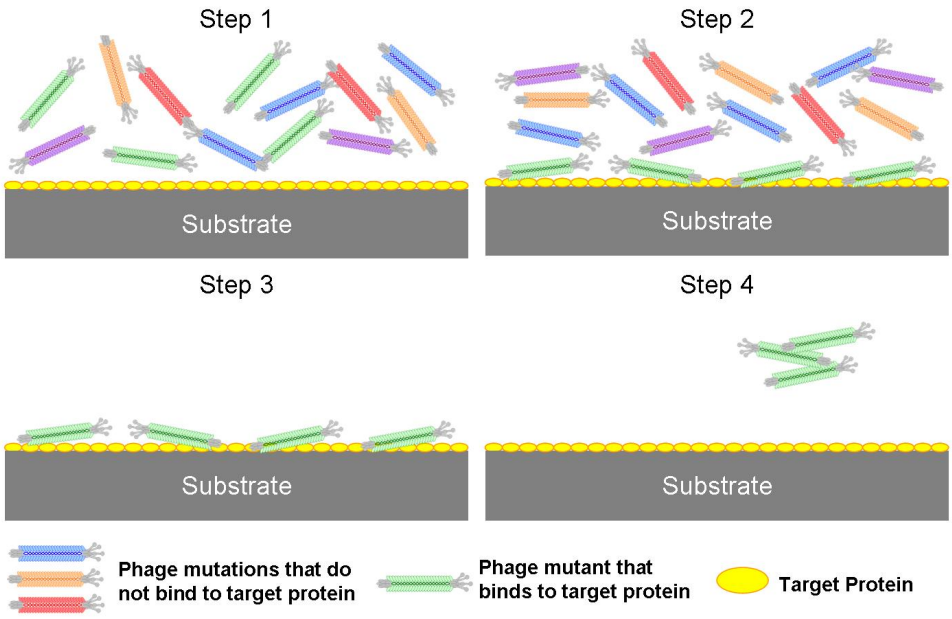

Figure 2.5: Substrate phage display. Step 1: A substrate is coated with a protein of interest and then exposed to a phage library. A phage library is a collection of phages with random proteins expressed on either their head (tailed phages) or PVIII (filamentous phages). Step 2: Phages with proteins that bind to the target protein attach to the surface, while others stay in solution. Step 3: Unbound phages are washed away. Step 4: Bound phages are eluted by changing the pH. These phages are collected and their DNA is sequenced. This can be used to determine which protein is present on the phage that attached to the substrate protein.

Western researchers abandoned this concept. But therapeutic phage research continued in the Soviet Union at that time [42, 57–59].

Phage therapy research is gaining renewed interest because of recent increases in antibiotic-resistant strains of bacteria. Because phages bind to specific receptors, bacteria can evolve immunity to that phage by modifying or losing that receptor. However, this is often seen as disadvantageous for the survival of the bacteria. Therefore, it is significantly more difficult for a bacteria to develop resistance to a phage compared to an antibiotic. Furthermore, because of the diversity of receptors that phages can bind to, if a bacteria gains immunity to one phage it will still be susceptible to other phages that target different receptors [42, 57–59].

Phage cocktails are being effectively applied to food in order to prevent bacterial contamination in many parts of the world. However, the application of phage cocktails in human medicine is limited at the time [57].

2.4.3 Phages for Molecular Transport

Phages are essentially molecular machines designed to store and carry genetic material until they find a suitable host. As such, phages make excellent candidates for the genetic modification of bacteria. The phage infection mechanism can be used to modify the chromosome of its host bacteria [42]. Temperate phages are typically the most useful for transfection, as they do not necessary end in the lysis of the bacteria.

Phages can not infect mammalian cells and they exibit little natural binding affinity for to them. However, a mammalian cell can be targeted by expressing a protein on the capsid of the phage that binds to a particular receptor. The cells can then take in the phage through endocytosis. While some promising results have been seen, transfection efficiencies were typically low. Additionally, multiple targeting proteins can be expressed on the phage, allowing for higher specificity and transfection efficiencies [42].

Phages also have been shown to have some promise in advanced drug delivery mechanisms. By designing the phage capsid protein, phages (or their proteins) can be structurally incorporated into lipid based micelles. These are designed in such a way that a specific targeting protein would face outwards on a micelle. These micelles can either carry drugs or genes to be delivered to a target cell [46].

2.4.4 Phages as Probes in Biosensors

As seen in Chapter 1, antibodies have many limitations as probes for bacterial biosensors. They are expensive to produce and purify, susceptible to environmental damage and limited in terms of bacterial selectivity. As such, phages have been recently investigated as biosensor probes. Phages offer more tunability in terms of selectivity than antibodies, are easy to produce and are environmentally robust.

Several initial studies have investigated the use of phages in pathogen detection. Initial investigations revolved around variants on phage display. However, more recently Handa *et al.* designed a ELISA for *Salmonella typhimurium* by anchoring P22 phages on ELISA wells [60]. They accomplished this by capturing phages using EDC and NHS crosslinkers to target free carboxyl groups on the phage.

Phages have also been attached to particles for the detection of bacteria. Sun *et al.* reported the attachment of phages to latex micro beads [61]. Beads were then found to specifically bind to host bacteria. This would allow for the labeling of bacteria with different particles for fluorescent detection or magnetic separation. In addition, Mossier-Boss *et al.* reported the production of fluorescently labeled P22 phages for the detection of *Salmonella* Typhimurium [62]. The P22 phage's DNA was labeled with SYBR gold nucleic acid stain, which during infection, was transmitted to host bacteria. Since bacteria cells are typically infected by multiple phages, the stain concentrated in host bacterial cells.

Wan *et al.* used a f8/8 library phages with magnetoelastic biosensors [63, 64]. Phages were physically adsorbed onto iron oxide sensor surfaces. The devices were resonated in buffer to detect bacteria. Advantages of such a biosensor are that it can be operated wirelessly, it is easily regenerated and the devices were still active after drying. However, the sensor suffered from drift and significant viscous dampening. Lankshamanan *et al.* used a similar system to detect *Samonella typhimurium* in fat free milk [65]. For this work, a phage mutant was selected from an f8/8 phage library. Nanduri *et al.* also physically adsorbed f8/5 phages to QCM devices for the detection of *E.coli* [66]. They used the QCM device to study and develop a model for the kinetics of phage-bacteria binding.

Yang *et al.* covalently attached M13 phages to QCM devices. Immobilization was accomplished by depositing a thin film of gold on the sensor followed by a designer thiol molecule to react with free amine groups. A multilayer of phages was reported with about 1000 phages per micron square. An antibody known to bind to M13 was then detected in concentrations as low as 7 nM [67]. Yang *et al.* immobilized phages on gold electrodes using a similar chemistry to sense molecules attaching to the phages by measuring changes in impedance [68]

Gervais *et al.* detected *E. coli* bacteria using genetically modified T4 phage on an electrical impedance sensor [44, 69]. These phages were modified to specifically express biotin on their capsid head. Phages were then immobilized on electrodes by gold functionalized with biotin and streptavidin. Gervais then modified the immobilization procedure (similar to Huang *et al.* except using phages instead of antibodies [70]) in order to integrate the blocking layer into the sensor functionalization. This was followed by specific detection of *E. coli* EC12 using T4 phages on microcantilever sensors [44].

Shabani *et al.* also worked with T4 phages, expect phages were immobilized on oxidized carbon electrodes [71]. Phages were then anchored by EDC coupling for 10 minutes. Ultimately, the sensor achieved a minimum detectable concentration of 1000 cfu/mL. The peak signal was achieved around 20 minutes, which was expected based on the T4 lytic cycle.

2.5 Summary

This chapter has discussed the basics of phage biology and technology. The basic nature and structure of common phages has been briefly outlined. This includes the structure and function of the components of a phage. The infection process of both lytic and lysogenic phages has also been outline. Several different prominent and promising phage-based technologies have also been discussed. These include phage display, phage therapeutics, phages for molecular transport and phages as probes in biosensors.

3

Mechanical Vibrations and Micro/Nano-Cantilever Sensors

3.1 Overview

As outlined in Chapter 1, there has been great efforts to develop sensitive and selective bacterial sensors. One promising platform with respect to potential sensitivity is the microcantilever sensor. A cantilever consists of a beam supported at one end, much like a diving board. A cantilever structure is shown in Figure 3.1. Macro-scale cantilevers have been used in various load cells to sensitively determine applied forces. This is typically accomplished by monitoring the bending of a long cantilever with low stiffness.

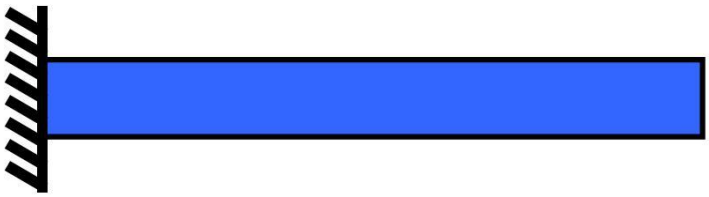

Figure 3.1: A cantilever beam is a structure that is clamped at one end and free at the other.

The advent of the Atomic Force Microscope (AFM) first showcased the potential of microcantilevers as sensors. Microfabricated cantilevers were used in conjunction with macroscopic elements that allowed the fast and precise movement of the cantilever. On the

end of the microcantilever is a sharp point that is brought into contact with the sample. A laser is then reflected off the back of the cantilever and received by a split photodiode. This optical lever setup allows precise measurement of the cantilever's deflection. The point of the cantilever was used to probe the surface by measuring the surface-tip interaction forces. These forces are proportional to the beam deflection. This deflection can then be mapped over an entire surface to image its topography [72,73]. The AFM has even achieved atomic resolution under ideal conditions [74].

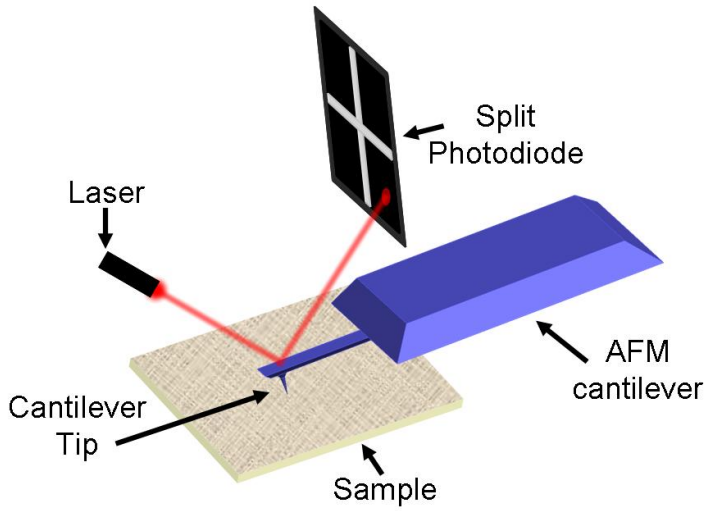

Figure 3.2: The Atomic Force Microscope (AFM). A cantilever with a sharp tip is brought in contact with the surface being imaged. A optical lever system measures the deflection of the cantilever while it is scanning the surface. The deflection profiles can then be mapped to create an image of the surface.

To image loosely bound molecules on a surface, tapping mode AFM was developed. Tapping mode uses a microcantilever in resonance to determine the surface topography. Changes in the resonant frequency are used to map the tip-surface interaction forces. This minimizes the lateral forces on the sample allowing the imaging of physi- and chemisorbed species [72,73].

In addition, microcantilevers have been shown to be sensitive for the measurement of both stress and mass loading. Surface stresses can be detected in the deflection mode of cantilever sensors. In this case, a differential surface stress will cause the bending of the cantilever [75,76]. Additional mass on the microcantilever can be detected by exploiting the inertial dependance of its resonant frequency. These are called resonant mode cantilever sensors. As such, a change in the mass of the cantilever will result in a change in the

resonant frequency. Both of these methods show great potential for the development of commercial biosensing platforms [75–77].

3.2 Fabrication

3.2.1 Overview

Like most microelectromechanical systems (MEMS), microcantilevers are fabricated using conventional microfabrication processes. This is performed through a series of deposition methods including evaporation, sputtering or chemical vapor deposition [78]. Patterning of the structures is usually achieved by optical lithography. Fabrication of nanoscale cantilevers can however involve electron beam lithography or self assembly. Two common microfabrication methods used to fabricate microcantilevers are briefly reviewed.

3.2.2 Bulk Machining

Bulk machining techniques consist in patterning of a substrate to form the mechanical structure. Silicon is typically used given the extensive number of fabrication processes developed by the microelectronics industry. Bulk machining process are used for devices that require a thick mechanical layer or single crystal material structures. Most commercial AFM cantilevers are fabricated using bulk machining methods.

Many bulk machining processes exploit wet etches that preferentially etch certain orientations of the silicon crystal. Single crystal silicon is etched much faster in the silicon $< 100 >$ plane than the $< 111 >$ plane by both KOH and TMAH [79]. Furthermore, by doping the silicon, the $< 100 >$ etch rate can be drastically reduced. Such doped layers can be used as etch stops to control the device's thickness [80].

A standard microcantilever bulk machining process can be summarized as follows:

1. A resist or masking layer is placed on a $< 100 >$ silicon wafer that is polished on both sides.

2. The resist or masking layer is patterned, defining the cantilever structure.

3. The top layer of silicon is etched to the desired thickness.

4. The resist/mask is removed, and a protective layer is deposited on the top of the structure. A masking layer is deposited on the back side and a window is patterned on the back, the cantilever.

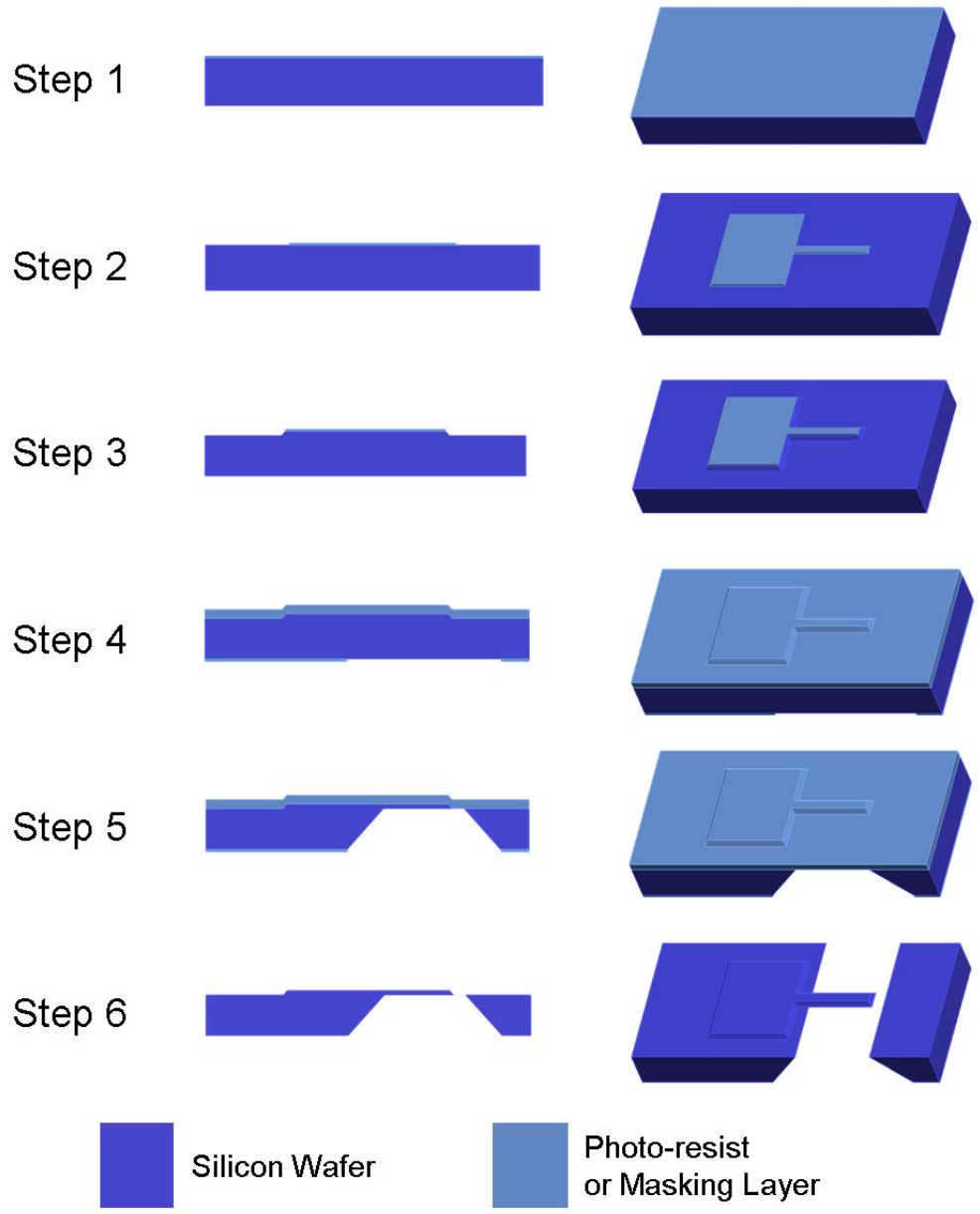

Figure 3.3: A typical bulk machining process. Step 1: A masking layer is deposited on a doubly polished $< 100 >$ silicon wafer. Step 2: The masking layer is patterned to define the cantilever structure. Step 3: The cantilever is formed by etching into the silicon wafer. Step 4: The masking layer is removed and a protective layer is deposited on top of the cantilever. Another masking layer is defined on the backside of the wafer and a pattern is created to form a releasing window for the structure. Step 5: The cantilever is wet etched from the back to release the cantilever. The etch depth is controlled using an etch stop dopant. Step 6: The masking layers are removed and the process is complete.

5. The back side of the wafer is wet etched to release the cantilever. An etch stopping dopant is often used so the cantilever is not etched away.

6. The masking layers are removed, leaving a released mechanical structure.

This process is shown in Figure 3.3. Depending of the material properties and dimensions of the devices other steps or consideration may be required.

3.2.3 Surface Machining

Similar to the bulk machining process, surface machining uses materials and substrates common to the microelectronics industry. However, instead of using the entire substrate to create the mechanical devices, thin films deposited on the substrate are rather used [78]. This allows for very thin devices, out of a variety materials. Common materials include silicon nitride, polycrystalline silicon [78] and various metal alloys [81].

A surface machining process only requires starting with a flat enough surface to perform optical lithography, while maintaining an adequate thin film adhesion. Silicon substrates are conventionally used [78]. One typical process can be summarized as:

1. A sacrificial layer is deposited or grown on the substrate.

2. The sacrificial layer is patterned.

3. A thin film of the structural material (typically poly-crystalline silicon) is deposited.

4. The film is patterned to define the mechanical structure.

5. The sacrificial layer is removed, releasing the free standing structure.

This process is summarized in Figure 3.4.

3.3 Deflection Mode Cantilever Sensors

Deflection mode microcantilever sensors rely on the presence of a differential surface stress. The effects of surface stress generally are becoming more important in thin film science [31], MEMS [35] and biosensors [75]. A surface stress, σ_{ss}, can be formally defined using the Shuttleworth equation as [82]:

$$\sigma_{ss} = \gamma + \frac{\delta\gamma}{\delta\varepsilon}, \tag{3.1}$$

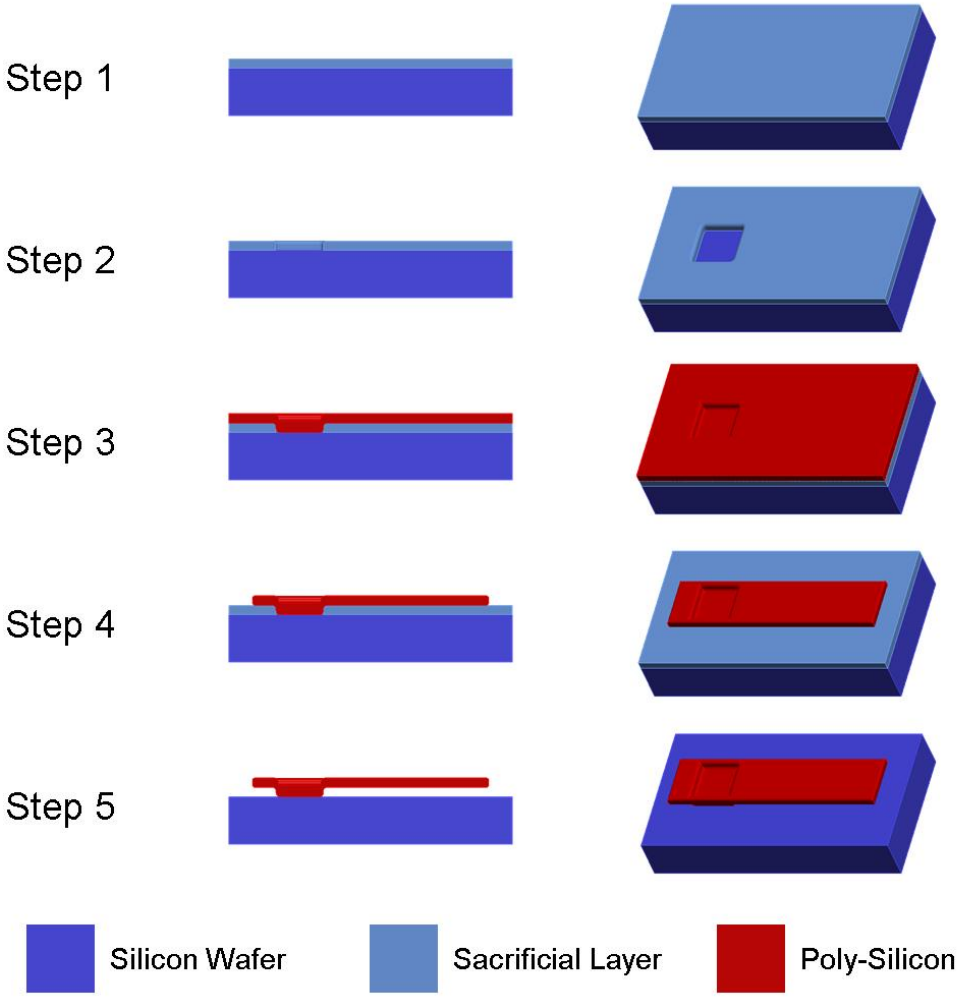

Figure 3.4: A typical surface machining process. Step 1: A sacrificial layer is deposited/grown on the substrate. Step 2: The sacrificial layer is patterned to define an anchor point for the mechanical structure. Step 3: A mechanical layer is deposited. This is typically polycrystalline silicon. Step 4: The mechanical layer is patterned to define the structure. Step 5: The sacrificial layer is removed and the structure is released.

where γ is the surface energy and ε is the elastic strain. For liquids the second term vanishes and the surface stress (in this case, also called surface tension) is equal to the surface energy. This is not the case in solids, since they can resist plastic deformation [82].

A positive surface stress is conventionally called tensile and will bend a thin plate towards the surface. A negative surface stress is called compressive and will bend a plate away from the surface [31]. Figure 3.5 depicts this difference.

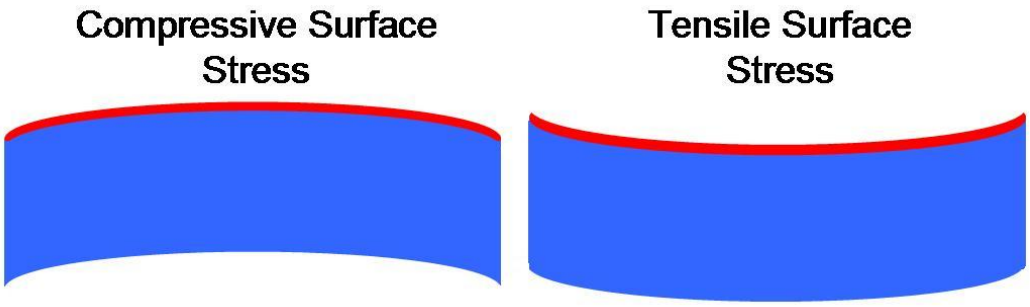

Figure 3.5: Depending on the type of stress upwards (tensile) or downwards bending (compressive) can result.

A a surface stress is often induced on the surface during the adsorption process. This can be expected at the fundamental level as the adsorbate will cause a change in the surface energy [82]. The origin of this change depends on the specific situation can be complex in nature and not always fully understood.

Deflection mode cantilever sensors rely on the fact that when there is a differential stress between the top and bottom sides of a cantilever, the cantilever will bend. This is due to the net moment caused by the surface stress' distance from the neutral axis [75,76,82]. Optical lever cantilever deflection systems have been shown to be sensitive enough to even measure single nanometers of deflection [83]. Alternatively, piezoresistive cantilevers have been used to avoid bulky optics and tedious optical alignment [84]. As such, microcantilevers have been demonstrated to be sensitive to very small changes in stress.

The bending of a cantilever due to a differential surface stress can be approximated by Stoney's equation [75, 82]:

$$\delta(x) = \frac{3\sigma_{ss}(1-\nu)}{E}\left(\frac{x}{t}\right)^2, \tag{3.2}$$

where σ_{ss} is the differential surface stress, E is Young's modulus, ν is Poisson's ratio, t is the cantilever thickness and x is the distance along the cantilever measured from the

base. Equation 3.2 predicts the largest deflection at the cantilever tip. The deflection can be measured in situ during the adsorption process as seen in Figure 3.6

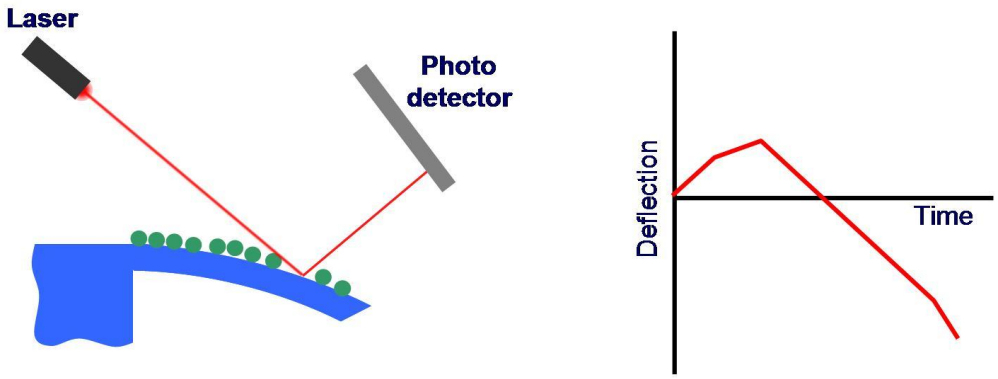

Figure 3.6: As molecules bind to one side of a cantilever, they cause a differential surface stress. This causes the cantilever to bend and can be recorded in realtime at the nanometer level.

Deflection mode cantilever sensors require that one side of the cantilever is essentially blocked. This often is achieved by coating one of the sides of a silicon cantilever with gold. A biosensor probe can then be immobilized specifically on the gold. When the analyte is captured it will preferentially bind to one side of the device, causing a change in the differential surface stress. To prevent non-specific binding to the silicon, it can be specifically blocked with a silane based blocking layer.

The sensitivity of these devices is related to the stiffness of the cantilever. Long, thinner cantilevers have higher sensitivities. Choosing materials with a lower Young's modulus also can amplify the bending due to surface stress. These materials must be compatible with microfabrication processes. Alternatively, several groups have proposed the use of SU-8 cantilevers due to their reduced stiffness [84–86].

A major advantage of deflection mode microcantilever sensors is that they are easily operated in fluids without compromising their sensitivity. For instance, Backmann *et al.* were able to detect 15 nM of analyte using antibody fragments immobilized on gold coated silicon cantilevers [87]. This resulted in about 50 nm of deflection. A deflection of 150 nm was noticed for a concentration of 300 nM.

3.4 Resonant Mode Cantilevers

3.4.1 Mechanical Vibration

One Degree of Freedom Simple Harmonic

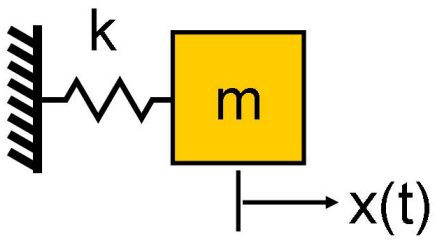

Figure 3.7: A single degree of freedom system.

Any mechanical system can be considered susceptible to external vibrations. The most basic mechanical system can be thought of as a mass attached to a spring as seen in Figure 3.7. With no external excitation, the equation of motion can be determined from Newton's laws for a mass of mass m and spring with a spring constant of k to be:

$$m\ddot{x} + kx = 0. \tag{3.3}$$

The general solution of Equation 3.3 is:

$$x(t) = A\cos(2\pi f_n t) + B\sin(2\pi f_n t), \tag{3.4}$$

where A and B are constants that are determined by the initial conditions. f_n is the natural frequency and is given by:

$$f_n = \frac{1}{2\pi}\sqrt{\frac{k}{m}}. \tag{3.5}$$

The natural frequency of the system is the frequency at which the system will vibrate under no external excitation. If an external oscillating force or base excitation is applied, a maximum vibration amplitude will occur when it is applied at the natural frequency.

Effective Mass and Stiffness

Multi-component mechanical systems can also be mathematically described in a similar fashion if all the velocities can be geometrically related as seen in Figure 3.8. However, the equation takes a modified form:

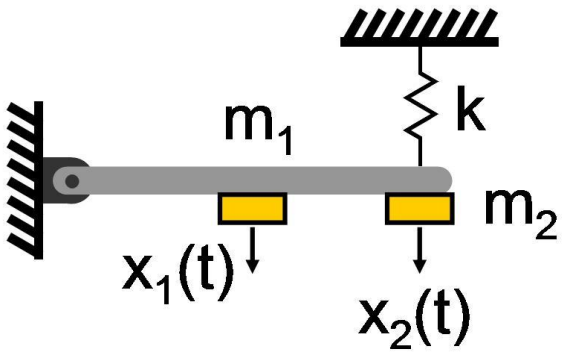

Figure 3.8: Even though there are several masses and springs, the system above has only one degree of freedom. By writing the velocities of m_1 and m_2 in terms of one reference point, the effective mass and stiffness of this system can be determined.

$$m_{eff}\ddot{x} + k_{eff}x = 0, \tag{3.6}$$

where m_{eff} and k_{eff} are the effective mass and stiffness of the system. To determine the effective mass and stiffness, an energy approach is often taken. First a reference point for the system is arbitrarily chosen. The equations of motion will be then be applied at this point. To determine the effective mass, the total maximum kinetic energy must be calculated. This value is then related to the maximum kinetic energy of a point mass at the reference point as follows:

$$E_k = \frac{1}{2}m_{eff}v_r^2, \tag{3.7}$$

where E_k is the maximum kinetic energy and v_r is the velocity of the reference point. Equation 3.7 allows for direct calculation of the effective mass. Similarly, by equating the elastic potential energy to that of the energy of a simple spring, k_{eff} can be determined:

$$E_p = \frac{1}{2}k_{eff}x_r^2, \tag{3.8}$$

where E_p is the potential energy and x_r is the displacement of the reference point. While this method is effective for relatively complex systems, both k_{eff} and m_{eff} can be used in Equation 3.5 to determine the natural frequency.

Multiple Degrees of Freedom

For more complex systems, like in Figure 3.9, more degrees of freedom may be required. By writing out Newton's laws, a system of coupled ordinary differential equations can be determined. As such, Equation 3.6 becomes:

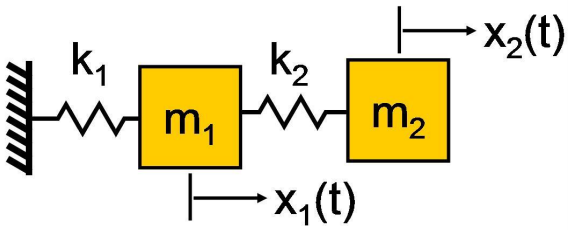

Figure 3.9: When velocities of a system cannot be related, several points must be used. This results in a coupled system of ordinary differential equations.

$$[M_{eff}]\ddot{\vec{x}} + [K_{eff}]\vec{x} = 0, \tag{3.9}$$

where $\vec{x}$ is a vector of the reference positions and $[M_{eff}]$ and $[K_{eff}]$ are the effective mass and stiffness matrices, respectively. For every n degrees of freedom a system has, there also exist n different modes of vibration. Each mode corresponds to a movement trajectory and a natural frequency. This is a consequence of each degree of freedom adding another solution to Equation 3.9. Formally, the natural frequencies are the eigenvalues and the mode shapes are the eigenvectors of the system. As such, for each degree of freedom there is a corresponding eigenvector and eigenvalue.

Viscous Damping

Only motion without the loss of energy has been discussed so far. However, this is almost never the case, as there is always some loss of energy. In mechanical systems energy dispassion is typically due to viscous damping. Viscous damping can be formulated as a force opposing the momentum vector of a moving system. The most basic system can be represented by the following:

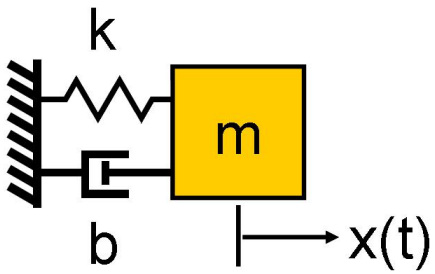

Figure 3.10: Real mechanical systems lose energy, often by means of viscous dampening. A viscous dampener is represent by the dashpot symbol.

$$m\ddot{x} + b\dot{x} + kx = 0, \tag{3.10}$$

where b is the viscous damping coefficient. As shown in Figure 3.10, this is often represented by a dashpot symbol. Viscous damping is a good model for the dissipation of energy due to damping effects of gases and liquids. The presence of damping will cause the vibrations to eventually stop. While this has many transient effect implications, the presence of damping will also affect natural frequency of the oscillator. The dampened natural frequency, also called the resonant frequency, is given by:

$$f_r = \frac{1}{2\pi}\sqrt{\frac{k_{eff}}{m_{eff}}}\sqrt{1-\zeta^2}, \tag{3.11}$$

where

$$\zeta = \frac{b}{2\sqrt{m_{eff}k_{eff}}}. \tag{3.12}$$

ζ is called the damping ratio. This value determines the transient effects of the motion. Equation 3.11 is only valid for values of ζ less than one. ζ will be much less than one in most situations and the difference between Equation 3.11, and Equation 3.5 is negligible. Without damping, the amplitude of vibration is theoretically unbounded. However, because all systems experience some damping, the resonant frequency is observed, which is bounded to a finite amplitude of motion. From Equation 3.11 it can be seen that the presence of damping will reduce the resonant frequency. The resonate frequency simplifies to the natural frequency in the absence of damping. Damping in air is often small enough to assume that resonant frequency is equal to the natural frequency.

A higher damping ratio increases the bandwidth in the frequency response of the system. This is often measured by the quality factor of the device. The quality factor can be expressed as:

$$Q = \frac{1}{2\zeta} = \frac{f_r}{f_{BW}}, \tag{3.13}$$

where f_{BW} is the one-half peak power bandwidth, as seen in Figure 3.11. The quality factor is an important figure of merit of a mechanical resonator. The ability to measure small shifts of the resonant frequencies will depend on the quality factor, which therefore proves important for cantilever sensing.

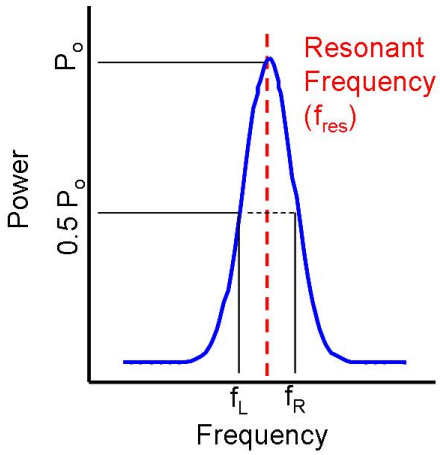

$$f_{BW} = f_R - f_L$$

$$Q = \frac{f_{res}}{f_{BW}}$$

Figure 3.11: The quality factor of a system can be determined from the frequency response. It requires measurement of the resonant frequency and the bandwidth.

3.4.2 Vibration Mechanics of Continuous Systems

The Euler-Bernoulli Equation

As the number of degrees of freedom in a mechanical system approaches infinity, it begins to behave like a continuum. That is the stiffness, inertial and damping properties are distributed throughout the structure. Partial differential equations as opposed to ordinary differential equations are therefore required to describe the motion. A consequence of the infinite degrees of freedom is that there are an infinite number of resonant frequencies and corresponding mode shapes.

This greatly complicates the problem in terms of its mathematics. However, one of the simplest mechanical structures to analyze is a simple beam. From Figure 3.12 the Euler-Bernoulli Equation can be formulated as [88]:

$$\frac{\delta^2}{\delta x^2}\left(EI\frac{\delta^2 y}{\delta x}\right) + \rho AL\frac{\delta^2 y}{\delta t^2} = 0, \tag{3.14}$$

where y is the vertical position of the beam, x is the coordinate along the beam, I is the second area moment of inertia and A is the cross-sectional area. The Euler-Bernoulli equation assumes that only small deflections are present and that deformation due to shear forces are negligible. This means Equation 3.14 is only valid for beams with large length-to-thickness ratios.

Equation 3.14 is a fourth order, linear, homogenous partial differential equation. It can be solved using the method of separation of variables [88]. A solution of the following form is assumed:

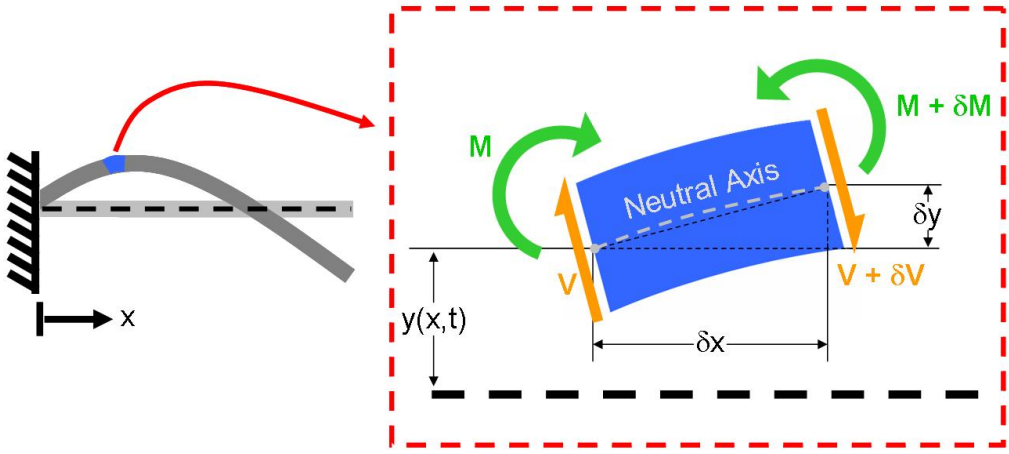

Figure 3.12: The Euler-Bernoulli equation can be derived by applying the equations of motion on a beam while taking into account the shear load (V) and the bending moment (M) loads. In the derivation of the Euler-Bernoulli equation the effects of shear deformation are neglected.

$$y(x,t) = X(x)T(t), \tag{3.15}$$

where y is the vertical deflection of the cantilever, and X and T are the spatial and time solutions to Equation 3.14, respectively. For a rectangular beam of uniform cross-section, the natural frequencies (f_n) of the system can be determined by the eigenvalues of the system:

$$f_n = \frac{t}{4\pi}\left(\frac{\lambda_n}{L}\right)^2\sqrt{\frac{E}{3\rho}}, \tag{3.16}$$

where L is the beam length and λ_n is called the mode number of the beam. The mode number can be determined from the boundary conditions. Each mode number corresponds to a different natural frequency and mode shape. There are theoretically an infinite number of these frequencies. Each mode of resonance has a higher frequency and smaller vibrational amplitude making them more difficult to measure. The mode shapes arise from the eigenfunctions of the time-independent solution to Equation 3.14:

$$X(x) = Acos(\lambda_n x) + Bsin(\lambda_n x) + Ccosh(\lambda_n x) + Dsinh(\lambda_n x), \tag{3.17}$$

where A, B, C and D are all constants determined by the boundary and initial conditions.

Cantilever Vibrations

The mode numbers and mode shapes can be determined for a given beam by applying the boundary equations. For cantilever structure, a beam with one fixed end (at x = 0) and one free end (at x = L) the boundary equations are [88]:

$$X(0) = 0 \tag{3.18}$$
$$\frac{\delta X}{\delta x}(0) = 0 \tag{3.19}$$
$$\frac{\delta^2 X}{\delta x^2}(L) = 0 \tag{3.20}$$
$$\frac{\delta^3 X}{\delta x^3}(L) = 0. \tag{3.21}$$

By applying these conditions to Equation 3.17 the mode numbers can be determined by the zeros to the following equation [88]:

$$cos(\lambda_n)cosh(\lambda_n) + 1 = 0. \tag{3.22}$$

Equation 3.22 has an infinite number of zeros and its first four are 1.875, 4.694, 7.855 and 10.996 respectively. The mode shapes can be subsequently determined as [88]:

$$X_n(x) = C_n \left(sin\left(\lambda_n \frac{x}{L}\right) - sinh\left(\lambda_n \frac{x}{L}\right) - \alpha_n \left[cos\left(\lambda_n \frac{x}{L}\right) - cosh\left(\lambda_n \frac{x}{L}\right) \right] \right), \tag{3.23}$$

where

$$\alpha_n = \left(\frac{sin(\lambda_n) + sinh(\lambda_n)}{cos(\lambda_n) + cosh(\lambda_n)} \right). \tag{3.24}$$

$X(x)$ is typically normalized so the maximum modal deflection is 1. Figure 3.13 shows the first three normalized mode shapes of a cantilever structure.

Effective Mass and Stiffness

Similar to discrete systems, the natural frequency of a cantilever beam can be expressed in terms of its mass and stiffness. The spring constant of the lateral bending of a constant rectangular cross-sectional cantilever:

$$k_{cant} = \frac{Ewt^3}{4L^3} \tag{3.25}$$

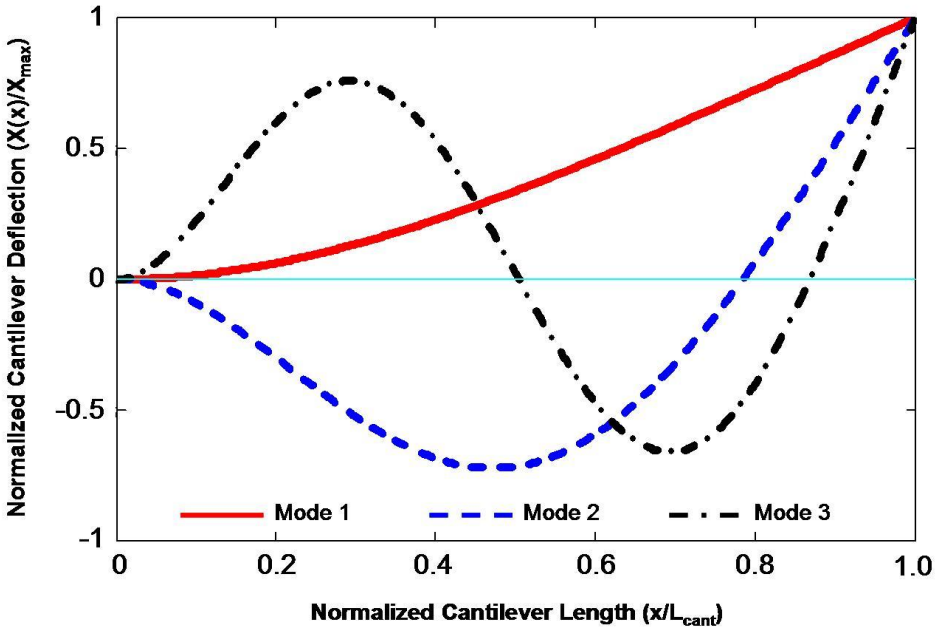

Figure 3.13: The first three mode shapes of a cantilever. Each mode shape is normalized by the deflection of the tip of that mode. However, in reality each mode has a decreasing amplitude that depends on the input excitation.

and the mass can be calculated as:

$$m_{cant} = \rho w t L. \tag{3.26}$$

Using these two properties, the natural frequency of a cantilever can be expressed as:

$$f_n = \frac{\lambda_n^2}{2\pi}\sqrt{\frac{k_{cant}}{m_{cant}}}. \tag{3.27}$$

Energy Methods

The governing equations are significantly more difficult to solve for more complex systems. The energy approach is generally the best way to predict the natural frequency of such a system. Assuming a harmonic time variance of the motion, the maximum kinetic energy can be expressed as [88]:

$$E_{k,max} = 2\pi^2 f_n^2 \int_0^L \rho A(x) X(x)^2 dx. \tag{3.28}$$

The maximum elastic potential energy stored in the beam can similarly be expressed as [88]:

$$E_{p,max} = \frac{1}{2}\int_0^L \left(EI(x)\frac{\delta^2 X(x)}{\delta x^2}\right)^2 dx. \tag{3.29}$$

This is a conservative system if damping is neglected. This means the maximum kinetic energy will equal the maximum potential energy. By applying this condition, the natural frequency is given by [88]:

$$f_n^2 = \frac{1}{4\pi^2}\frac{\int_0^L \left(EI(x)\frac{\delta^2 X(x)}{\delta x^2}\right)^2 dx}{\int_0^L \rho A(x)X(x)^2 dx}. \tag{3.30}$$

Equation 3.30 is called Rayleigh's quotient and is particularly useful in the analysis of stepped and other non-constant cross-sectional beams [17]. X(x) is typically not known for more complicated beams and loading conditions. In these cases, Rayleigh's quotient can be used to find an approximation of the natural frequency of the system. The static bending shape is assumed to predict the fundamental mode. Any arbitrary function can be used as long as it obeys the boundary conditions that constrain X(x). Because this over estimates the potential energy, Rayleigh's quotient causes an over prediction of the natural frequency [88].

The Rayleigh-Ritz method further expands this idea by introducing several different basis functions for X(x). This provides two major improvements over using just one mode shape. The first advantage is it provides a much better approximation of the natural frequency. Secondly, for each additional mode shape assumed, an additional mode of resonance is predicted [88].

3.4.3 Beams as Mass Sensors

Detection Principles

The operating principles of resonant mechanical sensors relies on the mass dependance of their resonant frequency. A small change in mass will result in a shift of the resonant frequency. This can be readily seen by taking a first order Taylor approximation of Equation 3.6 [75]:

$$\Delta f_n = \frac{-f_n}{2m_{eff}}\Delta m_{eff}. \tag{3.31}$$

Equation 3.31 is valid for small changes in the mass of a cantilever without any changes in the stiffness. Solving Equation 3.31 for the change in mass yields:

$$\Delta m_{eff} = \frac{-2m_{eff}}{f_n}\Delta f_n. \tag{3.32}$$

Equation 3.32 shows that for detecting small changes in mass a cantilever with a low effective mass and a high resonant frequency is required.

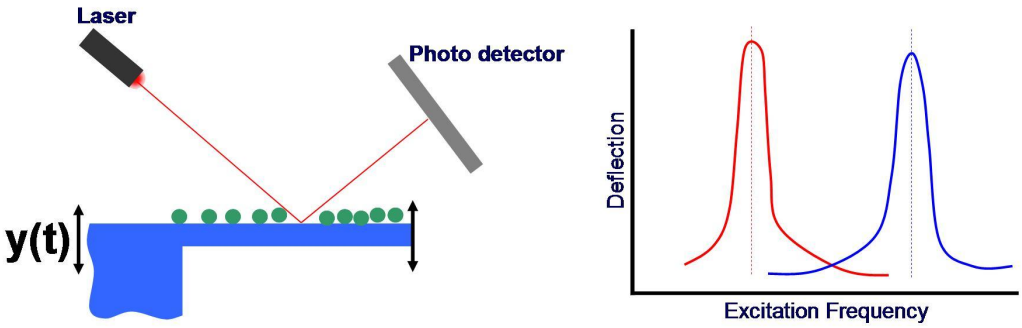

Figure 3.14: When the mass of a cantilever increases, the resonant frequency decreases. This property is exploited by microcantilever mass sensors.

Very small masses have been detected by using micro/nano cantilevers experimentally. Ilic *et al.* was able to detect attograms of added mass to cantilevers [89]. They used the specificity of thiol molecules to bind to gold that was patterned to be only at the tip of the cantilever. Yang *et al.* demonstrated cantilever mass sensing at the zeptogram level [90]. Fisher *et al.* detected the protein streptavidin using nanoscale doubly clamped beam resonators that were functionalized with biotin [91].

Sensitivity and Limits of Detection

There are several different factors that affect the minimum detectable mass of a cantilever sensor. Both relative and absolute sensitivities are often cited in the literature. The absolute sensitivity can be expressed as [92]:

$$\Delta S_{abs} = \frac{f_n}{2m_{eff}}. \tag{3.33}$$

It can be seen from Equation 3.33 that by increasing the resonant frequency and decreasing the mass of the system will cause a greater frequency shift for a given mass loading. The relative sensitivity is given by [93]:

$$\Delta S_{rel} = \frac{1}{2m_{eff}}. \tag{3.34}$$

Equation 3.34 shows the percent frequency shift only depends on the effective mass of the cantilever. Because microcantilever sensors often adsorb mass uniformly, the sensitivity per unit area for a single side cantilever sensor can be expressed by [93]:

$$\Delta S_A = \frac{1}{2\rho t}. \tag{3.35}$$

Equation 3.35 shows that relative frequency shift per unit area is only affected by the thickness and density of the cantilever.

Another important figure of merit of a cantilever sensor is the minimum detectable mass. Naturally, this depends on the quality factor of the device. A first order approximation of the minimum detectable mass, Δm_{min} is given by [77]:

$$\Delta m_{min} \propto \frac{m_{eff}}{Q}. \tag{3.36}$$

As illustrated by Equation 3.36, for smaller effective cantilever masses and large quality factors, smaller minimum detectable masses are obtainable. Several different factors can have a dominant effect on the quality factor in different situations. Viscous damping is by far the dominant factor affecting the quality factor in liquid environments. In addition, inertia loading caused by the weight of the fluid can also drastically lower the resonant frequency. This will ultimately limit the device sensitivity and the minimum detectable mass. Several groups have proposed both analytical [94–96] and computational models [97–99] of cantilevers vibrating in liquids. Campbell *et al.* has explored large cantilever sensors in fluids so inertial effects of the cantilevers will dominate that of the liquid damping effects with much success [100].

In air or devices open to atmosphere, there are no noticeable additional inertial effects observed. Damping can still manifest itself, broadening the resonant peak and thus reducing the quality factor. This was studied in detail by Xia *et al.* using a theoretical and computational approach [101]. In addition, surface machined devices may be susceptible to squeeze film damping, which can further lower the quality factor [35]. An undercut on a cantilever can further reduce the quality factor. This can be attributed to the additional effective length associated with the undercut that that lowers the frequency. Furthermore, undercut will also vibrate which will typically increase the viscose damping observed. [91]. This ultimately will limit the minimum detectable mass.

Much less damping is observed under vacuum, resulting in very high quality factors. Quality factors of over one million have been observed experimentally [102]. There are several factors that contributed to the damping in this system. One major factor is losses

at the clamping point. Energy can be also lost to the base of the device because it is impossible to create a perfect clamping point [77]. In addition, intrinsic damping in the structural material itself can cause an increase in damping. Henry *et al.* even showed various different surface terminations can affect the intrinsic damping of a system [103]. The ultimate limiting factor is thermomechanical noise present in any system. This can be limited by cooling the device to very low temperatures [104].

Another observation is that the mass sensitivity of a resonant mode cantilever sensor can be increased by resonanting the device at higher modes [105]. This can be seen as it provides a higher frequency of oscillation for use in Equation 3.33. Furthermore, by resonanting a cantilever at higher modes will increase the quality factor of the resonators. This allows for more sensitive microcantilever sensors with lower minimum detectable masses.

Stress Effects

Stress can also play a significant role in the vibration properties of beams. This can be seen readily with the vibrations of a taut string. A string can be thought of as a structure that cannot support a moment. The vibrations of a string are only possible when the string is under tension. These vibrations can be modeled very well by the one dimensional wave equation. From this solution, the natural frequency of the string depends only on the tension in the string, its mass per unit length and its length. The natural frequency of a taut string is given by [88]:

$$f_s = \frac{n}{2\pi L}\sqrt{\frac{T_s}{\mu}} \tag{3.37}$$

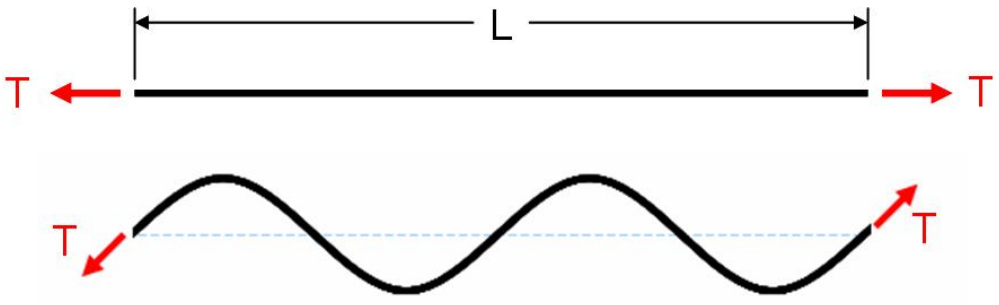

Figure 3.15: A vibrating string's natural frequency only depends on the length, the mass and the tension in the string. The fourth mode of resonance is shown.

Where T is the tension in the string, μ is the mass per unit length and n is the mode number (n = 1,2,3...). Doubly clamped beams also can exhibit similar behavior. Both tensile and compressive stress will affect the resonant behavior. In addition, if enough stress is present this effect will be dominant. The natural frequency will then have a L^{-1} (like a string) dependance instead of a L^{-2} (like a beam) [91]. Furthermore, additional tension not only increases the resonant frequency, but also the quality factor. For example, Verbridge *et al.* applied external tension to a nanostring and was able to increase both the natural frequency and the quality factor [106]. A compressive force in the beam is also known to decrease the natural frequency. Fischer *et al.* also demonstrated the use of residual stress within a structure as a way to tune nanomechanical resonators [91]. However, too much compressive stress can cause the beam to buckle [35].

Surface stress has also been shown to affect microcantilever structures. A surface stress has been typically modeled as an axial load or a distributed axial load [107–113]. Mcfarland *et al.* developed a stress sensor out of a resonant cantilever, which proved comparable in sensitivity to deflection mode stress sensing [110]. This was accomplished by the adsorption of thiol molecules to a gold coated microcantilever sensor. This resulted in an upward shift in the resonant frequency, which corresponds to a compressive surface stress. These results show that neglecting changes in stiffness during adsorption may not be always justified. However, the validity of these assumptions was also questioned by Lachut *et al.*, as they formed a more rigorous analytical analysis, outside the realm of beam theory [114].

Furthermore, since adsorption of molecules on the surface will affect both mass and surface stress, it is important to be able to de-couple these two effects.

3.5 Bacteria Detection Using Microcantilevers

3.5.1 Deflection Mode Microcantilever Bacteria Sensors

Deflection mode microcantilever sensors have been applied to the detection of pathogenic bacteria with limited success. Dhayal *et al.* detected *Bacillus anthracis* spores using peptide functionalized cantilever arrays. Gold coated cantilevers were functionalized with a peptide and all detection was performed on a Digital Instruments Scentris system. Bacteria were detected in both resonant and deflection mode cantilever sensing. The maximum deflection mode signal was 40 nm for a high concentration of spores. Resonant mode detection also resulted in small signals ($<$ 1 kHz) using the 5th mode of resonance [115]. Typical deflection mode studies see deflections on hundreds or thousands of nanometers.

Weeks *et al.* detected *Salmonella enterica* bacteria strain using silicon nitride deflection mode microcantilevers. Commercially available gold coated cantilevers were functionalized with antibodies and strain specificity was demonstrated. However, deflection signals were on the order of about 50 nm. Furthermore, the data has significant variance in experimental repeatability [116].

3.5.2 Resonant Mode Cantilever Bacteria Sensors

Resonant mode detection of bacteria has shown very promising results in several fundamentally different systems. Ilic *et al.* were able to detect a single bacteria on a small microfabricated cantilever [117]. Furthermore, they expanded the system to correlate the signal to the number of bacteria on the cantilever [118]. In both cases cantilevers of varying dimensions were employed. These microcantilevers were designed to be resonated in a typical AFM system.

Gupta *et al.* demonstrated bacteria detection using antibody functionalized surface machined cantilevers [119]. The microcantilever's resonant frequencies were measured on a Dimension 3100 AFM before and after bacterial capture. Very small frequency shifts were observed and correlated to the number of bacteria on the device. However, due to issues with stiction, the devices had to be critically dried to make the measurements.

Campbell *et al.* designed cantilevers to overcome viscous damping effects in liquids [100]. These cantilevers were on the order of millimeters in dimensions. They demonstrated that frequency and quality factor in liquids was very similar to that of air. Furthermore, they used these cantilevers to detect concentrations as low as 700 cfu/mL of *E. coli* O157:H7. Campbell *et al.* also detected 300 cfu/mL of *Bacillus anthracis* using similar methods [120]. Furthermore, by using EDC/NHS to immobilize the antibody layer detection levels were reduced to 10 cfu/mL in buffer [121]. Campbell *et al.* also detected *Bacillus anthracis* spores in air with a lower detection limit of 5 spores/L [122].

Ramos *et al.* also studied the effect of bacteria adsorption on the resonant properties of microcantilevers [123]. They placed drops of bacteria solutions on various parts of the cantilevers and studied the relative frequency shift. They reported that bacteria near the clamping point caused an upward shifts due to the elastic stiffness of the bacteria, while bacteria at tip caused downward shifts corresponding to mass loading. They also further developed this by examining the results in higher modes using perturbation theory, finite element analysis and experimental data [124]. The cantilevers were not functionalized with a probe and bacteria were placed in drops, which formed large clumps. This is often not the case with biosensor devices.

However, there has been little investigation into the development of a phage based microcantilever bacterial sensor. This poises as a great opportunity to exploit the sensitivity of microcantilever sensors with the selectivity of the phage. Doing so would represent a step towards a commercialization bacteria biosensor.

3.6 Summary

This chapter explored the mechanics involved in both resonant and deflection based microcantilever detection. The typical fabrication methods for creating a microcantilever sensor were reviewed. The surface stress detection ability of deflection mode microcantilever sensors was then outlined. Resonant cantilever sensors were developed in the context of vibrational theory as mass sensors. Finally, several case of microcantilever based bacteria detection have been reviewed.

4

Advancing Resonant Microcantilever Sensors: Decoupling Stress and Mass

4.1 Overview

This chapter examines the effect of small surface stresses on the resonant frequencies of microcantilevers at various modes. While the effect in higher modes of resonance is well defined in terms of mass loading, this is not the case with stress. This analysis is important in order to allow an accurate interpretation of the resonance data with respect to mass loading of the device. Theoretical, finite element, and experimental approaches are all carried out for verification. Ultimately, a novel method for decoupling the frequency shifts due to small changes in surface stress and mass as Part of this work. This approach is based on the mode number dependance of the relative frequency shift due to stress.

4.2 Theory

4.2.1 Cantilever Detection

As seen in Chapter 3, resonant microcantilever sensors measure a shift in resonant frequency in order to correlate it to a change in mass. However, induced surface stress from molecular adsorption can also cause shifts in the resonant frequency of a beam. The resonant frequency of an undamped mechanical systems is expressed as:

$$f_n = \frac{1}{2\pi}\sqrt{\frac{k_{eff}}{m_{eff}}}. \tag{4.1}$$

For small changes in k_{eff} and m_{eff}, the change in frequency is expressed as:

$$\frac{\Delta f_n}{f_n} = \frac{1}{2}\left(\frac{\Delta k_{eff}}{k_{eff}} - \frac{\Delta m_{eff}}{m_{eff}}\right). \tag{4.2}$$

The interpretation of k_{eff}, Δk_{eff}, m_{eff} and Δm_{eff} will be provided in the following sections.

4.2.2 Microcantilever Effective Mass and Stiffness

The definition of effective mass and stiffness of a cantilever beam has been extensively discussed in the literature [73, 76, 93, 125]. All of these definitions predict Equation 4.1 correctly. Equation 4.2 however requires precise definitions of the effective mass and stiffness.

It is most appropriate to take an energy approach to determine these terms. The effective mass can be determined by maximum kinetic energy of a cantilever at an arbitrary mode as compared to that of a simple mechanical system undergoing sinusoidal excitation. Naturally, the cantilever tip is taken as the reference point of the system. This means the maximum kinetic energy of the cantilever can be expressed as [88]:

$$E_{k,max} = \frac{1}{2}m_{eff}\dot{y}(L,t)^2_{max} = 2\pi^2 f_n^2 m_{eff} X(L)^2 = 2\pi^2 f_n^2 \int_0^L \rho A X(x)^2 dx. \tag{4.3}$$

By assuming the time independent solution to the Euler-Bernoulli (defined in Chapter 3), Equation 4.3 can be integrated. Solving for effective mass and integrating yields:

$$m_{eff} = \frac{1}{4}\rho A t = \frac{1}{4}m_{cant}. \tag{4.4}$$

The effective stiffness can be determined similarly from analyzing the maximum potential energy of the system and comparing it to a simple spring [88]:

$$E_{p,max} = \frac{1}{2}k_{eff}y(L,t)^2_{max} = \frac{1}{2}k_{eff}X(L)^2 = \frac{1}{2}\int_0^L EI\frac{dX(x)}{dx}^2 dx. \tag{4.5}$$

Equation 4.11 can be integrated by assuming the mode shapes predicted by the Euler-Bernoulli equation. Solving for the effective stiffness and integrating yields:

$$k_{eff} = \frac{1}{4}\lambda_n^4 \frac{EI}{L^3} = \frac{1}{12}\lambda_n^4 k_{cant}. \tag{4.6}$$

This analysis suggests that the effective stiffness increases with the mode of resonance and the effective mass remains constant. The higher frequencies associated with higher modes of resonance directly result from an increase in stiffness.

4.2.3 Changes in Effective Mass

Discrete Mass

The change in the maximum kinetic energy of a system with j discrete changes in masses of mass Δm_i will be:

$$\Delta E_{k,max} = 2\pi^2 f_n^2 \sum_{i=1}^{i=j} \Delta m_i X(x_i)^2, \tag{4.7}$$

where x_i is the location of the i^{th} mass. The change in effective mass Δm_d can then be determined as:

$$\Delta m_d = \sum_{i=1}^{i=j} \Delta m_i \left(\frac{X(x_i)}{X(L)}\right)^2. \tag{4.8}$$

A mass at the tip has its effective mass equal to the additional mass. This is a natural consequence of choosing the tip as reference point.

Uniformly Distributed Surface Mass

A similar analysis can be carried out to determine the change in the effective mass resulting from an added distributed surface mass. The change in the maximum kinetic energy resulting from an additional surface mass is given by:

$$\Delta E_{k,max} = 2\pi^2 f_n^2 \int_0^L \frac{d\Delta m}{dA_s}\frac{dA_s}{dx} X(x)^2 dx, \tag{4.9}$$

where A_s is the surface area of the cantilever that the mass is distributed over. For a uniformly distributed mass, this can be determined to cause a change in the effective mass of:

$$\Delta m_u = \frac{1}{4} m_s, \tag{4.10}$$

where m_s is the total added mass.

4.2.4 Changes in Effective Stiffness

Elastic Stiffening

For a cantilever that is stiffened elastically, such as from an additional thin film, the change in effective stiffness can be determined as follows:

$$\Delta k_E = \frac{1}{X(L)^2}\int_0^L E_s I_s \frac{dX(x)}{dx}^2 dx, \tag{4.11}$$

where E_s is Young's modulus and I_s is the moment of inertia of the added stiffening layer. For a very thin surface layer I_s can be approximated as $\frac{wt_s t^2}{4}$ where t_s is the thickness of it [35]. The change in the effective stiffness due to a uniformly distributed surface elastic stiffening layer can be determined from these definitions to be:

$$\Delta k_E = \frac{\lambda_n^4}{16} E_s w t_s t^2. \tag{4.12}$$

Effective Stiffening Due to Stress: A Novel Approach

The stress state can affect the resonant properties of a microcantilever. Here the surface stress will be approximated as an axial load. However, this requires the modification of the Euler-Bernoulli Equation as follows [88]:

$$\frac{\delta^2}{\delta x^2}\left(EI\frac{\delta^2 y}{\delta x}\right) + \rho AL\frac{\delta^2 y}{\delta t^2} + \frac{\delta}{\delta x}\left(P(x)\frac{\delta y}{\delta x}\right) = 0, \tag{4.13}$$

where $P(x)$ is the axial force in the beam. For a uniform surface stress, $P(x)$ is a constant. However, by solving the time independent part of Equation 4.13, the mode shape can be determined to be [88]:

$$X(x) = C_1 cosh\left(\Lambda_{1,n}\frac{x}{L}\right) + C_2 sinh\left(\Lambda_{1,n}\frac{x}{L}\right) + C_3 cos\left(\Lambda_{2,n}\frac{x}{L}\right) + C_4 sin\left(\Lambda_{2,n}\frac{x}{L}\right), \tag{4.14}$$

where $\Lambda_{1,n}$ and $\Lambda_{2,n}$ are the mode numbers of the system. The resonant frequency can then be expressed as [88]:

$$f_{P,n} = \frac{1}{2\pi L^2}\sqrt{\frac{EI}{\rho A}}\sqrt{\Lambda_{2,n}^4 + \Lambda_{2,n}^2\frac{PL^2}{EI}}. \tag{4.15}$$

For a constant cross sectional area cantilever loaded with tensile planar surface stress, the average force *in the beam* can be approximated as:

$$P = \frac{-\sigma_{ss} w}{1-\nu}. \tag{4.16}$$

By substituting Equation 4.16 into 4.15, taking derivative with respect to the surface stress and dividing by the natural frequency:

$$\frac{1}{f_{P,n}} \frac{\delta f_{P,n}}{\delta \sigma_{ss}} = -\frac{1}{8\pi^2 m_{eff}} \frac{\Lambda_{2,n}^2}{4(1-\nu)} \frac{w}{L} \frac{1}{f_{P,n}^2}. \tag{4.17}$$

This assumes that the mode number in the small region near $P = 0$ is relatively invariant. For a small change in surface stress Equation 4.17 can be simplified so that the relative frequency shift becomes:

$$\frac{\Delta f_{P,n}}{f_{P,n}} = -\frac{\Lambda_{2,n}^2}{8} \frac{w}{L} \frac{\Delta \sigma_{ss}}{1-\nu} \frac{1}{k_{eff}}. \tag{4.18}$$

From inspection of Equation 4.2, the change in stiffness due to the additional stress can be determined to be:

$$\Delta k_\sigma = -\frac{\Lambda_{2,n}^2}{4} \frac{w}{L} \frac{\Delta \sigma_{ss}}{1-\nu}. \tag{4.19}$$

$\Lambda_{2,n}$ depends on the boundary conditions and the value of P. However, since as $P \to 0$ implies $\Lambda_{2,n} \to \lambda_n$, so for $P << 1$, $\Lambda_{2,n} \approx \lambda_n$. The approximate change in stiffness due to a surface stress can be given by:

$$\Delta k_\sigma \approx -\frac{\lambda_n^2}{4} \frac{w}{L} \frac{\Delta \sigma_{ss}}{1-\nu} \tag{4.20}$$

An expression for the absolute stress sensitivity can from these results be expressed as:

$$\mid S_{abs,\sigma} \mid = \frac{\Delta f_n}{\Delta \sigma_{ss}} = \frac{3}{2\pi(1-\nu)\sqrt{E\rho}} \frac{1}{t^2}. \tag{4.21}$$

It can be noted that unlike the mass, the absolute sensitivity to surface stress does not change with higher modes.

4.2.5 Frequency Response Implications: A Novel Method for Decoupling Mass and Stress

Equation 4.2 can now be expanded as follows:

$$\frac{\Delta f_n}{f_n} = \frac{1}{2} \left(\frac{\Delta k_\sigma}{k_{eff}} + \frac{\Delta k_E}{k_{eff}} - \frac{\Delta m_{eff}}{m_{eff}} \right). \tag{4.22}$$

Substituting in the effective mass, effective stiffness, elastic stiffening, stress stiffening and a change in mass due to a distributed load mass yields:

$$\frac{\Delta f_n}{f_n} = \frac{1}{2}\left(-3\frac{w}{L}\frac{1}{\lambda_n^2}\frac{\Delta\sigma_{ss}}{1-\nu}\frac{1}{k_{cant}} + \frac{3E_s w t^2 t_s}{4k_{cant}} - \frac{\Delta m_s}{m_{cant}}\right). \tag{4.23}$$

An important consequence of Equation 4.23 is that the stress term actually decreases quadratically with the mode number. This can be exploited as a novel way to decouple mass and stress contributions to the relative frequency shift. As the mode of resonance increases the stress stiffening becomes less significant. For a cantilever with no elastic stiffening it then holds that:

$$lim_{n\to\infty}\frac{\Delta f_n}{f_n} = -\frac{1}{2}\frac{\Delta m_s}{m_{cant}} \tag{4.24}$$

Equation 4.24 means that when surface stress and mass contributions are both present on a cantilever, the stress contribution can be disregarded by resonating the cantilever in a high enough mode. Surface stress is typically disregarded anyways, however this may not be justified in the first mode of resonance where the stress term may dominate.

Another way these findings can be interpreted is that mass loading causes a constant change in the relative frequency shift, while stress loading causes a constant absolute frequency shift with respect to the mode of resonance.

4.3 Finite Element Analysis

4.3.1 Overview

The equations developed in section 4.2 reveal the nature of stress stiffening in a cantilever beam. Stress stiffening has been shown to approximately vary with the square of the mode number. Finite Element Analysis (FEA) is employed to verify this phenomenon and explore how accurate mass loading predictions can be made.

4.3.2 Cantilever Models

Microcantilevers

All FEA simulations were carried out in ANSYS 11.0. Four different cantilevers with various dimensions were modeled. Their dimensions were chosen based on the nominal values of commercially available tipless AFM cantilevers. These dimensions are shown in Table 4.1.

Table 4.1: Modeled Microcantilever Dimension

Cantilever	**Length**	**Width**	**Thickness**
-	μm	μm	μm
1	500	100	1
2	450	50	2
3	225	28	3
4	125	30	4

Cantilever 1 is based on Nano World Arrow-TL cantilevers [126] while cantilevers 2, 3 and 4 are based on Nanosensors cantilevers TL-CONT [127], TL-FM [128] and TL-NCH [129], respectively. All cantilever cross sections were taken to be rectangular for this model.

Material Model

Material properties for all cantilevers were taken to be that of single crystal silicon. An isotropic material model was used for silicon with Young's modulus and Poisson's ratio equal to 169GPa and 0.287, respectively. These material properties were obtained from the AFM microcantilever FEA model of Beltran *et al.* [130].

An isotropic model will lead to some level of error because silicon is an anisotropic material [35]. An isotropic model is justified because the changes in the resonant frequency relative to the original frequency are of most interest. Beltran *et al.* also used this simplification.

Element and Mesh properties

The element Solid45 (8 node, 3 dimensional structural solid)was used for the bulk of the cantilevers in each model [131]. Several different elements were compared for Cantilever 1, and Solid45 showed the fastest relative and absolute convergence. Solid45 also has stress stiffening capabilities, which is vital to this analysis. As a result this element was used in all subsequent analysis for bulk properties. The mesh was created with 8 node brick elements of equal size.

The surface element Surf154 was used to simulate surface effects like added mass loads [132]. The material properties for this element were chosen to be the same as silicon with its thickness was set to approximately zero (10^{-15}m). This caused the addition of the unloaded surface element to have negligible effects on the mechanical properties of the beam. Additional mass was added using the added mass property of Surf154.

Loading Conditions and Analysis

The unloaded cantilever was assumed to be perfectly clamped at one end. This means all of the degrees of freedom at that end of the cantilever were set to zero. This constraint was applied to all of the nodes at this end. A modal analysis was performed for the first 30 modes of each cantilever and their corresponding frequencies. Specifically of interest were the bending modes, so the first 8 bending modes were isolated from the set of 30 modes.

Mesh Sensitivity

A mesh sensitivity test was preformed for all cantilevers to ensure proper solution convergence. The relative error and absolute error were calculated for various mesh sizes. Here the relative error and absolute error for the ith of j mesh sizes is defined as:

$$\epsilon_{rel} = \frac{f_{n,i} - f_{n,i+1}}{f_{n,i+1}} \tag{4.25}$$

$$\epsilon_{abs} = \frac{f_{n,i} - f_{n,j}}{f_{n,j}} \tag{4.26}$$

respectively, where the jth mesh has the largest number of elements. Higher modes required smaller mesh sizes for comparable accuracy. Meshes were chosen so that the 30th mode of resonance's relative and absolute error was less than 0.5%. The convergence with respect to the number of elements for the 30th mode can be see in Figure 4.1.

Unloaded Microcantilever Resonant Properties

The natural frequency of each cantilever was non-dimensionalized in the following fashion:

$$F_n = f_n 4\pi \sqrt{\frac{3\rho L^4}{Et^2}} = \lambda_n^2, \tag{4.27}$$

where F_n is the non-dimensionalized frequency. This allowed for direct comparison of resonant properties of the microcantilevers. The first and second bending, torsional and plate mode shapes are shown for cantilever 4 in Figure 4.2.

In the first 30 modes cantilevers had bending, torsonal, plate and longitudinal modes of vibration. The bending modes of the cantilevers were then isolated, normalized and are summarized in Table 4.2.

One interesting observation is that the normalized frequency is slightly dependent on the geometry and deviates from the Euler-Bernoulli equation. This is likely due to the effect of shear deformation, which was neglected in the derivation of the Euler-Bernoulli equation.

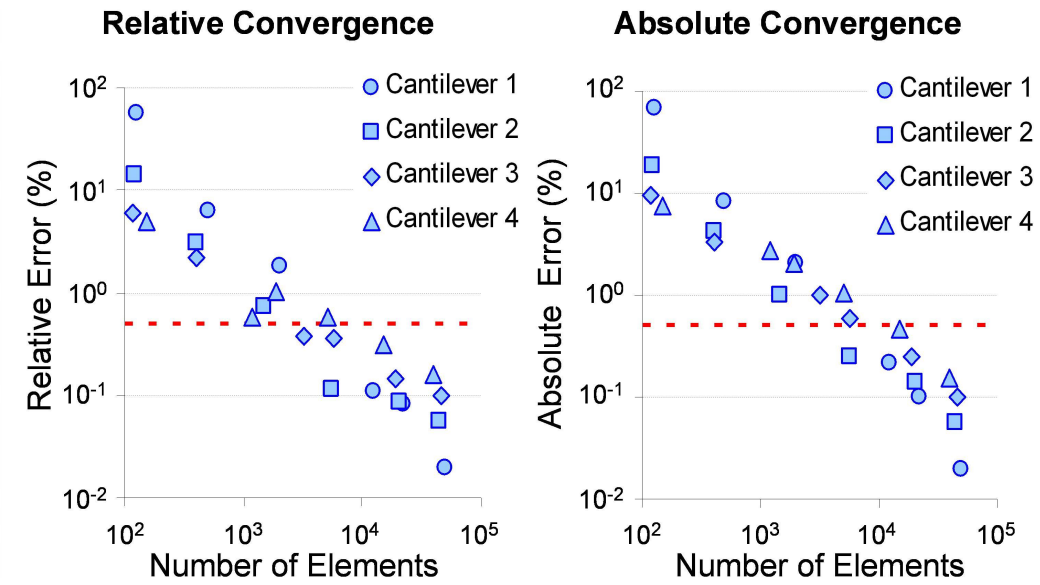

Figure 4.1: The relative and absolute convergence of the 30th mode of resonance for each different cantilever geometries. Meshes were chosen with the convergence criterion of both errors to be under 0.5%.

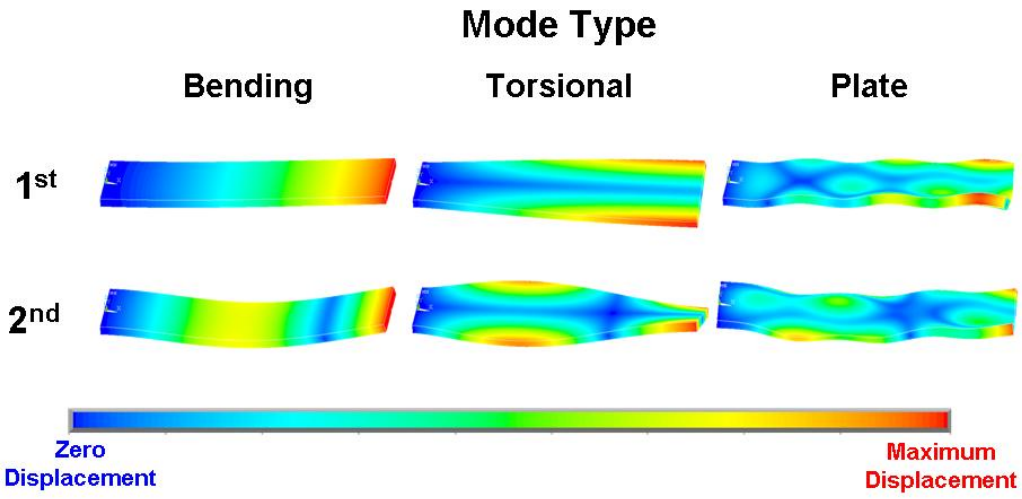

Figure 4.2: First 2 mode shapes of the bending, torsional and plate mode types.

Table 4.2: Non-dimensionalized Bending Modes

Mode	Euler-Bernoulli	Cant 1	Cant 2	Cant 3	Cant 4
1	3.52	3.56	3.54	3.54	3.55
2	22.0	22.3	22.2	22.2	22.2
3	61.7	62.4	62.1	62.0	61.7
4	121	123	122	122	120
5	200	203	202	201	196
6	299	305	302	300	289
7	417	426	423	418	399
8	555	565	564	556	521

Shear effects play a more dominant role as the thickness of the cantilever increases [88]. The bending mode shapes for the first few bending modes of resonance of these cantilevers can be seen in Figure 4.3.

4.3.3 Surface Mass

Surface mass of 1%, 2%, 3%, 4% or 5% of each cantilever's mass was added uniformly over their top surface. For each cantilever the percent frequency shift was invariant of the mode of resonance for added surface mass, which is consistent with Equation 4.2. Figure 4.4 shows the frequency shifts as function of mode frequency and mass per unit area absolute sensitivity of each cantilever.

4.3.4 Surface Stress Effects

Modeling Strategy

Both a static and modal analysis were performed in order to obtain the effect of surface stress stiffening on the cantilever structure. A two-dimensional surface stress was approximated by placing equivalent forces on the three free edges on the top surface. This was accomplished by applying a force normal to each node on the free edges. Only the top surface was loaded so that cantilever bending occurred due to a differential surface stress. This allowed for the deflection profile to also be predicted. These loading conditions are shown in Figure 4.5

The deflection and stress distributions were determined in the static analysis. To ensure consistency the static deflection was compared to that of Stoney's equation. A mesh sensitivity test was also evaluated at a high stress loading case. Deflection results agreed

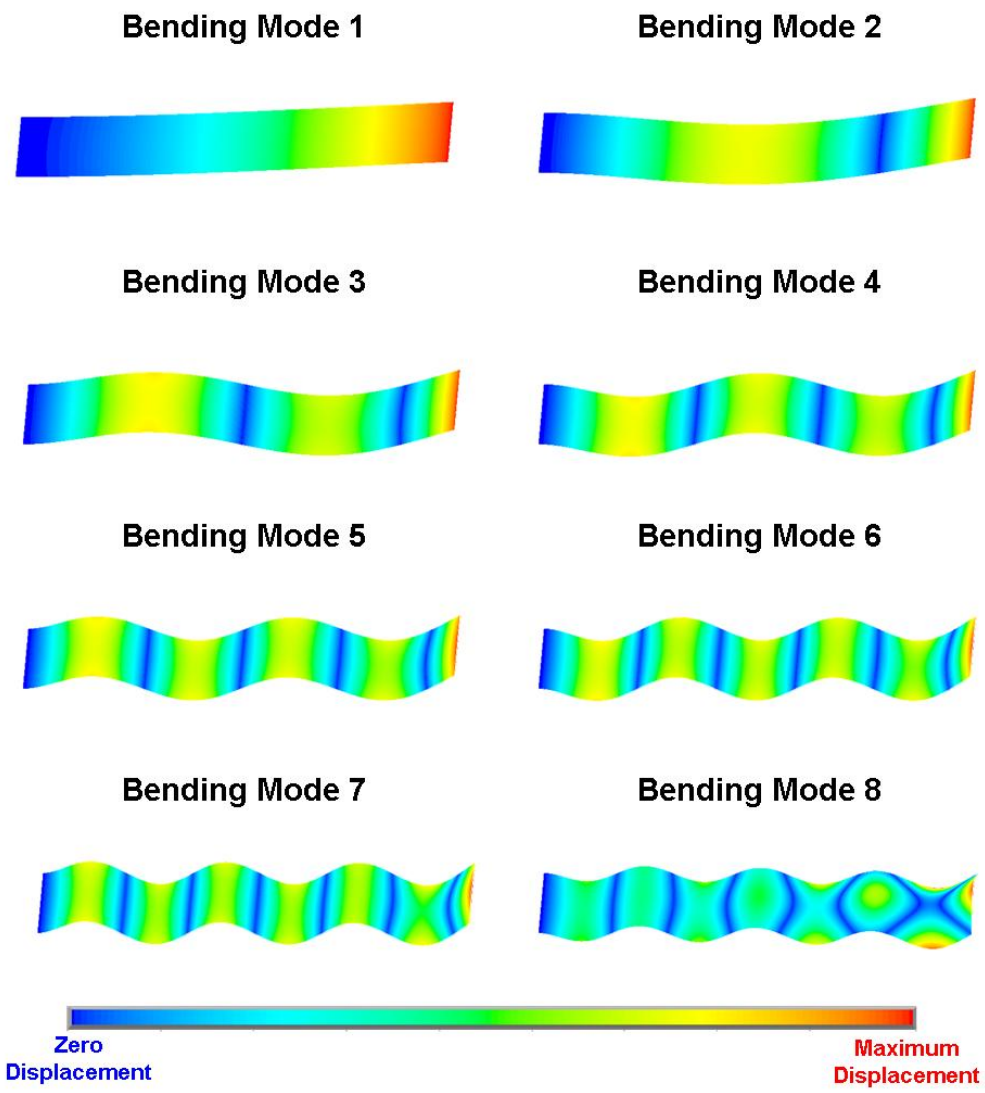

Figure 4.3: The first 8 bending mode shapes of cantilever 1. The eighth mode begins to deviate from the expected mode shape.

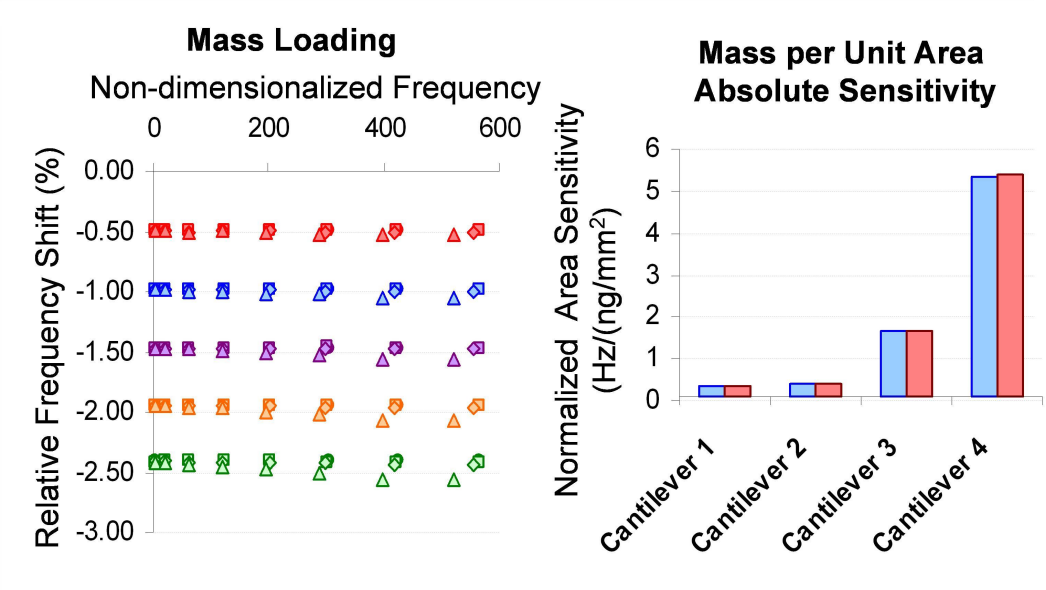

Figure 4.4: Left: The effect of percent added mass on the percent relative frequency shift. Mass loading: red = 1%, blue = 2%, purple = 3%, orange = 4%, green = 5%. Cantilever 1: ○, Cantilever 2: □, Cantilever 3: ◇, Cantilever 4: △. Right: Mass sensitivity per unit area of each cantilever normalized by mode number. Blue: ANSYS predicted mass sensitivity, Red: Theoretical mass sensitivity.

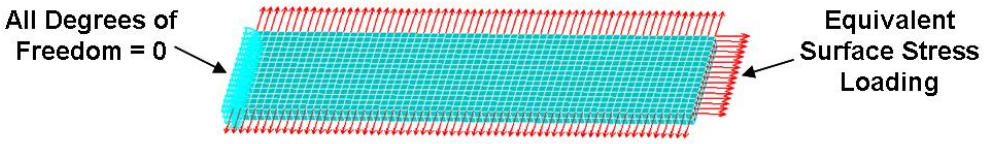

Figure 4.5: The applied loads and boundary conditions to simulate a cantilever with a surface stress on its top surface. A large mesh is shown so that individual elements and force vectors can be seen.

with Stoney's equation to within 5%. Absolute convergence of the stress and deflection was less than 1.5% and the convergence can be seen in Figure 4.6.

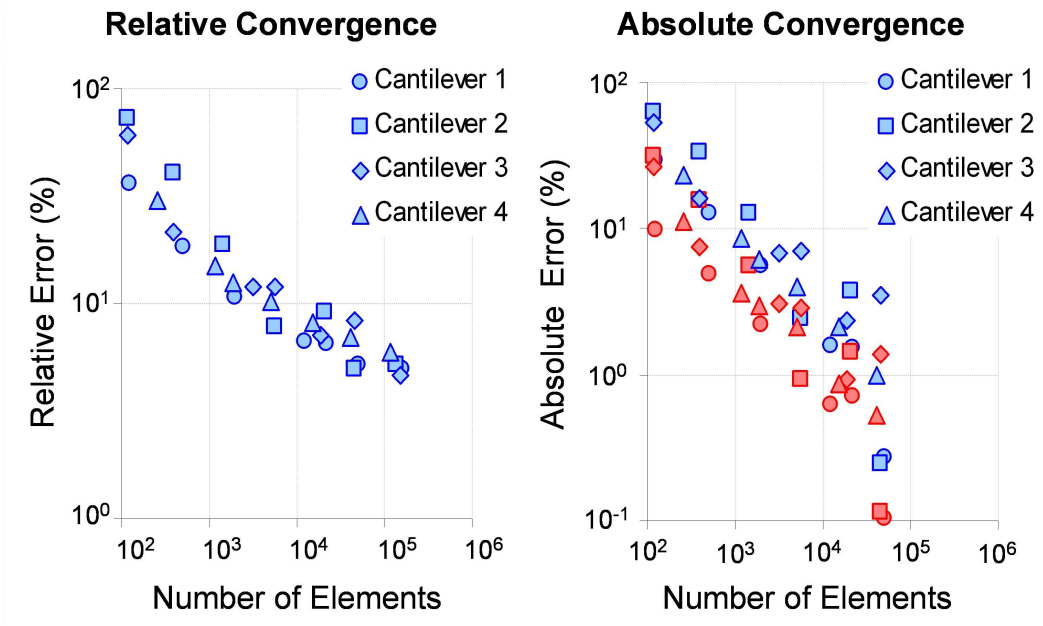

Figure 4.6: Left: The relative error of the model with respect to Stoney's equation. Right: The absolute convergence of the stress (red) and the tip deflection (blue). Mesh size was chosen so that the stress convergence was less than 1.5%

To determine the effect of the surface stress on the natural frequency, a static analysis was preformed followed by a modal analysis. The modal analysis was performed in the same fashion as the unloaded case, except a frontal solver was used. The surface stress was non-dimensionalized in order to compare the cantilevers of different dimensions as:

$$S_{ss} = \frac{w}{L}\frac{\Delta\sigma_{ss}}{k_{cant}}, \tag{4.28}$$

where S_{ss} is the non-dimensionalized surface.

Cantilever Deflection

Surface stress and deflection vs position plots were obtained after the static analysis was performed. Figure 4.7 shows an example of these plots. As expected the loading conditions created a uniform planar stress distribution that only varied through the thickness. This naturally resulted in a deflection profile similar to that of Stoney's equation.

Analysis was completed for the values of 0.6, 0.4 and 0.2 of the non-dimensionalized stress surface for both tensile and compressive stresses. The deflection at the tip was then

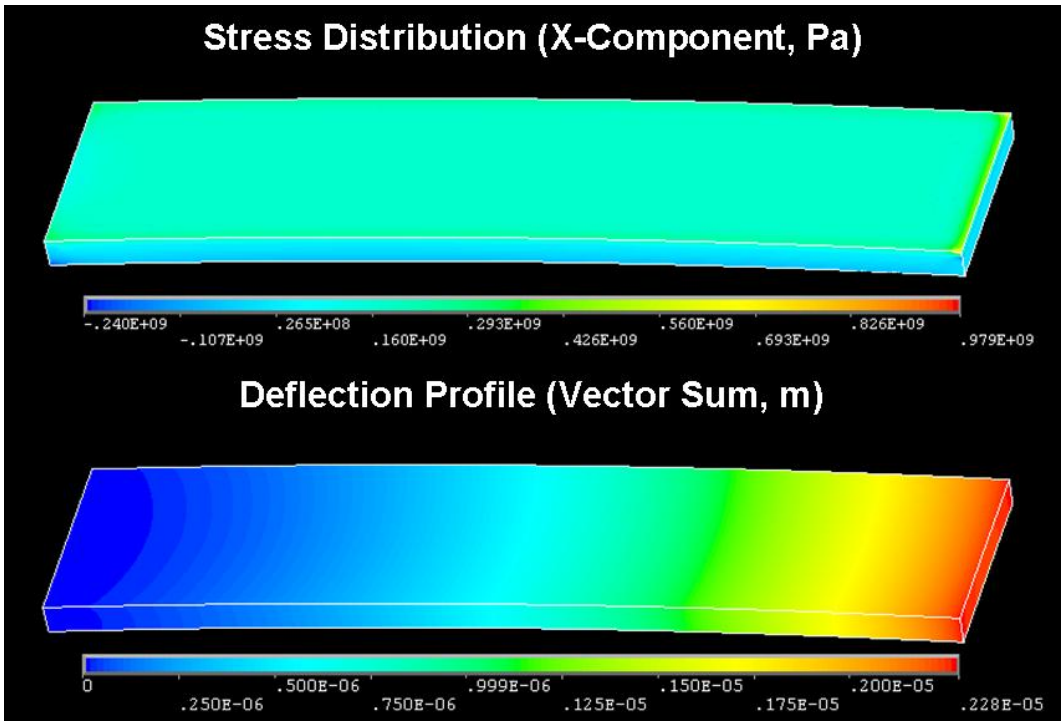

Figure 4.7: An example of the static ANSYS analysis results. Both the x-component stress distribution and the and the resulting vector sum displacement are shown. As expected the surface stress is fairly uniform across the cantilever, while the deflection shows the expected maximum deflection at the tip.

normalized by the thickness for each cantilever at each stress state. Simulations showed negligible variation between each cantilever's normalized deflection. Figure 4.8 shows these values as compared to Stoney's Equation. Simulations deviated less that 5% over the entire range of stress values.

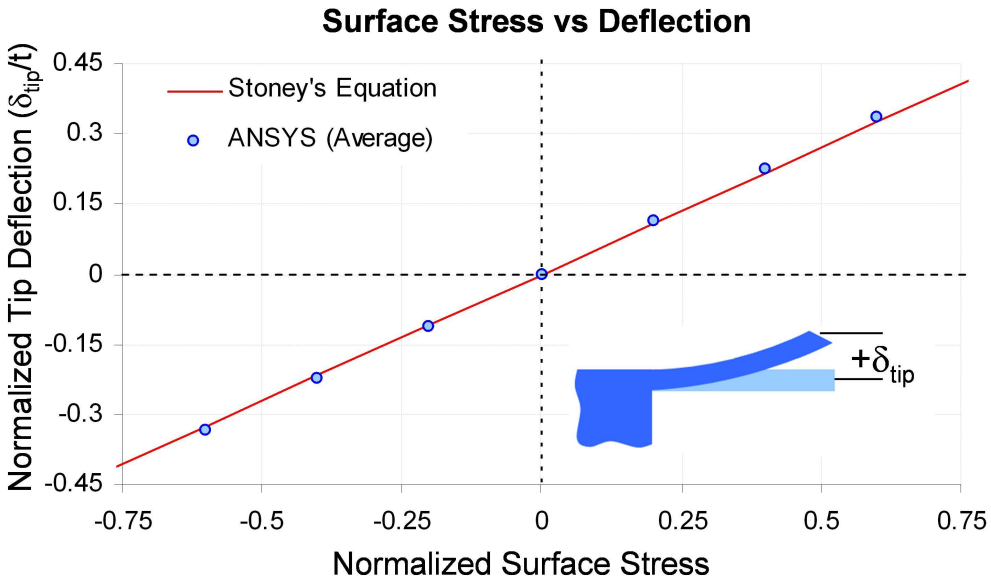

Figure 4.8: The applied surface stress verses the normalized tip deflection as predicted from ANSYS simulations. For comparison, Stoney's equation is shown. The results deviate approximately 5% from Stoney's equation.

Effect of Surface Stress on Resonance

The values of 0.4, 0.2, 0.1 and 0.01 of both compressive and tensile non-dimensionalized surface stresses used to determine its effect on the resonant frequency. The first 8 bending modes of resonance were isolated in each stress state for each cantilever. Most of the error in the surface stress induced-frequency shift is due to roundoff error, especially at higher modes and lower stress states. However, as with the tip deflection, non-dimensionalized values varied insignificantly between cantilever models.

Figure 4.9 shows the relative frequency shift versus the non-dimensionalized surface stress for the first mode of resonance. For larger values of surface stress, the simulations clearly deviate from the equations developed in Section 4.2. This is likely due to the breakdown of a small stress approximation. Furthermore, it can be seen that tensile surfaces cause downward frequency shifts, while compressive stress causes upwards shifts. While

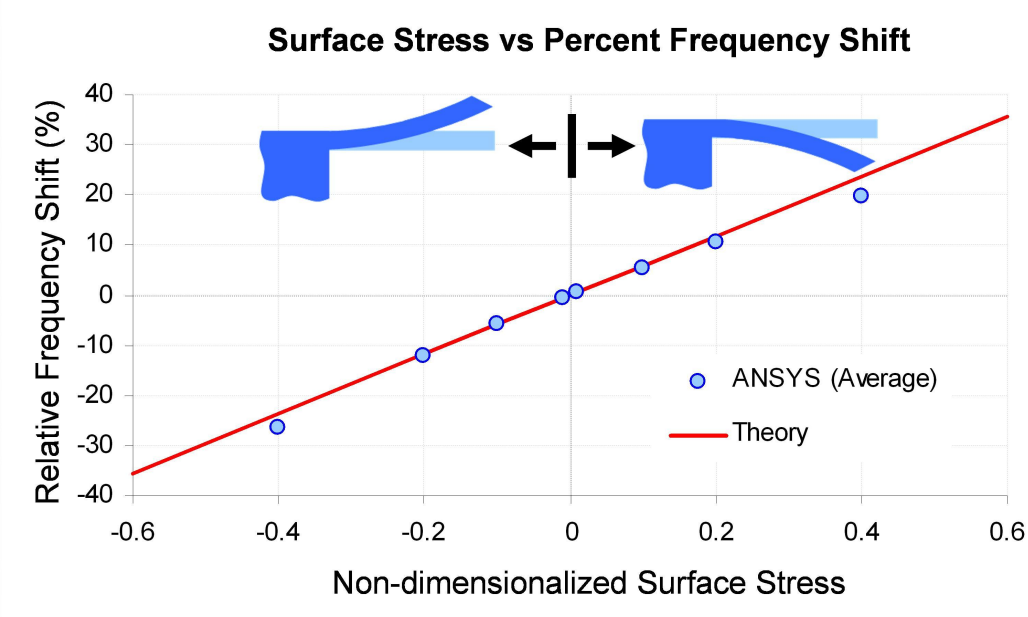

Figure 4.9: The relative frequency shift with respect to the applied non-dimensionalized surface stress for the first mode of resonance. ANSYS points for each canilever were averaged. The predicted theory is shown for comparison.

this may seem counterintuitive, a tensile surface stress will cause a compressive stress in the beam to maintain equilibrium.

The relative frequency shift due to stress is expected to drop off for higher modes of resonance. Figure 4.10 shows this trend clearly for both tensile and compressive stresses. An interesting observation is that tensile surface stresses tend to deviate from theory more than compressive surface stress.

4.3.5 Combined Mass and Stress Loading

Effect of Combined Loading

The complete form of Equation 4.2 must be used for combined mass and stress loading. As seen in Equation 4.2, the effects on the relative frequency should be super-imposable for small surface stresses and masses. A simulation case was taken with both an added stress and mass to assess this. Cantilevers were each loaded with 1% of their masses and either an applied non-dimensionalized surface stress of 0.1 tensile, 0.0 or 0.1 compressive.

Figure 4.11 shows the relative frequency shifts with respect to the non-dimensionalized frequency for each of these cases. When a compressive surface stress is applied an upward shift was present for the first two modes. This clearly shows stress dominance. As the mode

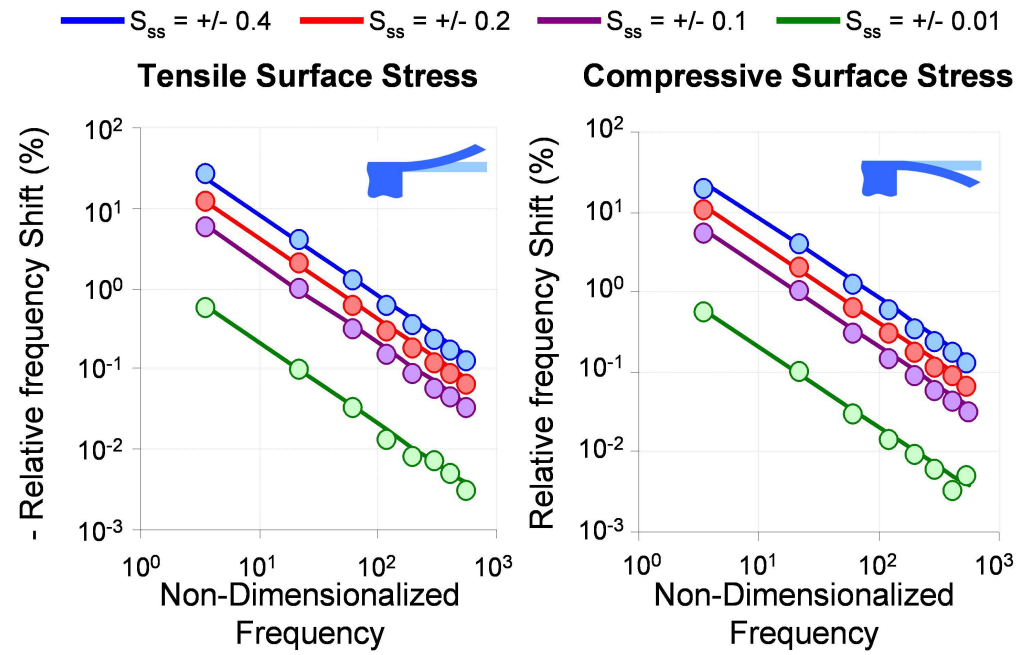

Figure 4.10: The relative frequency shift with respect to the non-dimensionalized frequency for different applied surface stresses. Theoretical values are shown as lines. All ANSYS points were averaged once they were non-dimensionalized.

of resonance is increased the relative frequency shift converges to that of the unstressed case. Furthermore, the relative frequency shift at the third mode is close to zero. This can be exceptionally troublesome in biosensor applications as a false negative can result.

The tensile surface stress also dominated the first couple of modes of resonance. However, the mass and stress frequency shifts are additive. This means that using only the first mode would result in a drastic overestimation of the additional mass. The tensile also converged to the case of zero stress at higher modes. Neglecting stress would result in a mass prediction error of 5% for compressive and 7% for tensile surface stress at the 8^{th} bending mode of resonance for these loading conditions.

Measurement Implications: A Novel Method for Decoupling Stress and Mass

The data from Figure 4.11 can be linearized in order to make a better estimation of the additional mass. Figure 4.12 shows this along with least-square linear regression best fit lines. The R^2 values of the best fit lines were 0.9993 and 0.9998 for compressive and tensile surface stress respectively. The equations of these lines are:

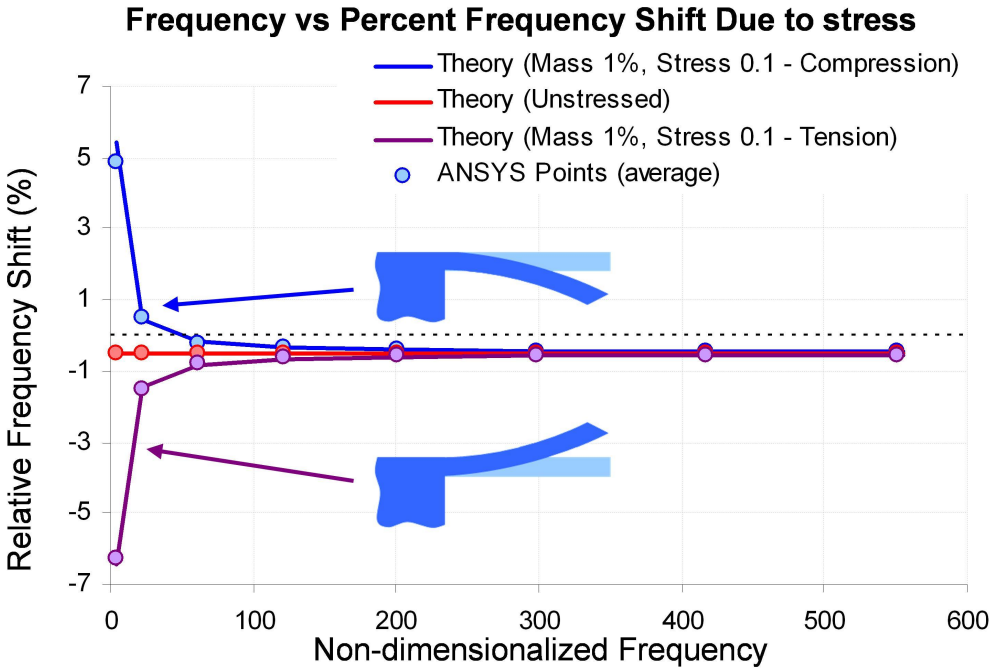

Figure 4.11: The relative frequency shift with respect to the non-dimensionalized frequency of 1% mass loaded cantilevers. Tensile stress surface causes an over prediction of the downward shift, while compressive surface stress causes and upward shift for lower modes. However, at higher modes, both converge to the unstressed relative frequency case.

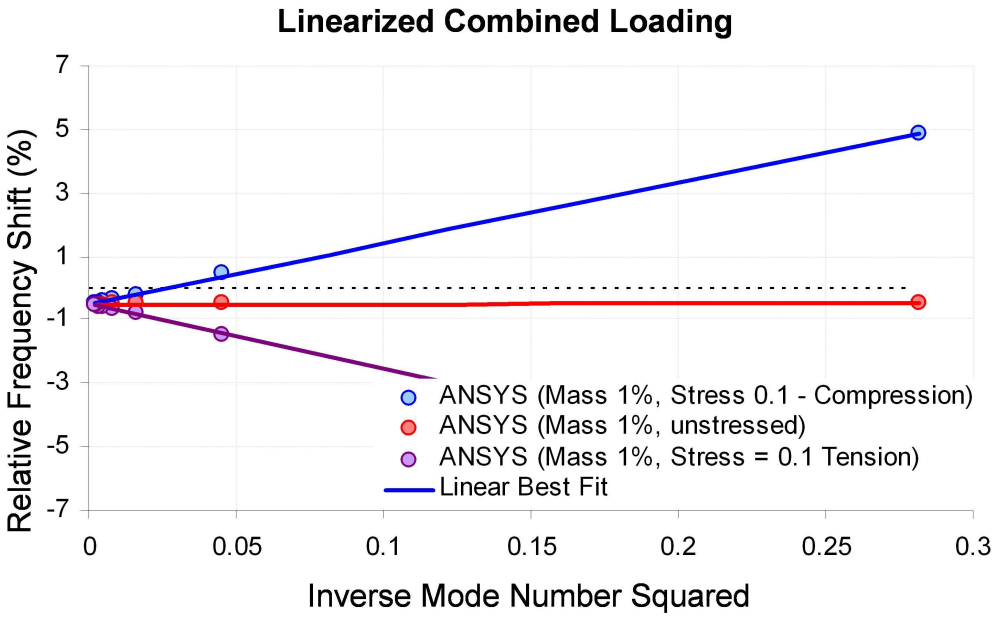

Figure 4.12: Linearized relative frequency shift plots. As $n \rightarrow \infty$ the frequency shift approaches the unstressed, mass loaded case.

$$y_{com} = 19.083x - 0.4948 \tag{4.29}$$

$$y_{ten} = 20.455x - 0.5025 \tag{4.30}$$

It can be seen that on Figure 4.12 that as $\lambda_n^{-2} \rightarrow 0$ then $f_n \rightarrow \infty$ and $\frac{\Delta f_n}{f_n} \rightarrow \frac{\Delta m}{m_{cant}}$. This means that the y-intercept of the linearized plot represents a state of pure mass loading. The added mass can be predicted to within 1% of the actual added value using these intercept values, in this case.

4.4 Cantilever Measurements

4.4.1 Cantilever Selection

Frequency measurements of cantilevers were performed on a Veeco Dimension 3100 AFM. Sections 4.2 and 4.3 have relied on higher modes of cantilever resonance in order to obtain precise mass loading measurements. However, the frequency spectrum of mechanical systems can have several different types of modes including torsional, bending (about both axis normal to the cantilever's axis) and plate bending. These modes can cause a signal that

can be measured by the optical lever method levied by the AFM. Other sources of noise may also be present in the spectrum such ambient and electronic noise.

The Dimension 3100 AFM is capable of measuring frequencies theoretically up to 5MHz. However, frequency measurements on each of cantilevers yielded peaks no higher than 3MHz (or reliably greater than 2.5MHz). This is likely due to the small amplitude of vibration associated with these high frequencies. Frequencies less than 10kHz were also difficult to determine. It is best to look at the absolute mass sensitivity because of the frequency limit given these constraints. For a uniformly distributed mass the sensitivity is normalized against the active surface capture area.

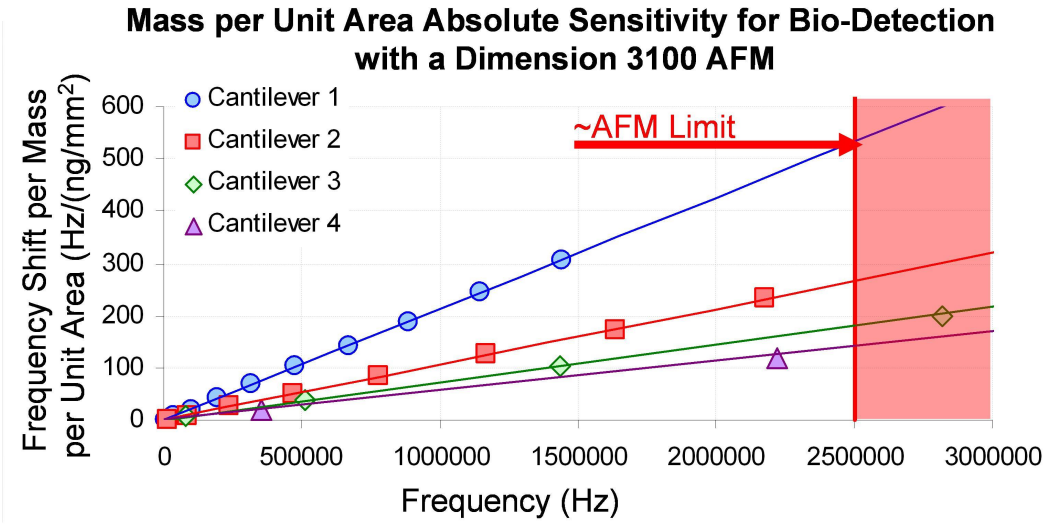

Figure 4.13: A comparison of absolute mass sensitivities per unit area of cantilevers 1 through 4. Only their first 8 modes are shown. The AFM detection limit is shown for reference.

Figure 4.13 shows the theoretical sensitivity with respect to the frequency. Each point corresponds to an accessible mode. Only the first 8 bending modes are shown for each cantilever. Cantilever 1 shows the most promising absolute mass sensitivity when higher harmonics are utilized.

4.4.2 Finite Element Analysis

Real microcantilevers are not as simple as the idealized cantilevers in Section 4.3. The side walls are sloped because they are bulk machined. Furthermore, some higher modes of resonace may be effected by the triangular tip found on most cantilevers. An example of the geometry and boundary conditions of these cantilevers is shown in Figure 4.14.

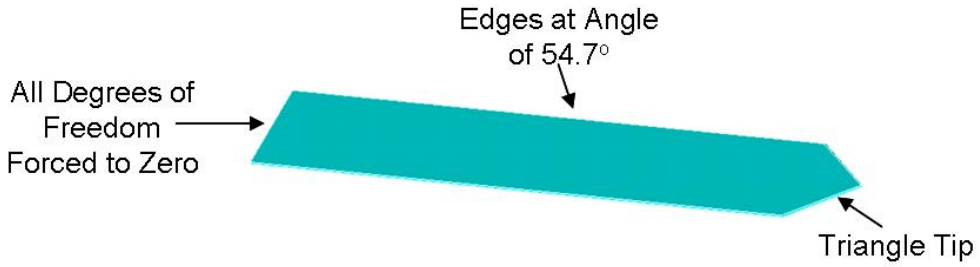

Figure 4.14: The FEA model for determining the mode numbers and bending modes of the commercially available cantilevers.

To determine the bending modes of each cantilever a FEA model was constructed for each cantilever and their unloaded frequencies were determined. Solid92 was used in the mesh because of the geometry. Solid92 is a tetrahedral element known for having less error than brick elements for irregular meshes [133]. A mesh size was picked to ensure less than 1% convergence. These modes were then normalized to determine their mode numbers. These values were used subsequently in determining the location of bending modes in the frequency response of the microcantilevers.

4.4.3 Cantilever Resonance Properties

Cantilever modal properties were determined sequentially on the AFM. The first few modes of resonance were typically bending modes. The first (or second) bending mode was then used to predict the subsequent bending modes. This was repeated so that for every mode i determined the jth mode could be found by:

$$f_j = \frac{\lambda_j^2}{\lambda_i^2} f_i. \tag{4.31}$$

It is important to note that f_i is the last measured mode and f_j is the next predicted mode. The frequency of each mode determined was used to find the next one. The convergence of this prediction can be seen in Figure 4.15. As excepted, modes closer to the frequency provided better estimations. This was vital in isolating the bending modes of a cantilever. For example, Figure 4.16 shows a typical spectrum and the predicted frequencies using this method of a TL-Arrow cantilever.

This method allowed for predicting bending modes of resonance to generally less than 2kHz error. The deviation is most likely due to neglecting the damping caused by air. The

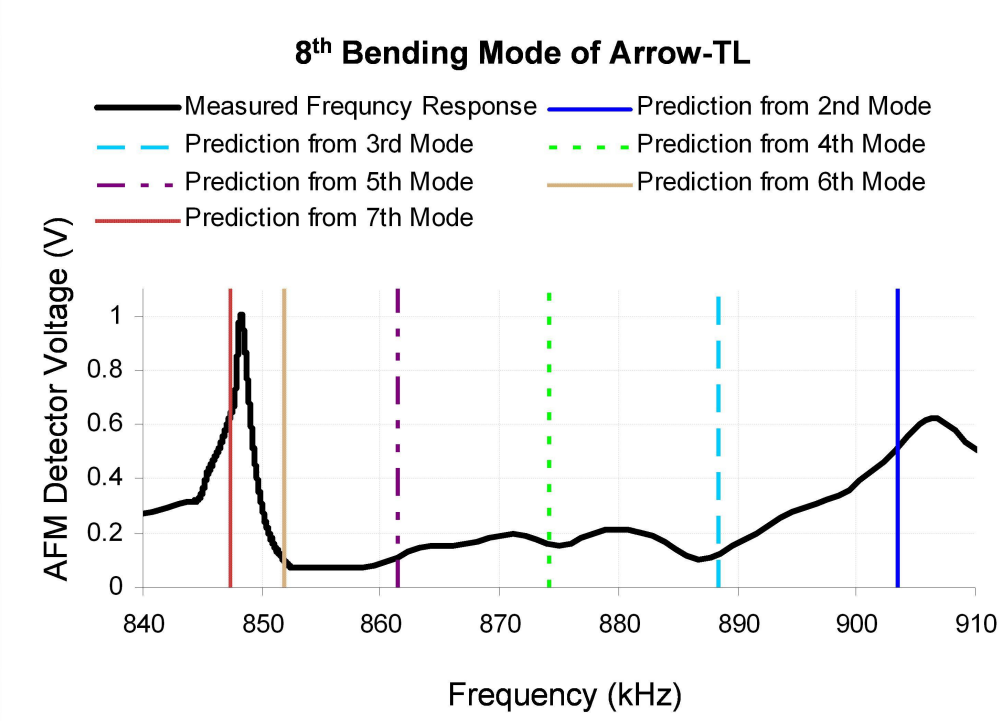

Figure 4.15: The convergence of using higher measured modes to predict a sequential mode. The final prediction typically yielded less thank 2kHz error.

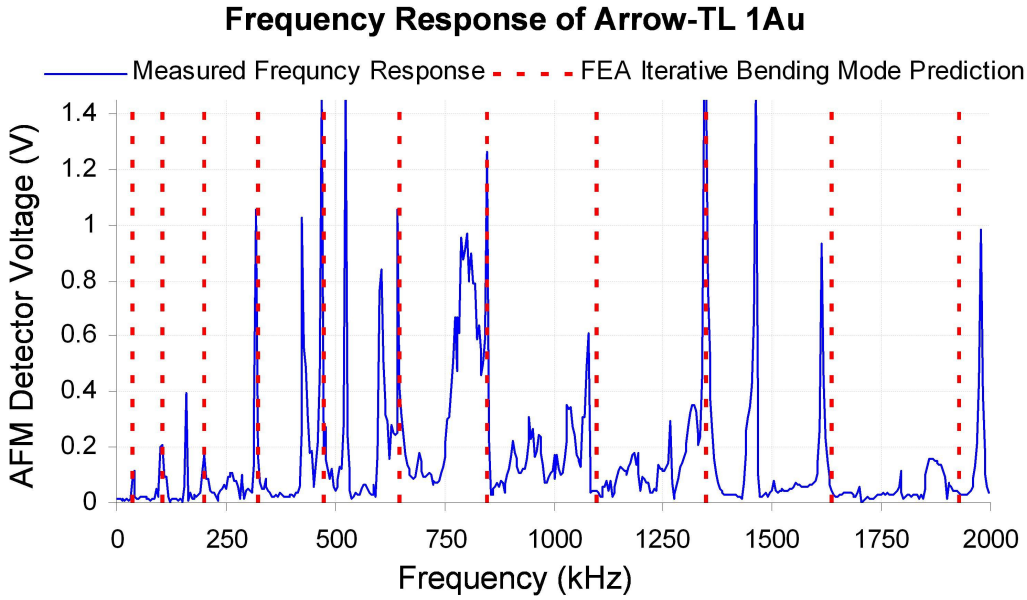

Figure 4.16: Frequency response of a Arrow-TL-1Au cantilever. The frequency spectrum is full of peaks, however the bending modes can be determined with good accuracy.

error was an order of magnitude larger for frequencies greater than the 10th mode. This is likely due to deviation from the ideal case.

The amplitude of a given mode of resonance was dependant on the position of the laser on the beam. The beam was originally focused on the tip, but some modes were not detectable when this was the case (or of very small amplitude). As such, the laser was moved along the beam. This allowed the frequency response to be detected at various positions. The peak amplitude was then optimized with respect to the beam position. This proved especially important with higher modes of resonance.

4.5 Experiment: NeutrAvidin Detection

Overview

In order to validate these equations further, cantilever protein detection was carried out using TL-CONT cantilevers. The cantilevers were functionalized with biotin and then exposed to NeutrAvidin. Biotin is known to bind specifically with variants of the avidin protein. [44].

Materials and Methods

NeutrAviden and Phosphate Buffered Saline (PBS) were obtained from Pierce Biotechnology (Nepean, Canada). TL-CONT microcantilevers were obtained from NanoAndMore (Lady's Island, USA). Both sides of the cantilevers were sputtered with a 2nm chrome adhesion layer and 20nm of gold.

TL-CONT cantilevers were chosen because the first mode of resonance was below detectable levels. Microcantilevers were resonated and their corresponding bending modes were determined by the methods outlined in Section 4.4. Microcantilevers were subsequently immersed in 1mM of NHS-SS-Biotin dissolved in MilliQ water overnight. After brief rinsing, cantilevers were dried in nitrogen and resonated. Negligible frequency shift was observed.

Microcantilevers were subsequently immersed in 1mg/mL of NeutrAvidin dissolved in PBS buffer for 15 minutes. Cantilevers were rinsed in PBS and water, followed by nitrogen drying and then resonated.

Results and Discussion

The first 4 modes of resonance showed frequency shifts too small to be reliably measured on the AFM. These shifts were considered statistically insignificant. The fifth, sixth and

seventh bending modes showed measurable frequency shifts. From each of these shifts the added mass was calculated neglecting the effect of stress. The points were then plotted, linearized and a best fit for the points was determined. Figure 4.17 shows these calculated values.

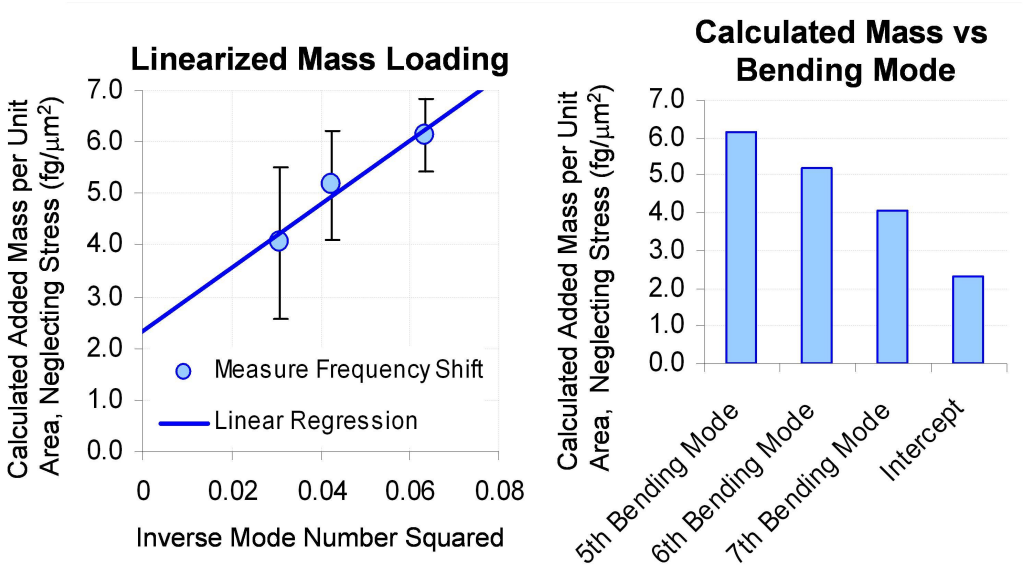

Figure 4.17: Left: The calculated added mass per unit area with respect to the inverse mode number squared

The upward slope of the linear regression demonstrates the presence of a compressive stress. The best estimate of the added mass of the cantilever is obtained from the linear regression's intercept, which corresponds to a mass per unit area of 2.3 mg/m^2. These results demonstrate that with knowledge of several modes of resonance, contributions from stress and mass can be decoupled.

4.6 Conclusions

A detailed analysis of the effect of small surface stresses on the higher modes of microcantilever resonance has been carried out. A formulation of the effect of small surface stresses on cantilever resonance was derived in the context of Euler-Bernoulli theory with the addition of an axial load. This demonstrated that higher modes of resonance are more sensitive to mass, and less sensitive to stress. Surface stress causes a constant frequency shift, while mass loading causes constant relative frequency shift. These concepts were then verified with extensive FEA. Subsequently, a novel method for determining a mass

load in the presence of a surface stress was utilized by linearizing the response. Finally, experimental verification was demonstrated with the detection of NeutrAvidin.

5

Surface Immobilization of T4 Phages for Specific Bacterial Capture

5.1 Overview

This chapter focuses on enhancing the attachment of phages to gold surfaces for bacterial capture. Gold surfaces are used as a template because of their ease to chemically modify and widespread use in the biosensor community. However, the methods here can be applied to any surface with the prerequisite functional surface groups. The T4 phage was used as a model bacteria recognition element to demonstrate strain level specificity.

5.2 Materials

T4 phages and all *E. coli* bacterial strains (6M1N1, EC12, NP10, NP30) were obtained from Biophage Pharma Inc. (Montreal, Canada). SYTO BC bacterial stain B7277 was obtained from Invitrogen (Carlsbad, CA, USA). Bovine Serum Albumin (BSA), cysteamine hydrochloride, ethanolamine, glutaraldehyde, L-cysteine and L-histidine were purchased from Sigma Aldrich (St. Louis, MO. USA). Dextrose and sucrose were purchased from Merck and Co., Inc (NJ, USA). Tween-20 was purchased from MP biomedicals, Inc (OH, USA).

Luria Bertani (LB) media was purchased from Quelabs (Montreal, Canada). LB media was prepared by dissolving 25 g of LB media in 1 L of MillQ water. For LB top agar,

6 g of agar was added to 400 mL of LB media. Phosphate Buffered Saline (PBS) buffer was purchased from Pierce Biotechnology (Nepean, Canada) and made by dissolving one package in 500 mL of MilliQ water.

Tryptic Soy Broth (TSB) and SM buffer were made using reagents from Sigma-Aldrich. TSB was made by dissolving 5 g of NaCl, 5 g of soytone and 15 g of tryptone in 1 L of MillQ water. Then 5% TSB solution was made by mixing 50 mL of TSB solution in 950 mL of 0.15 M NaCl and 5% TSB Tween-20 (5% TSBT) was made by adding Tween-20 so that the solution was 0.05% Tween-20 by volume. SM buffer was made by mixing 5.8 g of NaCl, 2 g of $MgSO_4 \cdot 7H_2O$, 50 mL of 1 M Tris-hydrochloride (pH-7.5) and 1 mL of 10% (w/v) gelatin in 1 L of MilliQ water.

Ethanol and Isopropanol were purchased from the University of Alberta Chemistry Lab Stores. LB broth, TSB broth and SM buffer were all autoclaved before use.

5.3 Methods

5.3.1 Bacteria Amplification

Four different strains of *E.coli* were used in the following experiments: one host (EC12) and three controls (6M1N1, NP10, NP30). All bacteria were cultured and enumerated in a similar fashion. Bacteria was streaked onto LB plates from glycerol stocks. A different plate was used for each strain of bacteria. Four overlapping streaks were made on the plate in order to form single colonies. This plate was then allowed to grow overnight in a 37^oC incubator. The plate was subsequently stored at 4^oC up to 15 days and used as necessary.

Primary cultures were created by picking 3 to 5 single colonies from a given plate. These colonies were then place in 5mL of LB broth and grown for 4-7 hours at 37^oC and 200 RPM. Cultures were removed once they had a very turbid optical density. These cultures were stored and used for up to one week.

5.3.2 Bacteria Enumeration

To determine the concentration of a given bacteria culture, the plate count method was used. A bacteria sample was diluted several times. For each dilution, a 10 μL drop was dispensed on a LB plate. The plate was then incubated overnight at 37^oC. Subsequently, the dilutions that produced isolated colonies were counted. The concentration was the determined from the number of colonies and the dilution factor. Approximately 5 colonies were typically

counted in the 10^{-6} dilution, which corresponds to a concentration of 5x10^8 cfu/mL. This concentration was used in all subsequent bacterial capture experiments.

5.3.3 T4 Phage Amplification

The stock of T4 phages was amplified in order to increase the concentration and amount of phage. The stock source of phage (10^8 pfu/mL), was diluted by 100x. Then 100 μL of this dilution was then added to a culture of *E.coli* EC12 (host bacteria). After briefly mixing the mixture was allowed to sit for approximately 15 minutes. The infected culture was then added to 250 mL of LB broth in a 500 mL Erlenmeyer flask. The flask was covered in parafilm and incubated at 37^{o}C and 180 RPM.

The infection was incubated until a significant amount of bacterial debris was observed in the flask. This typically took 4 to 7 hours. The resulting lysate was then poured into several 50 mL falcon tubes and centrifuged at 4000 RPM for 8 minutes to remove the majority of the bacterial debris. The supernatant was then poured through a 220 nm pore vacuum filter to further purify the phages from other lysis products. The phages were stored in this solution at 4^{o}C until required.

Then 20 mL of LB-T4 solution were then poured into 8 polycarbonate ultracentrifuge tubes to further concentrate to phage. The tubes were then placed in a Beckmann ultracentrifuge and centrifuged at 55 000 RPM for 1 hour. The 2 0mL of liquid was then gently poured out, followed by the addition of 1 mL of SM buffer. The tubes were left overnight at 4^{o}C to allow the phages to desorb. Subsequently, the solution was briefly mixed, followed by a second filtering with a 220 nm pore syringe filter. This process typically yielded between 1x10^{12} and 8x10^{12} pfu/mL. The SM-T4 solutions used in subsequent surface immobilization experiments were diluted to 10^{12} pfu/mL for consistency.

5.3.4 Phage Enumeration

Phage enumeration was accomplished using the plaque counting method. Four milliliters of LB top agar was heated to 50^{o}C. Then 100 μL of host bacteria was added to the LB top agar and was briefly mixed. The mixture was then poured on a LB plate and allowed to spread across the plate. The SM-T4 solution was then diluted several times and 10 μL drops of each dilution were dispensed on the plate. The plate was then incubated overnight at 37^{o}C. The plaques that formed were then visible the next day by the absence of bacteria. Plaques

were counted from a dilution that resulted in single isolated plaques and the corresponding concentration was determined.

5.3.5 Bacteria Adsorption Preparation

One milliliter of bacteria were taken from a culture and spun at about 13 000 RPM in an epindorff centrifuge for 1 minute. This caused the bacteria to pellet at the bottom of the epindorff tube. The supernatant was removed by pipette and the pellet was resuspended in equal volumes of either 5% TSB or PBS buffer. The bacteria concentration was determined by colony counting after changing the buffer and showed no measurable effect on concentration.

The bacteria were fluorescently stained after changing the solution. This was achieved by adding 1 μL/mL of SYTO BC stain to the bacteria. SYTO BC stain is a mixture of several different nucleic acid stains and has a maximum absorbance and emission at 485 nm and 500 nm for DNA, respectively [134]. After brief mixing, the suspension was allowed to sit for five minutes prior to use. Exposure to light was minimized to prevent degradation of the stain before observation. All bacteria capture experiments were performed at room temperature.

5.3.6 Surface Preparation

Prime silicon $< 100 >$ wafers were scored 100 μm deep into 5 mm by 7 mm rectangles using a dicing saw. Wafers were then sonicated in isopropanol to remove access debris followed by a piranha clean ($3H_2SO_4$:$1H_2O_2$) for 20 min. Wafers were then dried and immediately sputtered with 3 nm chrome adhesion layer followed by 20 nm of gold. Gold chips could easily be cleaved from the wafer while producing minimal particulate by using the score lines. Gold chips were stored in laboratory conditions for a few months before being discarded.

Prior to surface functionalization, the gold chips were sonicated briefly in isopropanol to remove any particulate from the surface. The chips were then dried with nitrogen followed by 1 hour of cleaning at 70^{o}C in a Novascan UV cleaning system. The cleaning mechanism is expected to be a result of the UV light and ozone produced by the UV light to remove organic contamination [135]. The contact angle of water on the chips reduce to zero after cleaning to confirm clean gold. Gold chips were then placed in 95% ethanol for 20 minutes to reduce any gold oxide that may have formed [136].

5.3.7 Physical Adsorption of Phages on Gold

Gold chips were cleaned as mentioned above followed by a brief rinse in MilliQ water and SM buffer. The chips were then placed in $6x10^{12}$ pfu/mL SM-T4 phage solution overnight. Samples for SEM were then rinsed briefly in SM followed by MilliQ water. The SEM samples were then dried with nitrogen and imaged.

Surfaces for bacterial capture were briefly rinsed in SM, water and PBS buffer and subsequently blocked with 1mg/mL of BSA in PBS for 30 minutes. After a brief rinse in PBS and 5% TSB, the surface was then exposed to either stained host bacteria or control in 5% TSB for 30 minutes. After a brief rinse in 5% TSB, surfaces were washed in 5% TSBT for 5 minutes, followed by two brief rinses in 5% TSB. Bacteria surface capture was then enumerated using fluorescent microscopy.

5.3.8 Amino Acids and Simple Sugars for Enhanced Phage Adsorption

Clean surfaces were immersed in 25 mM solutions of either cysteine, histidine, dextrose or sucrose in MilliQ water. Adsorption of histidine and cysteine were at 60^oC, while sucrose and dextrose were adsorped at room temperature. Following brief rinses in MilliQ water and SM, each surface was exposed to SM-T4 at either 20^oC, 40^oC, 50^oC or 55^oC. Following brief rinses in SM and MilliQ water, SEM samples were dried in nitrogen.

Bacteria capture samples were rinsed in SM, MilliQ water and PBS buffer followed by being submerged in 1 mg/mL BSA in PBS buffer for 30 minutes. Subsequently, samples were briefly rinsed in PBS and 5% TSB, before being exposed to bacteria for 30 minutes. Samples were then rinsed briefly with 5% TSB and washed in 5% TSBT for 5 minutes. The samples were then rinsed twice in 5% TSB before being observed in the fluorescent microscope.

5.3.9 Covalent Attachment of Phages

Cleaned gold surfaces were placed in solutions of 25mM cysteamine or cysteine in MilliQ water overnight. The samples were then rinsed well in MilliQ water. The samples were then placed in 2% glutaraldehyde for 1 hour. The samples were briefly rinsed in MilliQ water and then placed in SM-T4 solution at 40^oC overnight. Subsequently, the samples were rinsed in SM buffer followed by MilliQ water. SEM samples were then nitrogen dried. A summary of this immobilization procedure can be seen in Figure 5.1.

The samples for bacteria capture were rinsed in PBS buffer and blocked with 1mg/mL

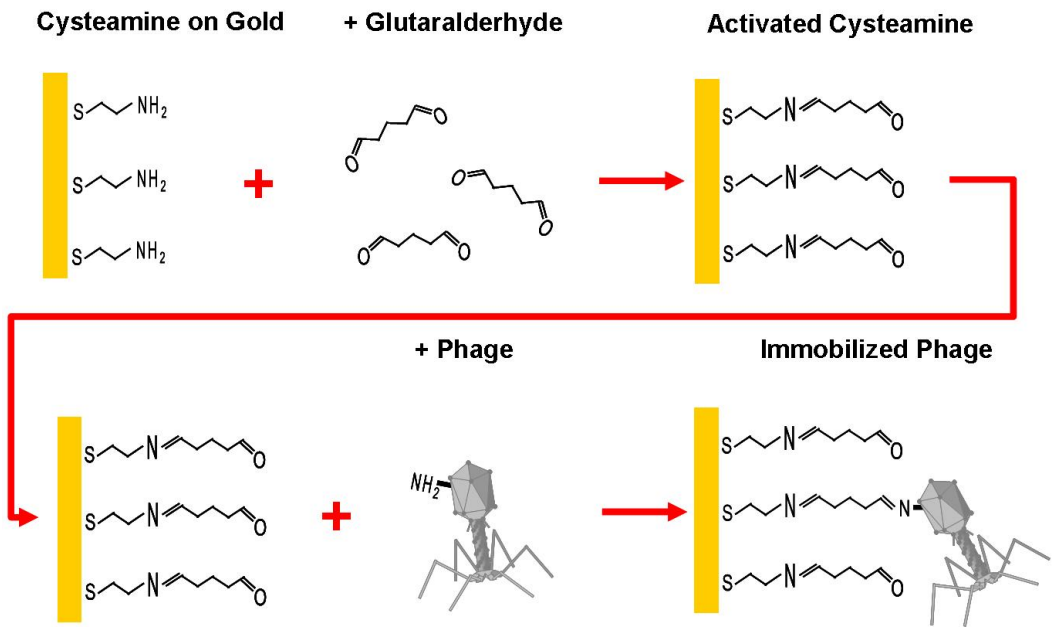

Figure 5.1: The covalent immobilization process employed. Cysteine or Cysteamine (shown) SAM is formed followed by glutaraldehyde activation. Phages are then exposed to the surface. Free amine groups on the phage will then react with the surface.

BSA in PBS buffer for 30 minutes. Subsequently, samples were rinsed in PBS and 5% TSB buffer prior to exposure to bacteria in 5% TSB for 30 minutes. The samples were then rinsed in 5% TSB, washed in 5% TSBT for 5 minutes, and rinsed twice in 5% TSB before being observed in the fluorescent microscope.

5.3.10 Scanning Electron Microscopy and Phage Surface Density Determination

After nitrogen drying, samples were baked at 60^{o}C for 10 min to desorb remaining water. Samples were the loaded into a Hitachi HR-4800 SEM. Images were typically taken 3 to 8 hours after SEM flashing. Longer time resulted difficulty imagining the phages. Images were taken at an accellerating voltage of 1 kV and current of 20 μA. Deceleration mode was used with an accelerating voltage of 2.5 kV and a decelerating voltage of 1.5 kV for higher magnification images. Phages in a given image were then counted and their density per unit area was determined. Several samples and images were used so an average and standard deviation could be determined. Phage densities are quoted as the average counted phages per unit area plus or minus the standard deviation.

5.3.11 Fluorescent Microscopy and Bacteria Surface Density

Following rinsing, the surfaces were imaged in a Olympus IX81 Inverted Fluorescence Microscope. Plastic microscope slide with a 1 cm hole drilled in the center to create a fluid cell. A microscope slide cover was then placed over the hole on one side and held in place with a vaseline seal. The fluid cell was filled with 200 μL of buffer. The fluid cell set up is shown in Figure 5.2.

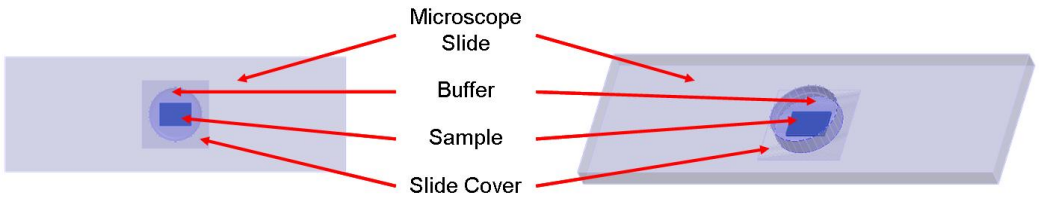

Figure 5.2: A fluid cell was used to image fluorescently stained bacteria captured on gold surfaces. A hole was drilled in a plastic microscope slide. A cover slip was mounted for each experiment by using vasoline as an adhesive. The well was filled with buffer and the sample was placed face down allowing the surface to be imaged.

The sample was then placed face down in the fluid cell. The SYTO stain can be observed using the FITC filter [134]. Images were typically taken at 10x, 20x, 40x and 64x. Zoomed in images were taken in areas that appeared to be representative of the sample as viewed at 10x. Bacteria densities were then counted over a single image and divided by the area of that image to get bacteria surface densities. Densities were calculated over several samples so that an average and standard deviation could be calculated. Bacterial densities are quoted as the average counts per unit area plus or minus the standard deviation.

5.4 Physical Adsorption of Phages on Gold

Simple physisorption of phages on gold was employed as reference standard for comparative purposes. SEM revealed very small densities of physically adsorbed phages on the gold surface. This corresponds to about 0.5 ± 0.1 phages/μm^2. Host bacteria capture yielded 1.1 ± 0.1 bacteria/100μm^2. Control bacteria also showed insignificant binding. This indicates that BSA is providing adequate blocking and the phage is specific. These results are summarized in Figure 5.3.

While gold does physically adsorb phages, the densities are fairly small. It may be possible to improve chemical adsorption of the phages by modifying the surface chemical group of the gold.

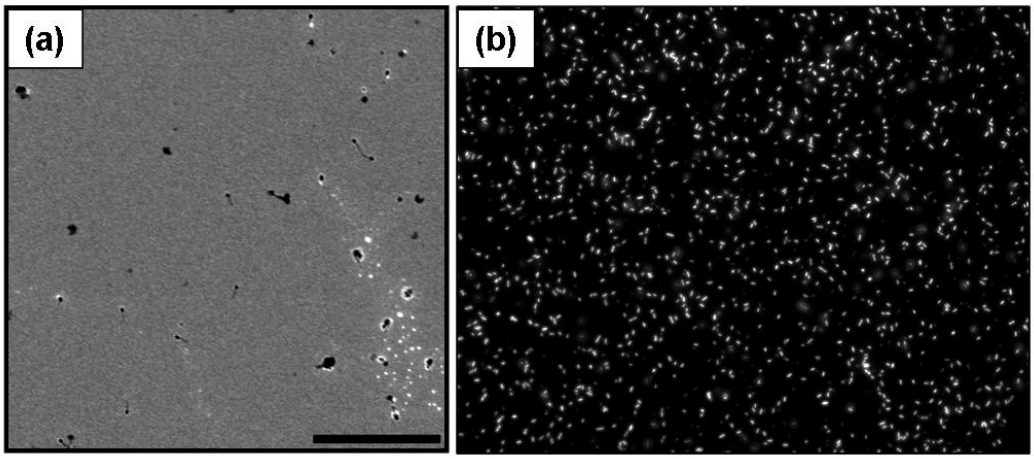

Figure 5.3: (a) SEM of T4 Phages physically adsorbed on to gold. The scale bar is 2μm. (b) Fluorescent image of bacteria capture from physically adsorbed phages taken at 40x.

5.5 Amino Acids and Simple Sugars for Enhanced Phage Adsorption

Enhanced phage densities can be realized by modifying gold with the adsorption of simple sugars, amino acids or a SAM prior to phage adsorption. By using several different molecules some insight into the chemical surface groups available on the phages can be gained.

Gold modification proved very effective in terms of increasing phage densities. Histidine adsorption prior to phage adsorption yielded phage densities of 1.6 ± 0.5 phage/μm^2 and bacterial capture of 2.3 ± 0.1 bacteria/100μm^2. This represents a 2-fold increase in phage densities and bacterial capture as compared to physical adsorption. Histidine was expected to bind to free amine groups on the phage through hydrogen bonding with the histidine carboxyl group [137]. It is likely that the histidine did not form a complete nor stable monolayer on the gold, which would cause suboptimal adsorption. This is because histidine attaches to the gold though physical adsorption.

Dextrose and sucrose adsorption both yielded even higher phage densities at 2.4 ± 0.5 and 3.7 ± 0.5 phage/μm^2, respectively. Bacterial adsorption was also significantly higher at 2.5 ± 0.1 and 4.0 ± 0.1 bacteria/100μm^2, respectively. The additional adsorption ability can be explained by the increased wettability of the surface, driving the phage binding. This was due to the presence of many hydroxyl groups on both sugars. These sugars however were still loosely bound to the surface and surface densities were not always uniform.

In order to improve surface uniformity cysteine was used, which has a thiol group that

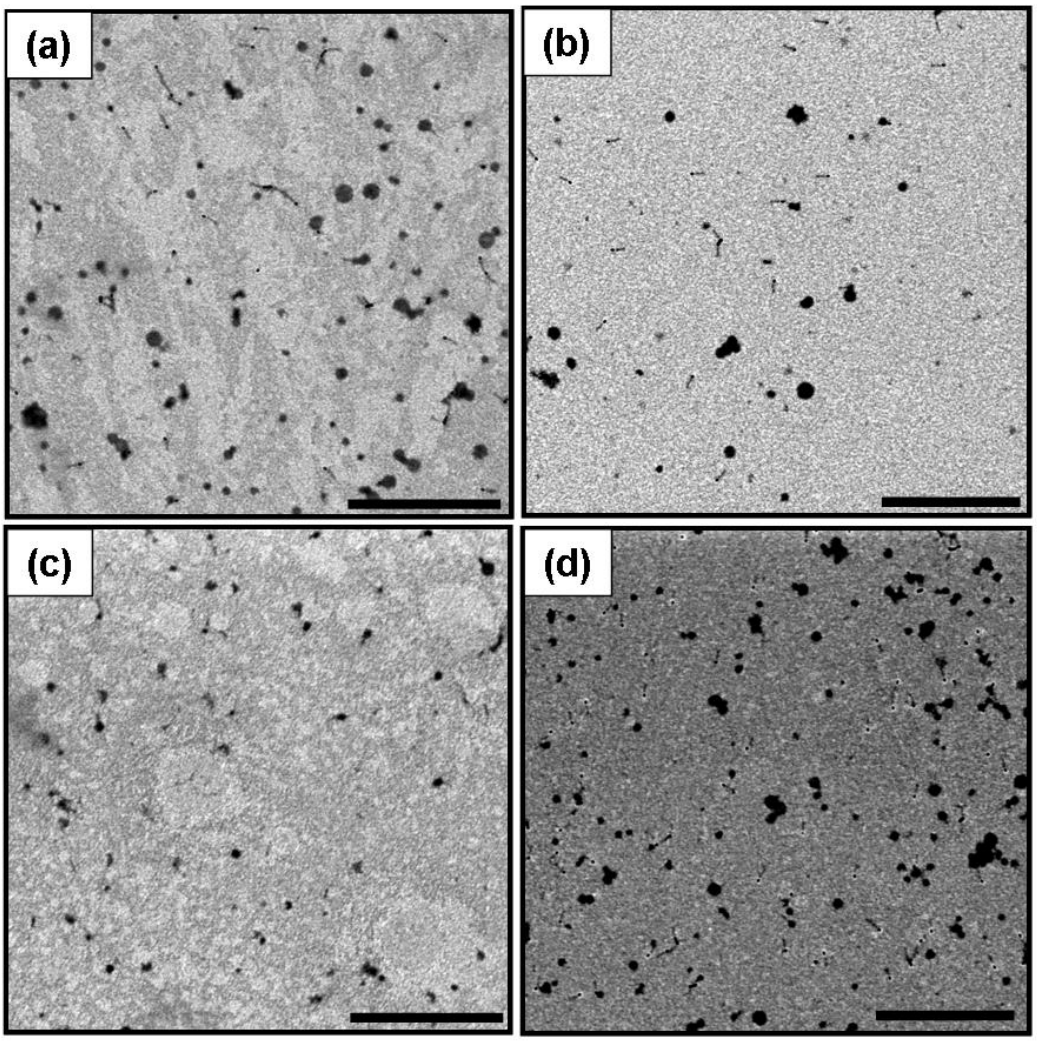

Figure 5.4: Phage adsorption on gold functionalized with (a) dextrose, (b) sucrose, (c) histidine and (d) cysteine. All scale bars are 2μm.

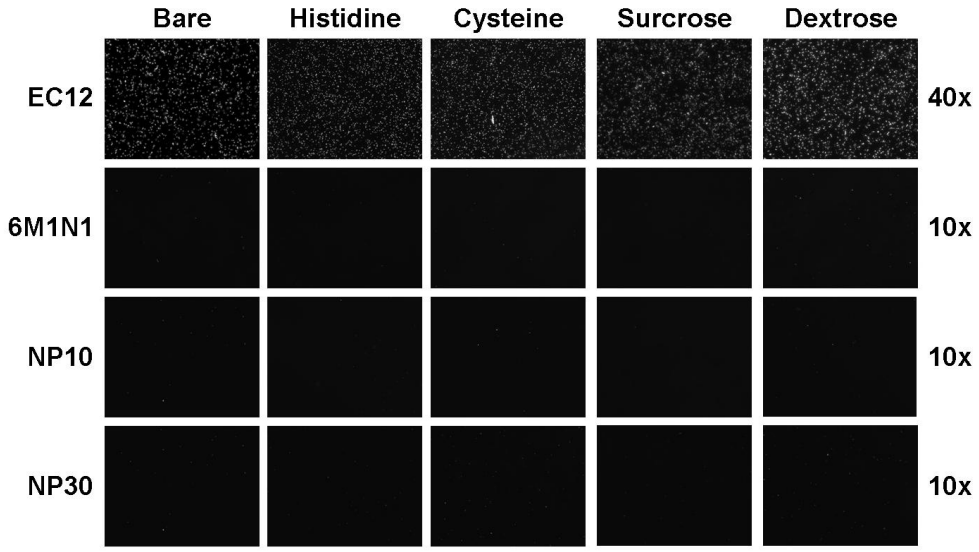

Figure 5.5: Bacteria capture of host (EC12) and control (6M1N1, NP10, NP30) on various gold modifications. Host strain images were taken at 40x and control strain images were taken at 10x.

is well known for binding to gold. This achieved phage densities of 3.4 ± 0.5 phages/μm^2 and bacterial capture of 3.9 ± 0.2 100μm^2. For all surfaces, 6M1N1, NP10 and NP30 *E.coli* strains showed negligible binding, which verified the specificity of the system. Phage concentrations used in all the above experiments were 6x10^{12} pfu/mL. These results are summarized in Figure 5.4 and 5.5.

It is well established that the temperature of a solution can have and effect on the kinetics of adsorption. The temperature dependance of phage adsorption was also studied to examine this effect. However, phage concentrations used in subsequent experiments were reduced to 10^{12} pfu/mL. Cysteine was exposed to phages at room temperature, 40^{o}C, 50^{o}C and 55^{o}C. Increasing the adsorption temperature to 40^{o}C effectively increased the phage density from 3.4 ± 0.5 phages/μm^2 to 7.2 ± 0.7 phages/μm^2. Bacterial capture also doubled with higher temperature phage adsorption.

At 50^{o}C phages began to clump together making quantification erroneous. Furthermore, reduction in bacterial capturing capacity was also observed. At 55^{o}C clumping was dominant and phages were typically uncountable. Significant reduction in bacterial capture was observed. A significant increase in background fluorescence was noticed, possibly to due to the damaging of the phages, which allowed their DNA to be exposed to free nucleic acid stain.

The adsorption of T4 phages can be increased by modifying the surface chemical group.

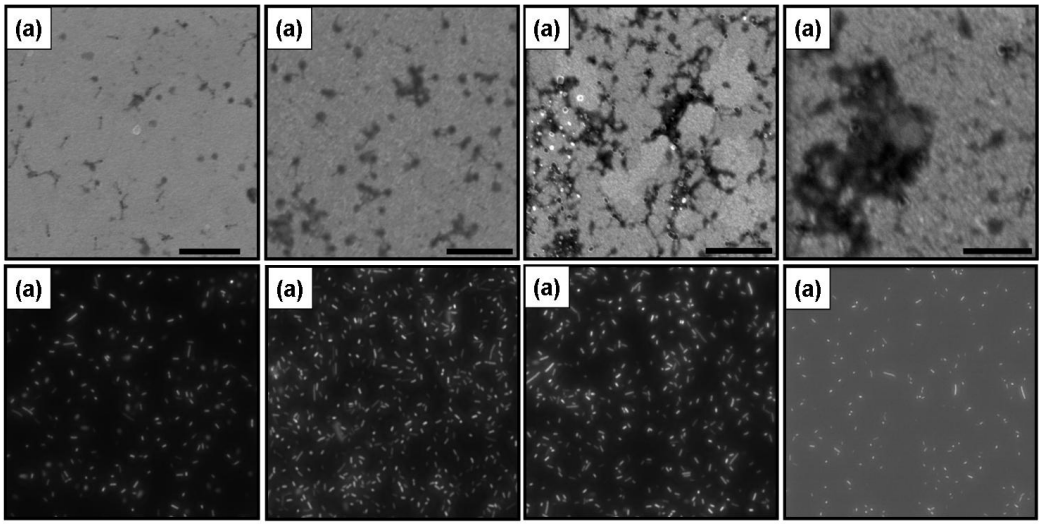

Figure 5.6: SEM images of phages immobilized at (a) room temperature, (b) 40^{o}C, (c) 50^{o}C and (d) 55^{o}C. Host bacteria capture of surfaces with phages immobilized at (e) room temperature, (f) 40^{o}C, (g) 50^{o}C and (h) 55^{o}C. Bacterial capture is a maximum at 40^{o}C. The scale bars for (a), (b) and (c) are 2 μm and the scale bar for (d) is 1 μm.

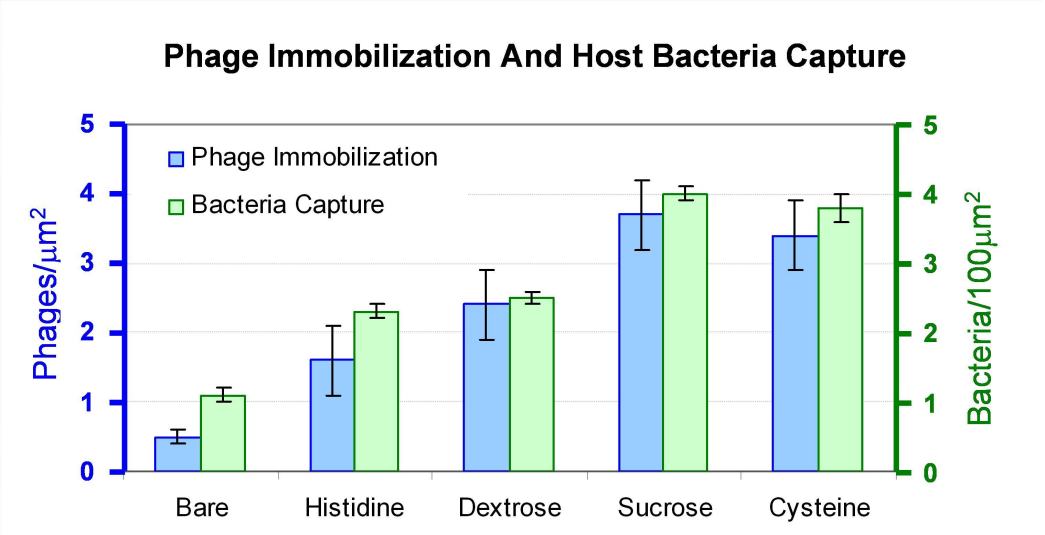

Figure 5.7: The number of phages adsorbed for a given surface modification and the corresponding host bacteria capture.

This corresponds to an increase in bacterial capture. This is most likely due to hydrogen bonding between free surface groups on the phage and the adsorbed molecule. A significant number of these groups are present on the head of the phage because bacteria capture was increased. Furthermore, adsorbing phages at higher temperatures has also been shown to increase the phage surface density and bacterial capture. Thus, subsequent phage immobilizations were carried out at 40^{o}C.

5.6 Covalent Attachment of Phages

Amine groups can be targeted to covalently attach the phages on to gold surfaces to further improve phage immobilization. Because the phage head is comprised of proteins, there should be a significant amount of free amine groups. Targeting amine groups can be accomplished in several different ways [17]. Here glutaraldehyde activated cysteamine and cysteine SAMs are investigated for this purpose. Glutaraldehyde is known to react with amine groups at its aldehydic terminal groups. As such, glutaraldehyde can be used to crosslink two amine groups by forming two separate bonds [138]. By modifying a surface with a SAM that has a free glutaraldehyde activated amine group, it will effectively capture other amine groups.

Glutaraldehyde activation of both cysteine and cysteamine resulted in large increase in phage densities. Activated cysteine and cysteamine yielded phage densities of 17 $\pm$ 1 phages/μm^2 and 18.0 $\pm$ 0.1 phages/μm^2. This represents about a 35-fold increase compared to the physical adsorption case. Activated cysteine and cysteamine also yielded bacterial capturing abilities of 5.3 $\pm$ 0.6 bacteria/100μm^2 and 11.9 $\pm$ 0.2 bacteria/100μm^2.

Control bacteria did not significantly adsorb to the surface. These results are summarized in Figures 5.8 and 5.9.

By specifically targeting free amine groups on the phage, significant improvements in phage densities and bacterial capture were realized. This was achieved while maintaining low non-specific binding.

5.7 Conclusions

In this chapter several different processes for immobilizing phages onto gold surface have been investigated. A highly effective covalent phage immobilization procedure has been developed. Non-specific binding has remained low (much less than 1 bacteria/100μm^2), which demonstrated the specificity of a phage based sensor.

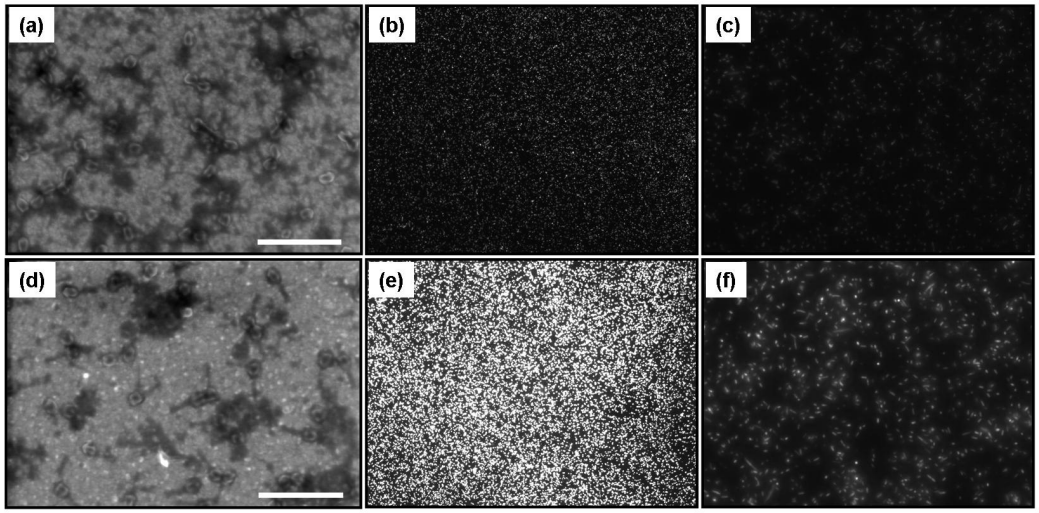

Figure 5.8: Activated cysteine (a) phage capture, (b) bacteria capture (10x) and (c) bacteria capture (64x). Activated cysteamine (d) phage capture, (e) bacteria capture (10x) and (f) bacteria capture (64x).

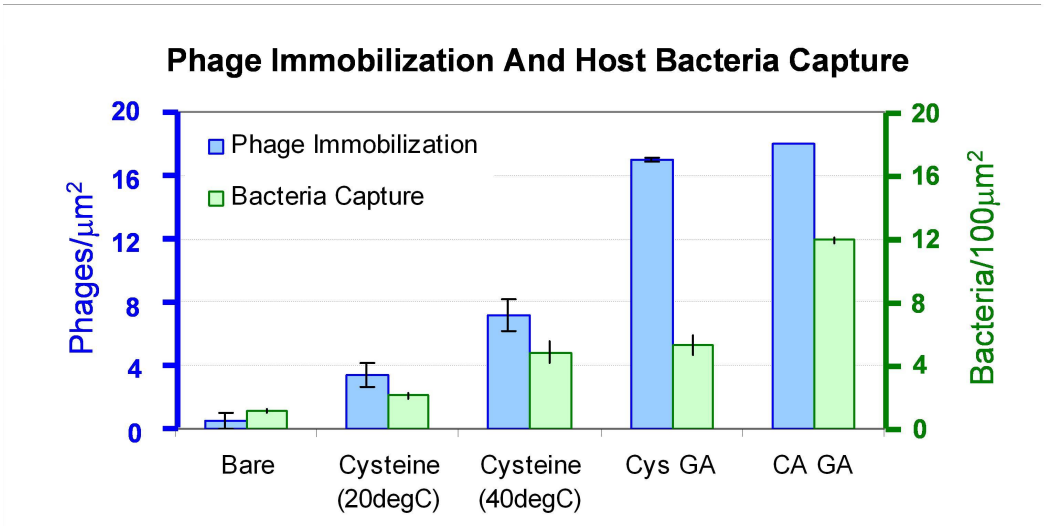

Figure 5.9: Phage immobilization densities and host bacterial capture of glutaraldehyde activated cysteine (Cys GA) and cysteamine (CA GA). Cysteine phage densities and host bacteria capture (at room temperature and 40^{o}C) are shown for reference.

6

Phage Functionalized Microcantilevers for Bacteria Detection

6.1 Overview

This chapter combines the developments in Chapter 4 and Chapter 5 with proof-of-concept phage based microcantilever bacterial detection. Several unexpected challenges are outlined.

6.2 Materials

TL-Arrow-Au-2 and TL-CONT cantilevers were obtained from NanoAndMore (Lady's Island, USA). T4 phages and *E. coli* bacteria (6M1N1, EC12, NP10, NP30) were obtained from Biophage Pharma Inc. (Montreal, Canada) and SYTO BC nucleic acid stain (B7277) was obtained from Invitrogen (Carlsbad, CA, USA). Bovine serum albumin (BSA), cysteamine hydrochloride, glutaraldehyde, and L-cysteine were purchased from Sigma Aldrich (St. Louis, MO. USA). Tween-20 was purchased from MP biomedicals, Inc (OH, USA).

LB media was purchased from Quelabs (Montreal, Canada). LB media was prepared by dissolving 25 g of LB media in 1 L of MilliQ water. LB top agar was made by dissolving 6 g of agar in 400 mL of LB media. PBS buffer was purchased from Pierce Biotechnology (Nepean, Canada) and prepared with one package in 500 mL of MilliQ water.

TSB was made by dissolving 5 g of NaCl, 5 g of soytone and 15 g of tryptone in 1 L of MilliQ water. Five percent TSB solution was made by mixing 50 mL of TSB solution in 950 mL of 0.15 M NaCl. Five percent TSB Tween-20 (5% TSBT) was made by adding Tween-20 so that the solution was 0.05% Tween-20 by volume. SM buffer was made by mixing 5.8 g of NaCL, 2 g of $MgSO_4 \cdot 7H_2O$, 50 mL of 1 M Tris-hydrochloride (pH-7.5) and 1 mL of 10% (w/v) gelatin in 1 L of MilliQ water. All reagents for the TSB and SM buffer were from Sigma-Aldrich.

LB broth, TSB broth and SM buffer were autoclaved before use. Ethanol and isopropanol were obtained from the University of Alberta Chemistry Lab Stores.

6.3 Methods

6.3.1 Surface Drying of Bacteria

The cantilever sensors were operated in air in order to bypass sensitivity reductions associated with fluidic mass loading and viscous dampening in water. As such, several different drying procedures were evaluated by SEM. Processes were roughly based on procedures found in Bozzola and Russel for SEM sample fixation of bacteria [139].

Surfaces were functionalized with cysteine, phages and exposed to bacteria as outlined in the process below. The surfaces were then either fixed with 2% glutaraldehyde (GA), fixed and dehydrated with ethanol in increasing concentrations (24%, 48%, 71%, 95% ethanol in water), or unmodified. These surfaces were either allowed to dry by evaporation or were blown with nitrogen.

There was significant bacteria coverage for unfixed surfaces, however bacteria distribution was very non-uniform across the surface. Air drying had slightly more attached bacteria then nitrogen drying. Ethanol dehydration and fixation showed virtually no bacterial capture. This is likely caused to the osmotic pressure induced to the the concentration gradient of ethanol across the bacteria. These results were consistent for both air and nitrogen drying.

Glutaraldehyde fixation produced non-uniform bacteria distributions when air dried and fairly uniform bacteria distributions when dried with nitrogen. When fixation is followed by ethanol dehydration bacteria densities are extremely uniform when nitrogen dried. However, when air dried these surface had virtually no bacteria attached. Figure 6.1 shows some representative SEMs of subsequent drying.

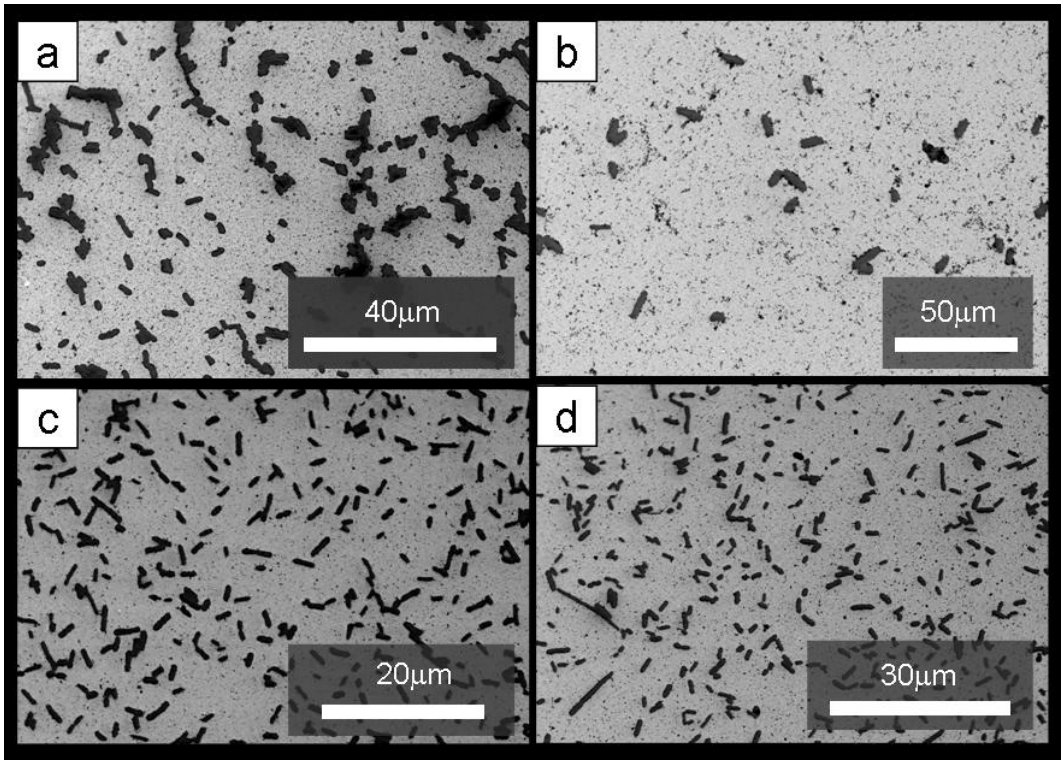

Figure 6.1: SEM images of bacterial capture with nitrogen drying and (a) no fixation, (b) ethanol dehydration, (c) glutaraldehyde fixation and (d) glutaraldehyde fixation and ethanol dehydration.

6.3.2 Cantilever Functionalization

Cantilevers were initially cleaned for 1hr at 70^{o}C in a Novascan UV cleaning system. After cleaning, cantilevers were emersed in ethanol for 20 minutes. Subsequently, the cantilevers were dried in nitrogen and their resonant properties were determined using the methods outlined in Chapter 4. Briefly, the first mode of resonance was determined experimentally. Then using the mode numbers determined by FEA in Chapter 4, the bending modes of resonance were isolated. This prediction method was repeated for each bending mode to better predict the next harmonic.

Microcantilevers were then functionalized with either the cysteine (not activated) or glutaraldehyde activated cysteamine as outlined in Chapter 5. Briefly, the cantilevers were incubated in either 25 mM (in MilliQ water) of cysteine (at 60^{o}C or room temperature) or cysteamine at room temperature overnight. Cantilevers were subsequently rinsed in MilliQ water. Cysteamine functionalized cantilevers were then activated by incubating them in 2% glutaraldehyde for 1 hour. The cantilevers were then immersed in T4 phage solution overnight at 40^{o}C. For a detailed description of the biological methods used, please see Chapter 5.

Surfaces were blocked with 1 mg/mL of BSA in PBS after phage adsorption. After brief rinsing, the cantilevers were then exposed to either host bacteria or bacteria free buffer for 20 to 30 minutes in a well mixed petri dish. Bacteria was either suspended in 5% TSB (cysteine cantilevers) or PBS buffer (cysteamine cantilevers). After brief rinsing in buffer and buffer-Tween20 solutions, cantilevers were then immersed in 2% v/v of glutaraldehyde for 1 hour. Several cantilevers were not fixed until they were inspected by fluorescent microscopy to assess bacterial capture before drying. After fixation with glutaraldehyde cantilevers were then immersed in several ethanol-water mixtures (24%, 48%, 71%, 95% percent ethanol in water by volume) of increasing ethanol concentration. Cantilevers were then dried in nitrogen and their final resonance properties were determined.

6.4 Cysteine on Functionalized Gold Cantilevers

TL-Arrow-2Au cantilevers were used in bacterial detection on cysteine functionalized cantilevers. Successful bacterial capture using cysteine mediated phage adsorption caused average downward shifts of -10 kHz and -14 kHz for the 8^{th} and 9^{th} bending modes of resonance respectively. This corresponds to an average mass per unit area of 93 fg/μm^2 and 99 fg/μm^2 respectively. Assuming that a bacteria is a cylinder with a diameter of 1

μm and a length of 2 μm, this corresponds to approximately 4.7 and 4.9 bacteria/100 μm^2. This is in agreement with results from Chapter 5.

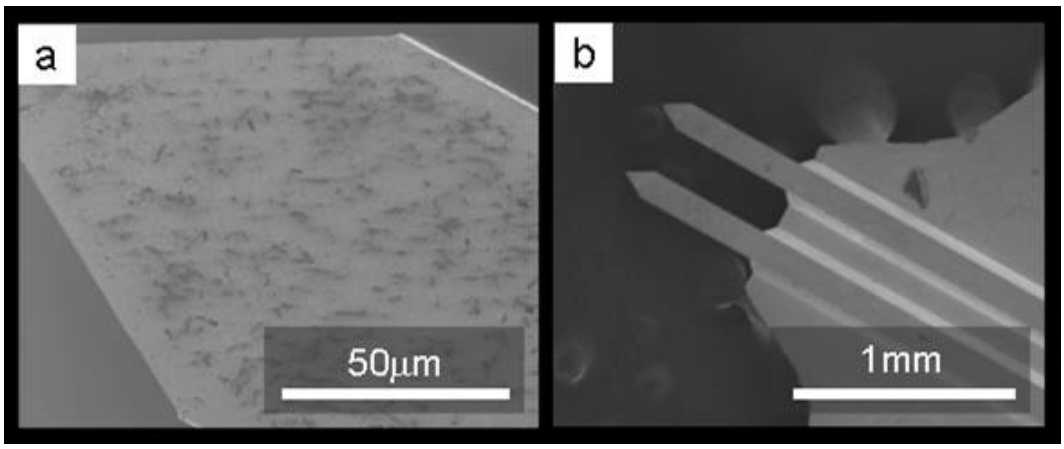

Figure 6.2: Bacterial adsorption on a cysteine assisted phage functionalized TL-Arrow-2Au cantilever array. (a) shows a zoom in of the time of the cantilever while (b) shows the cantilever chip.

However, cysteine cantilever experiments proved very unrepeatable in terms of successful functionalization of cantilevers. The cysteine consistently crystalized in solution, often on the cantilever causing unpredictable results. Both the adsorption temperature and concentration of cysteine was modified and still crystallization remained troublesome.

6.5 Experiment: Phage on Glutaraldehyde Activated Cysteamine Functionalized Gold

TL-CONT cantilevers were sputter coated with 20 nm of gold and then functionalized with cysteamine as described above. All of the bending modes or resonance were tracked. Cantilevers were either exposed to host bacteria or no bacteria before fixation. The first two modes of resonance shows statistically no difference between the host bacteria and the control. Higher modes showed consistent frequency shifts for host bacteria, while the control showed negligible frequency shifts. Following the linearization of the data an added mass of 1.859 ng was determined, which corresponds to about 3 bacteria/100μm^2. These results are summarized in Figure 6.3.

This is significantly less than the expected values predicted by Chapter 5. This is attributed to nonuniform bacteria adsorption on the cantilever itself. Furthermore, results

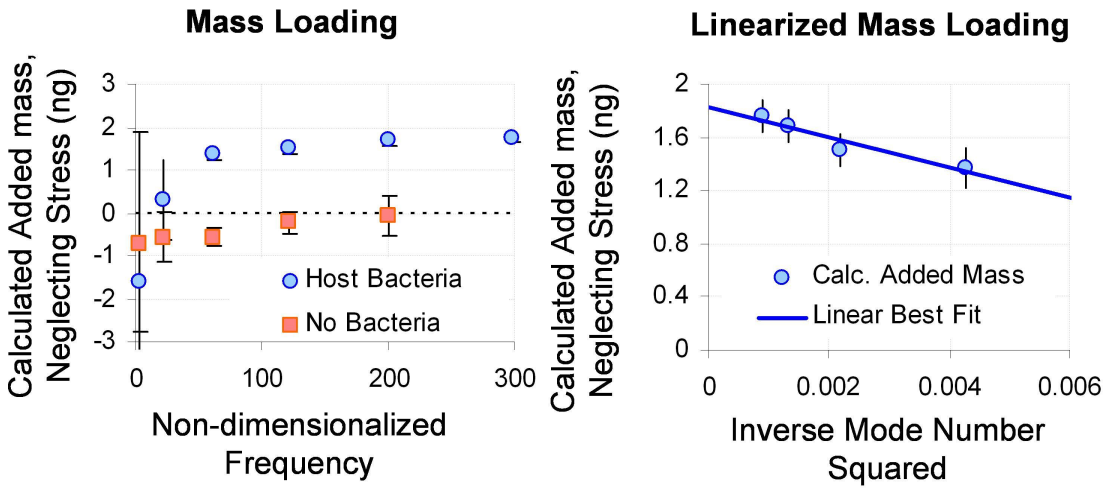

Figure 6.3: Left: Calculated added mass of cantilevers exposed to host bacteria and no bacteria. Right: Linearized calculated average mass with a linear best fit. Only frequency shifts that were statistically different than the control shifts were used in this fit.

were not repeatable, due to unexpected adsorption phenomena. The frequency shift was as expected when bacteria was observed on the cantilevers. However, more often than not the cantilever captured very few bacteria, while the base of the cantilever was covered uniformly. This was seen in both SEM and fluorescence microscopy, so the phenomena is not due to drying of the cantilever. These effects were noticeable on both TL-CONT cantilevers and TL-arrow cantilevers. SEM images of both types of cantilevers with this immobilization pattern can be seen in Figure 6.4.

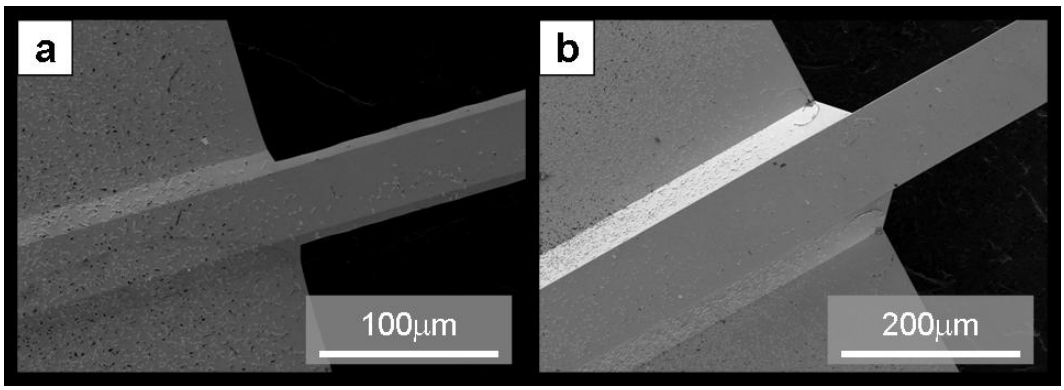

Figure 6.4: The base of TL-CONT (a) and TL-Arrow-Au-1 (b) cantilevers after functionalization and bacteria capture. While the chip did significantly capture bacteria, almost no bacteria was on the actual cantilever structure.

The most likely explanation for this property is the surface transport of bacteria to the

cantilever. Edge effects may cause unexpected bacterial adsorption and disturb the flow enough that bacteria are transported away. Unlike the base of the chip, the cantilever is not a rigid flat plate and is free to move in the solution. This could possibly generate flow patterns that would actively move bacteria away from the microcantilever. Slight differences in microcantilever placement during bacterial capture could affect the flow pattern of the mixing in experiments. This could explain why sometimes bacterial capture was successful to a degree.

6.6 Conclusions

Several proof-of-concept experiments have been demonstrated combining cantilever the theory developed in Chapter 4 and the phage immobilization procedures in Chapter 5. While some level experiments have been demonstrated for bacteria detection, further refinement involving the capture of bacteria on the cantilever is required. This will most likely take the form of enhancing the surface transport of bacteria to the surface of the cantilever. This can likely be achieved by moving away from the AFM as a detection system and creating a fluidic system fully integrated with the cantilever sensors. On chip flow patterns can subsequently be tuned using geometry and other MEMS based components.

7 Conclusions

7.1 Summary

This work has demonstrated the detection potential of both phages as probes for bacteria detection and high mode resonant microcantilevers as bacterial biosensors.

The frequency response of a cantilever structure was examined in great detail with respect to the mass and surface stress loading. While the effect of mass loading is well established in cantilever mechanics, the effect of a surface stress is less defined. Here the effect of surface stress is modeled as an axial force on the cantilever beam as presented by others. Surface stress dependance for arbitrary modes of resonance is derived in the context of a modified Euler-Bernoulli equation. It was determined that for a given mode, surface stress causes a constant frequency shift as opposed to mass loading, which causes a constant relative frequency shift. For combined mass and surface stress loading, as the mode of resonance approaches infinity so to does the natural frequency. As this occurs, any relative frequency shift approaches a state of pure mass loading.

This concept was validated with FEA using ANSYS. Four different cantilevers were modeled and non-dimensionalized for comparison purpose. Mesh independence was established for each model. Cantilevers were assessed for mass, surface stress and combined loading. Small values of stress loading agreed well with the predicted values. For combined loading, by linearizing and performing a least square regression a more accurate prediction of the added mass was made than simply by neglecting stress.

Resonating cantilevers at higher modes proved challenging experimentally. The frequency response of the microcantilevers were noted to have many peaks corresponding to many different modes of resonance and noise. Bending mode peaks were isolated using the mode numbers of the cantilever predicted by FEA. The closest frequency determined was used to predict the subsequent harmonic.

Neutravidin was detected using the 4th, 5th and 6th modes of resonance. Gold coated cantilevers were functionalized with biotin, which specifically binds with avidin based molecules. After biotin immobilization, cantilevers were resonated and exposed to a solution of Neutravidin. By linearizing the frequency response equations, a mass loading of 2.3 fg/μm^2 of Neutravidin was predicted. This mass was decoupled from a tensile surface stress.

Enhancing the attachment of phages on gold surfaces was also achieved. The binding of T4 phages to surfaces modified with simple sugars (dextrose and sucrose) and amino acids (cysteine and histidine) was initially examined. These surfaces were then used to specifically capture bacteria at much higher densities than that of the physical adsorption of phages on gold. In addition, the temperature dependance of phage adsorption was assessed for a cysteine surface. A maximum bacterial adsorption was observed at 40^{o}C.

T4 phages were also covalently bound to surface. Cysteine and cysteamine monolayers on gold were activated with glutaraldehyde in order to capture free amine groups present on the phage. The maximum phage density was 18 ± 0.1 phages/μm^2, which corresponded to a bacterial capture of 11.9 ± 0.2 bacteria/100μm^2.

Lastly, proof of concept level bacteria detection was carried out on microcantilever sensors using cysteine and glutaraldehyde activated cysteamine phage capture techniques. Cysteine/phage functionalized cantilevers predicted about 5 bacteria/100μm^2. This agrees fairly well with previous chapters, but was unrepeatable due to cysteine crystallization on the cantilever. Glutaraldehyde activated cysteamine/phage funtionalized cantilevers performed worst then expected, predicting about 3 bacteria/100μm^2. Bacteria capture is believed to be reduced due to inefficient mass bacteria transport to the cantilever structure.

7.2 Future Directions

There are several different areas for development in this project so that a commercially viable technology is realized. First and foremost, cantilever sensors should be fabricated for better mass detection sensitivities. This will also increase the stress sensitivity, however these factors can be decoupled. Furthermore, this will allow for the microfluidic integration

of this sensing technology. As such, greater control over the fluid flow around the cantilever will be possible, which will likely increase the efficiency and repeatability of bacterial capture. Microfluidic integration will allow the cantilever sensor to be incorporated with micro-mixing and concentrating technologies. This will hopefully result in vastly improved surface capture of bacteria.

The AFM is suboptimal for most of the measurement being taken on it. A laser doppler vibrometer, such as those offered by Polytec, can be used to actually detect the mode shape of a vibrating cantilever. This will vastly increase the information gained about each mode for a given mechanical system and allow for an iterative design process. Furthermore, by pushing the frequency response to higher limits, higher mass sensitivities can be achieved.

In terms of improving the phage as an bio-detection probe, purification of the lysate is essential for optimal bacteria capture. This will allow minimal capture of contaminating proteins that will competitively bind with the phages. This could be coulped with optimization of the blocking layer to minimize the need to adsorb more protein on the surface. This would result in a more stable signal allowing for even smaller masses to be detected. Lastly, the theory developed in Chapter 4 is valid for cantilevers of all scales. As such, nanoscale cantilevers should be investigated at multiple modes for frequency response mass and stress decoupling.

Bibliography

[1] N. E. Redman, *Food Safety*. ABC CLIO, 2 ed., 2007.

[2] C. Poitras and N. Tufenkji, "A QCM-D based biosensor for *E. coli* O157:H7 highlighting the relevance of the dissipation slope as a transduction signal," *Biosensor and Bioelectronics*, vol. 24, pp. 2137–2142, 2009.

[3] C. M. Bourgeois and J. Y. Leveau, *Microbiological Control for Foods and Agricultural Products*. Wiley-VCH, 2 ed., 1995.

[4] J. Waswa, C. Debroy, and J. Irudayaraj, "Rapid detection of *Salmonella enteritidis* and *Escherichia coli* using surface plasmon resonance biosensor," *Journal of Food Process Engineering*, vol. 29, pp. 373–385, 2006.

[5] O. Lazcka, F. J. D. Campo, and F. X. Munoz, "Pathogen detection: A perspective of traditional methods and biosensors," 2007.

[6] P. Fratamico, "Comparison of culture, polymerase chain reaction (PCR), TaqMan *Salmonella*, and Transia Card *Salmonella* assays for detection of *Salmonella* spp. in naturally-contaminated ground chicken, ground turkey and ground beef," *Molecular and Cellular Probes*, vol. 18, pp. 215–221, 2003.

[7] T. on-site pathogen detection using antibody-based sensors, "Peter skottrup and mogens nicolaisen and annemarie justesen," *Biosensor and Bioelectronics*, vol. 24, pp. 339–348, 2008.

[8] F. Prez, M. Mascini, I. Tothill, and A. Turner, "Immunomagnetic separation with mediated flow injection analysis amperometric detection of viable *Escherichia coli* O157," *Anal. Chem.*, vol. 70, no. 11, pp. 2380–2386, 1998.

[9] H. Gu, K. Xu, C. Xu, and B. Xu, "Biofunctional magnetic nanoparticles for protein separation and pathogen detection," *Chem. Commun*, pp. 941–949, 2006.

[10] T. Arakawa, Y. Shirasaki, T. Izumi, T. Aoki, H. Sugino, T. Funatsu, and S. Shoji, "High-speed particles and biomolecules sorting microsystem using thermosensitive hydrogel," *Meas. Sci. Technol.*, vol. 17, pp. 3141–3146, 2006.

[11] C. Ferguson, N. Booth, and E. Allan, "An ELISA for the detection of *Bacillius subtillis* L-form bacteria confirms their symbiosis in strawberry," *Letters to Applied Microbiology*, vol. 31, pp. 390–394, 2000.

[12] I. Kourkine, M. Ristic-Petrovic, E. Davis, C. Ruffolo, A. Kapsalis, and A. Barron, "Detection of *Escherichia coli* O157:H7 bacteria by a combination of immunofluorescent staining and capillary electrophoresis," *Electrophoresis*, vol. 24, pp. 655–661, 2003.

[13] DuPont, *Bax System Q7 Manual*, 2006.

[14] M. Heller, "DNA microarray technology: Devices, systems and applications," *Annual Review of Biomedical Engineering*, vol. 4, pp. 129–153, 2002.

[15] R. Stoughton, "Applications of DNA microarrays in biology," *Annual Review of Biochemistry*, vol. 74, pp. 53–82, 2005.

[16] E. J. Biosensors and Bioelectronics, "Definition of biosensors." Online.

[17] S. Rao, K. Anderson, and L. Bachas, "Oriented immobilization of proteins," *Mikrochimica Acta*, vol. 128, pp. 127–143, 1998.

[18] B. Aronsson, J. Lausmaa, and B. Kasemo, "Glow discharge plasma treatment for surface cleaning and modification of metallic biomaterials," *Journal of Biomedical Materials Research*, vol. 35, pp. 49–73, 1997.

[19] Y. Kanari, Y. Shoji, H. Ode, T. Miyake, T. Tanii, T. Hoshino, and I. Ohdomari, "Protein adsorption on self-assembled monolayers induced by surface water molecules," *Japanese Journal of Applied Physics*, vol. 46, no. 9B, pp. 6303–6308, 2007.

[20] P. Wagner, M. Hegner, P. Kernen, F. Zaugg, and G. Semenza, "Covalent immobilization of native biomolecules onto Au(111) via N-hydroxysuccinimide ester functionalized self-assembled monolayers for scanning probe microscopy," *Biophsical Journal*, vol. 70, pp. 2052–2066, 1996.

[21] W. Senaratne, L. Andruzzi, and C. Ober, "Self-assembled monolayers and polymer brushes in biotechnology: Current applications and future perspectives," *Biomacromolecules*, vol. 6, pp. 2427–2448, 2005.

[22] H. Gao, K. Buchapudi, A. Harms-Smyth, M. Schulte, X. Xu, and H. Ji, "Improved surface modification approach fo micromechanical biosensors," *Langmuir*, vol. 24, no. 2, pp. 345–349, 2008.

[23] H. Chen, Y. Kim, J. Lee, S. Yoon, D. Lim, H. Choi, and K. Koh, "Enhancement of BSA binding on Au surfaces by Calix[4]bisazacrown monolayer," *Sensors*, vol. 7, pp. 2263–2272, 2007.

[24] T. Huang, J. Sturgis, R. Gomez, T. Geng, R. Bashir, A. Bhunia, P. Robinson, and M. Ladisch, "Composite surface for blocking bacterial adsorption on protein biochips," *Biotechnology and Bioengineering*, vol. 81, no. 5, pp. 618–624, 2003.

[25] V. Wu, S.-H. Chen, and C.-S. Lin, "Real-time detection of *Escherichia coli* O157:H7 sequences using circulating-flow systems of quartz crystal microbalance," *Biosensors and Bioelectronics*, vol. 22, p. 2007, 2006.

[26] K. Reimhult, K. Petersson, and A. Krozer, "QCM-D analysis of the performance of blocking agents on gold and polystyrene surfaces," *Langmuir*, vol. 24, no. 15, pp. 8695–8700, 2008.

[27] N. Moll, E. Pascal, D. Dinh, J.-P. Pillot, B. Bennetau, D. Rebiere, D. Moynet, Y. Mas, D. Mossalayi, J. Pistre, and C. Dejous, "A Love wave immunosensor for whole *E. coli* bacteria detection using an innovative two-step immobilisation approach," *Biosensor and Bioelectronics*, vol. 22, pp. 2145–2150, 2007.

[28] F. Frederix, K. Bonroy, G. Reekmans, W. Laureyn, A. Campitelli, M. Abramov, W. Dehaen, and G. Maes, "Reduced nonspecific adsorption on covalently immobilized protein surfaces using poly(ethylene oxide) containing blocking agents,"

[29] Y. Nagasaki, H. Kobayashi, Y. Katsuyama, T. Jomura, and T. Sakura, "Enhanced immunoresponse of antibody/mixed-PEG co-immobilized surface construction of high-performance immunomagnetic ELISA system," *Journal of Colloid and Interface Science*, no. 309, pp. 524–530, 2007.

[30] M. Ward and D. Buttry, "In situ interfacial mass detection with piezoelectric transducers," *Science*, vol. 249, pp. 1000–1007, 1990.

[31] M. Ohring, *Materials Science of Thin Films: Deposition and Structure*. Academic Press, 2002.

[32] S. Wenzel and R. White, "Analytic comparison of the sensitivities of bulk-wave, surface-wave and flexual plate-wave ultrasonic gravimetric sensors," *Appl. Phys. Lett*, vol. 54, no. 20, pp. 1976–1978, 1989.

[33] Z. Shen, M. Huang, C. Xiao, Y. Zhang, X. Zeng, and P. Wang, "Non-labeled QCM biosensor for bacterial detection using carbohydrate and lectin recognitions," *Anal. Chem.*, vol. 79, no. 6, pp. 2312–2319, 2007.

[34] X.-L. Su and Y. Li, "A QCM immunosensor for salmonella detection with simultaneous measurements of resonant frequency and motional resistance," *Biosensors and Bioelectronics*, vol. 21, pp. 840–848, 2005.

[35] J. Gardner, V. Varadan, and O. Awadelkarim, *Microsensors, MEMS and Smart Devices*. John Wiley and Sons, 1 ed., 2001.

[36] O. Tamarin, S. Comeau, C. Dejous, D. Moynet, D. Rebiere, J. Bezian, and J. Pistre, "Real time device for biosensing: design of a bacteriophage model using Love acoustic waves," *Biosensors and Bioelectronics*, vol. 18, pp. 755–763, 2003.

[37] C. Zimmermann, P. Mazein, D. Rebiere, C. Dejous, F. Josse, and J. Pistre, "A theoretical study of Love wave sensors mass loading and viscoelastic sensitivity in gas and liquid environments," *Proceedings of the IEEE Ultrasonics Symposium*, 2004.

[38] J. Homola, "Present and future of surface plasmon resonance biosensors," *Anal. Bioanal. chem*, vol. 377, pp. 528–539, 2003.

[39] S. Philips and Q. Cheng, "Recent advances in surface plasmon resonance based techniques for bioanalysis," *Anal. Bioanal Chem.*, vol. 387, pp. 1831–1840, 2007.

[40] R. Rich and D. Myska, "Why you should be using more SPR biosensor technology," *Drug Discovery Today: Technologies*, vol. 1, no. 3, pp. 301–308, 2004.

[41] A. Taylor, J. Ladd, Q. Yu, S. Chen, J. Homola, and S. Jiang, "Quantitative and simultaneous detection of four foodborne bacterial pathogens with a multi-channel SPR sensor," *Biosensors and Bioelectronics*, vol. 22, pp. 752–758, 2006.

[42] E. Kutter and A. Sulakvelidze, *Bacteriophages: Biology and Applications*. CRC Press, 2005.

[43] S. Sidhu, *Phage Display in Biotechnology and Drug Discovery*. Taylor and Francis Group, 2005.

[44] L. Gervais, "T4 bacteriophage fuctionalized micro-cantilevers for highly specific bacteria detection," Master's thesis, The University of Alberta, 2007.

[45] S. Sidhu, *Phage Display in Biotechnology and Drug Discovery*. CRC Press, 2005.

[46] V. Petrenko, "Phage-derived bioselective nanovechicles for drug and gene delivery," *Proceedings of NSTI-Nanotech*, vol. 2, 2007.

[47] V. Petrenko, "Landscape phage as a molecular rcognition interface for detection devices," *Microelectronics Journal*, 2007.

[48] J. M. V. Emon, *Immunoassay and other bioanalytical techniques*. CRC Press, 2006.

[49] W. Falk and R. James, "The tail sheath of bacteriophage T4 as a microactuator," *Ferroelectrics*, vol. 342, pp. 57–64, 2005.

[50] F. Arisaka, "Assembly and infection process of bacteriophage T4," *CHAOS*, vol. 15, 2005.

[51] V. Mesyanzhinov, P. Leiman, V. Kostyuchenko, L. Kurochkina, K. Miroshnikov, N. Sykilinda, and M. Shneider, "Molecular architecture of bacteriophage T4," *Biochemistry (Moscow)*, vol. 69, no. 11, pp. 1190–1202, 2004.

[52] L. Tang, W. Marion, G. Cingolani, P. Prevelige, and J. Johnson, "Three-dimentional structure of the bacteriophage P22 tail machine," *The EMBO Journal*, vol. 24, pp. 2087–2095, 2005.

[53] S. Steinbacher, U. Baxa, S. Miller, A. Weintraub, R. Seckler, and R. Huber, "Crystal structure of phage P22 tailspike protein comlexed with *Salmonella* sp. O-antigen receptors," *Proc. Natl. Acad. Sci*, vol. 93, pp. 10584–10588, 1996.

[54] A. Samuel, T. Pitta, W. Ryu, P. Danese, E. Leung, and H. Berg, "Flagellar determinants of bacterial sensitivity to chi-phage," *Proc. Natl. Acad. Sci.*, vol. 96, pp. 9863–9866, 1999.

[55] M. Sarikaya, C. Tamerler, A. Jen, K. Schulten, and F. Baneyx, "Molecular biomimetics: nanotechnology through biology," *Nature Materials*, vol. 2, pp. 577–585, 2003.

[56] V. Petrenko and V. Vodyanoy, "Phage display for detection of biological threats," *Jounral of Microbiological Methods*, vol. 53, pp. 253–262, 2003.

[57] J. Housby and N. Mann, "Phage therapy," *Drug Discovery Today*, 2009.

[58] A. Sulakvelidze, Z. Alavidze, and G. Morris, "Bacteriophage therapy," *Antimicrobrial agents and Chemotherapy*, vol. 45, no. 3, pp. 649–659, 2001.

[59] R. Carlton, "Phage therapy: Past history and future prospects," *Archivum Immunologiae et Terapiae Experimentalis*, vol. 47, no. 267-274, 1999.

[60] H. Handa, S. Gurczynski, M. Jackson, G. Auner, J. Walker, and G. Mao, "Recognition of *Salmonella typhimurium* by immobilized phage P22 monolayers," *Surface Science*, vol. 602, pp. 1392–1400, 2008.

[61] W. Sun, L. Brovko, and M. Griffiths, "Use of bioluminescentsalmonella for assessing the efficiency of constructed phage-based biosorbent," *Journal of Industrial Microbiology and Biotechnology*, vol. 27, p. 126, 2001.

[62] P. Mosier-Boss, S. Lieberman, J. Andrews, F. Rohwer, L. Wegley, and M. Breitbart, "Use of fluorescently labeled phage in the detection and identification of bacterial species," *Applied Spectroscopy*, vol. 57, no. 9, p. 2003, 2003.

[63] J. Wan, H. Shu, S. Huang, B. Fiebor, I.-H. Chen, V. Petrenko, and B. Chin, "Phage-based magnetoelastic wireless biosensors for detecting *Bacillus Anthracis* spores," *IEEE Sensors Journal*, vol. 7, no. 3, pp. 470–477, 2007.

[64] J. Wan, M. Johnson, R. Guntupalli, V. Petrenko, and B. Chin, "Detection of *Bacillus anthracis* spores in liquid using phage-based magnetoelastic micro-resonators," *Sensors and Actuators B*, vol. 127, pp. 559–566, 2007.

[65] R. Lakshmanan, R. Guntupalli, J. Hu, V. Petrenko, J. Barbaree, and B. Chin, "Detection of *Salmonella typhimurium* in fat free milk using a phage immobilized magnetoelastic sensor," *Sensors and Actuators B*, vol. 126, pp. 544–550, 2007.

[66] V. Nanduri, I. Sorokulova, A. Samoylov, A. Simonian, V. Petrenko, and V. Vodyanoy, "Phage as a molecular recognition element in biosenors immobilized by physical adsorption," *Biosensors and Bioelectronics*, vol. 22, number = , pages = 986-992,, 2007.

[67] L.-M. yang, J. Diaz, T. McIntire, G. Weiss, and R. Penner, "Covalent virus layer for mass-based biosensing," *Anal. Chem.*, vol. 80, no. 4, pp. 933–943, 2008.

[68] L. mei Yang, P. Tam, B. Murray, T. McIntire, C. Overstreet, G. Weiss, and R. Penner, "Virus electrodes for universal biodetection," *Anal. Chem.*, vol. 78, no. 10, pp. 3265–3270, 2006.

[69] L. Gervais, M. Gel, B. Allain, M. Tolba, L. Brovko, M. Zourob, R. Mandeville, M. Griffitghs, and S. Evoy, "Immobilization of biotinylated bacteriophages on biosensor," *Sensors and Actuators B*, 2007.

[70] T. Huang, J. Sturgis, R. Gomez, T. Geng, R. Bashir, A. Bhunia, P. Robinson, and M. Ladisch, "Composite surface for blocking bacterial adsorption on protien biochips," *Biotechnology and BIoenegineering*, vol. 81, no. 5, pp. 619–624, 2003.

[71] A. Shabani, M. Zourob, B. Allain, C. Marquette, M. Lawrence, and R. Mandeville, "Bacteriophage-modified microarrays for the direct impedimetric detection of bacteria," *Anal. Chem.*, vol. 80, no. 24, pp. 9475–9482, 2008.

[72] G. Hornyak, J. Dutta, H. Tibbals, and A. Rao, *Introduction to Nanoscience*. Oxford University Press, 2001.

[73] M. D. Ventra, S. Evoy, and J. Heflin, *Introduction to Nanoscale Science and Technology*. Springer, 2002.

[74] G. Binnig, C. Cerber, E. Stoll, T. Albrecht, and C. Quate, "Atomic resolution with atomic force microscope," *Europhysics Letters*, vol. 3, no. 12, pp. 1281–1286, 1987.

[75] P. Waggoner and H. Craighead, "Micro- and nanomechanical sensors for environmental, chemical and biological detection," *Lab Chip*, vol. 7, pp. 1238–1255, 2007.

[76] C. Ziegler, "Cantilever-based biosensors," *Anal. Bioanal. Chem.*, vol. 379, pp. 946–959, 2004.

[77] K. Ekinci and M. Roukes, "nanoelectromechanical systems," *Review of Scientific Instruments*, vol. 76, p. f, 2005.

[78] S. Campbell, *The Science and Engineering of Microelectronic Fabrication*. Springer, 2002.

[79] K. WIlliams and R. Muller, "Etch rates for micromachinging processing," *Journal of Microelectromechanical systems*, vol. 5, no. 4, 1996.

[80] S. Tatic-Lucic, W.-Y. Zhang, and N. Navneet, "Etch-stop characteristics of heavily B/GD-doped silicon epilayer in KOH and TMAH," *Sensors and Actuators A*, vol. 123, pp. 640–645, 2005.

[81] A. Chand, M. Viani, T. Schaffer, and P. Hansma, "Microfabricated small metal cantilevers with silicon tip for atomic force microscopy," *Journal of Microelectromechanical Systmes*, vol. 9, no. 1, pp. 112–116, 2000.

[82] M. Godin, *Surface Stress, Kinetics and Structure of Alkanethiol Self-Assembled Monolayers*. PhD thesis, McGill University, 2004.

[83] *Cantisense Specification Sheet*.

[84] A. Johansson, O. Hansen, J. Hales, and A. Boisen, "Temperature effects in Au piezoresistors integrated in SU-8 cantilever chips," *Journal of Micromechancis and Microengineering*, vol. 16, pp. 2564–2569, 2006.

[85] J. Ransley, M. Watari, D. Sukumaran, R. McKendry, and A. Seshia, "SU-8 bio-chemical sensor microarrays," *Microelectronic Engineering*, vol. 83, pp. 1621–1625, 2006.

[86] M. Hopcroft, T. Kramer, G. Kim, K. Tatakshima, Y. Higo, D. Moore, and J. Brugger, "Micromechanical testing of SU-8 cantilevers," *Fatigue Fract Engng Mater Struct*, vol. 28, p. 735, 2005.

[87] N. Backmann, C. Zahnd, F. Huber, A. Bietsch, A. Pluckthun, H.-P. Lang, H.-J. Guntherodt, M. Hegner, and C. Gerber, "A label-free immunosensor array using single-chain antibody fragments," *PNAS*, vol. 102, no. 41, pp. 14587–14592, 2005.

[88] S. Rao, *Mechanical Vibrations*. Pearson/Prentice Hall, 2005.

[89] B. Ilic, H. Craighead, S. Krylov, W. Senaratne, C. Ober, and P. Neuzil, "Attogram detection using nanoelectromechanical oscillators," *Journal of Applied Physics*, vol. 95, no. 7, pp. 3694–3703, 2004.

[90] Y. Y. C. Callegari, X. Feng, K. Ekinci, and M. Roukes, "Zeptogram-scale nanomechanical mass sensing," *Nano Leters*, vol. 6, no. 4, pp. 583–586, 2006.

[91] L. Fischer, "Development of silicon carbonitride nanomechanical resonators for bilogoical detection," Master's thesis, The University of Alberta, 2007.

[92] M. Ghatkesar, V. Barwich, T. Braun, J.-P. Ramseyer, C. Gerber, M. Hegner, H. P. Lang, U. Drechsler, and M. Despont, "Higher modes of vibration increase mass sensitivity in nanomechanical microcantilevers," *Nanotechnology*, vol. 18, 2007.

[93] T. Thundat, P. Oden, and R. Warmack, "Microcantilever sensors," *Nanoscale and Microscale Thermophysical Engineering*, vol. 1, no. 3, pp. 185–199, 1997.

[94] J. Sader, "Frequency response of cantilever beams immersed in viscous fluids with applications to the atomic force microscope," *Journal of Applied Physics*, vol. 84, no. 1, pp. 64–76, 1998.

[95] C. Eysden and J. Sader, "Frequency response of cantilever beams immersed in viscous fluids with applications to the atomic force microscope," *Journal of Applied Physics*, vol. 101, 2007.

[96] D. Dareing, F. Tian, and T. Thundat, "Effective mass and flow patterns of fluids surrounding microcantilevers," *Ultramicroscopy*, vol. 106, pp. 789–794, 2006.

[97] S. Basak, A. Raman, and S. Garimella, "Hydrodynamic loading of microcantilevers vibrating in viscous fluids," *Journal of Applied Phyics*, vol. 99, 2006.

[98] M. Clark and M. Paul, "The stochastic dynamics of an array of atomic force microscpoes in a viscous fluid," *Non-Linear Mechanics*, vol. 42, pp. 690–696, 2007.

[99] P. Decuzzi, A. Granaldi, and G. Pascazio, "Dynamic reesponse of microcantilver-based sensors in a fluidic chamber," *Journal of Applied Physics*, vol. 101, 2007.

[100] G. Campbell and R. Mutharasan, "Detection of pathogen *Escherichia coli* O157:H7 using self-excited PZT-glass microcantilevers," *Biosensors and Bioelectronics*, vol. 21, pp. 462–473, 2005.

[101] X. Xia and X. Li, "Resonance-mode effect on microcantilever mass-sensing performance in air," *Review of Scientific Instruments*, vol. 79, 2008.

[102] S. Verbridge, H. Craighead, and J. Parpia, "A megahertz nanomechanical resonator with room temperature quality factor over a million,"

[103] J. Henry, Y. Wang, and M. Hines, "Controlling energy dissipation and stablity of micromechanical silicon resonators with self-assembled monolayers," *Applied Physics Letters*, vol. 84, no. 10, pp. 1765–1767, 2004.

[104] K. Ekinci, Y. Yang, and M. Roukes, "Ultimate limits to inertial mass sensing based upon nanoelectromechanical systems," *Journal of Applied Physics*, vol. 95, no. 5, pp. 2682–2689, 2004.

[105] M. Ghatkesar, T. Braun, V. Barwich, J.-P. Ramseyer, C. Gerber, M. Hegner, and H. P. Lang, "Resonating modes of vibrating microcantilevers in liquid," *Applied Physics Letters*, vol. 92, 2008.

[106] S. Verbridge, D. Shapiro, H. Craighead, and J. Parpia, "Macroscopic tuning of nanomechanics: Substrate bending for reversible control of frequeny and quality factor of nanostring resonators," *Nano Letters*, vol. 7, no. 6, pp. 1728–1735, 2007.

[107] G. Chen, T. Thundat, E. Wachter, and R. Warmack, "Adsorption-induced surface stress and its effects on resonance frequency of microcantilevers," *Journal of applied Physics*, vol. 77, no. 8, pp. 3618–3622, 1995.

[108] K. Hwang, K. Eom, J. H. Lee, D. W. Chun, B. H. Cha, D. Yoon, and T. Kim, "Dominant surface stress driven by biomolecular interactions in the dynamical response of a nanomechanical microcantilevers," *Applied Physics Letters*, vol. 89, 2006.

[109] S. Khadem and M. Rezaee, "Non-linear free vibration analysis of a string under bending moment effects using the perturbation method," *Journal of Sound and Vibration*, vol. 254, no. 4, pp. 677–691, 2002.

[110] A. McFarland, M. Poggi, M. Doyle, L. Bottomley, and J. Colton, "Influence of surface stress on the resonance behavior of microcantilevers," *Applied Physics Letters*, vol. 87, 2005.

[111] P. Lu, H. Lee, C. Lu, and S. O'Shea, "Surface stress effects on the resonance properties of cantilever sensors," *Physical Review B*, vol. 72, 2005.

[112] S.-H. Tsai and H.-C. Kan, "Mathematical analysis of a model for the rectangular cantilever beam," *Journal of Physics D: Applied Physics*, vol. 40, pp. 6129–6137, 2007.

[113] J. Park, J. Ryu, S. Choi, E. Seo, J. Cha, S. Ryu, J. Kim, B. Kim, and S. Lee, "Real-time measurement of the contractile forces of self-organized cardiomyocytes on hybrid biopolymer microcantilevers," *Anal. Chem.*, vol. 77, no. 20, pp. 6571–6580, 2005.

[114] M. Lachut and J. Sader, "Effect of surface stress on the stiffness of cantilever plates," *Physical Review Letters*, vol. 99, 2007.

[115] B. Dhayal, W. Henne, D. Doorneweerd, R. Reifenberger, and P. Low, "Detection of *Bacillus Subtilis* spores using peptide-functionalized cantilever arrays," *J. Am. Chem. Soc.*, vol. 128, pp. 3716–3721, 2006.

[116] B. weeks, J. Camarero, A. Noy, A. Miller, L. Stanker, and J. Yoreo, "A microcantilever-based pathogen detector," *Scanning*, vol. 25, pp. 297–299, 2003.

[117] B. Ilic, D. Czaplewski, M. Zalalutdinov, and H. Craighead, "Single cell detection with micromechanical oscillators," *J. Vac. Sci. Technol. B*, vol. 19, no. 6, pp. 2825–2828, 2001.

[118] B. Ilic, D. Czaplewski, H. Craighead, P. Neuzil, C. Campagnolo, and C. Batt, "Mechanical resonant immunospecific biological detector," *Applied Physics Letters*, vol. 77, no. 3, pp. 450–452, 2000.

[119] A. Gupta, D. Akin, and R. Bashir, "Detection bacterial cells and antibodies using surface micromachined thin silicon cantilever resonators," *J. Vac. Sci. Technol. B*, vol. 22, no. 6, pp. 2785–2791, 2004.

[120] G. Campbell and R. Mutharasan, "Piezoelectric-excited millimeter-sized cantilever (PEMC) sensors detect *Bacillus anthracis* at 300 spores/mL," *Biosensors and Bioelectronics*, vol. 21, pp. 1684–1692, 2006.

[121] G. Campbell, J. Uknalis, S. Tu, and R. Mutharasan, "Detect of *Escherichia coli* O157:H7 in ground beef samples using piezoelectric excited millimeter-sized cantilever (PEMC) sensors," *Biosensors and Bioelectronics*, vol. 22, pp. 1296–1302, 2007.

[122] G. Campbell, D. deLesdernier, and R. Mutharasan, "Detection of airborne *Bacillus anthracis* spores by and integrated system of an air sampler and a cantilever immunosensor," *Sensors and Actuators B*, vol. 127, pp. 376–382, 2007.

[123] D. Ramos, J. Tamayo, J. Mertens, and Calleja, "Origin of the response of nanomechanical resonators to bacteria adsorption," *Journal of Applied Physics*, vol. 100, 2006.

[124] D. Ramos, J. Tamayo, J. Mertens, M. Calleja, L. Villanueva, and A. Zaballos, "Detection of bacteria based on the thermomechanical noise of a nanomechanical resonator: origin of response and detection limits," *Nanotechnology*, vol. 19, 2007.

[125] F. Lochon, I. Dufour, and D. Rebiere, "An alternative solution to improve sensitivity of resonant microcantilever chemical sensors: comparison between using high-order modes and reducing dimensions," *Sensors and Actuators B*, vol. 108, pp. 979–985, 2005.

[126] Nanoworld, *Arrow TL1 Data Sheet*.

[127] Nano Sensors, *TL-cont Data Sheet*.

[128] Nano Sensors, *TL-fm Data Sheet*.

[129] Nano Sensors, *TL-NCH Data Sheet*.

[130] F. Beltran, T. Scholz, G. Schneider, J. Munoz-Saldana, U. Rabe, and W. Arnold, "Finite-element simulation of cantilever vibrations in atomic force acoustic microscopy," *Journal of Physics: Conference Series*, vol. 61, pp. 293–297, 2007.

[131] ANSYS 11.0, *Solid45 Element Properties*.

[132] ANSYS 11.0, *Surf157 Element Properties*.

[133] ANSYS 11.0, *Solid45 Element Properties*.

[134] Invitrogen, "SYTO green-fluorescent nucleic acid stains data sheet," *Molecular Probes: Invitrogen Detection Technologies*, 2008.

[135] J. Vig, "UV/ozone cleaning of surface," *J. Vac. Sci. Technol A*, vol. 3, no. 3, pp. 1028–1034, 1985.

[136] H. Ron, S. Matlis, and I. Rubinstein, "Self-assembled monolayers on oxidized metals. 2. gold surface oxidative pretreatment, monolayer properties, and depression formation," *Langmuir*, vol. 14, pp. 1116–1121, 1998.

[137] H. Joshi, P. Shirude, V. Bansal, K. Ganesh, and M. Sastry, "Isothermal titration valorimetry studies on the binding of amino acids to gold nanoparticles," *J. Phys. Chem. B*, vol. 108, no. 31, pp. 11535–11540, 2004.

[138] D. Walt and V. Agayn, "The chemistry of enzyme and protein immobilization with glutaraldehyde," *Trends in analytical chemistry*, vol. 13, no. 10, pp. 425–430, 1994.

[139] J. Bozzola and L. Russel, *Electron Microscopy: Principles and Techniques for Biologist*. Jones and Bartlett Publishers, 1999.